CFD simulation of wet-towing operation of semi-submersible platforms

Floating Offshore Wind Turbines

Master's thesis
Ken Chen

Delft University of Technology

TUDelft   Boskalis   NTNU

CFD simulation of wet-towing operation of semi-submersible platforms

Floating Offshore Wind Turbines

by

Ken Chen

to obtain the degree of Master of Science

at the Delft University of Technology,

to be defended publicly on 8 August, 2025

TUDelft   **Boskalis**   NTNU

Summary

Floating wind is a proven concept to harvest wind energy in deeper water. Most technology of floating wind is transferred from the oil and gas industry. However, a commercial wind farm can consist of 50 wind turbines, and an efficient transport method is needed. Wet-towing is an efficient transport method, but it introduces fluid-structure interaction and should be carefully investigated. For wet-towing operations, the expected drag load is of interest, so a vessel with the right capacity can be chosen. Vortex shedding can occur since most semi-submersible platforms consist of several cylinders. This can cause vortex-induced motion and cause undesired motions such as sway motion.

While previous studies have examined fluid-structure interaction of semi-submersible platforms, two key gaps remain. First, most are conducted at model scale, where the lower Reynolds number leads to different flow regimes and may not reflect full-scale behavior. Second, many vortex-induced motion studies use single-phase simulations with a double-body assumption, neglecting the free surface and its influence on wake dynamics. These gaps highlight the need for full-scale, multiphase simulations to capture realistic wet-towing hydrodynamics.

This study carries out full-scale multiphase simulations to investigate three key aspects. It examines the influence of towing configuration, specifically heading and draft, on the hydrodynamic performance of the platform. It evaluates the impact of the free surface on vortex-induced motion of semi-submersible platforms. Finally, it compares the accuracy and efficiency of drag prediction and vortex behavior across three modeling approaches: full-scale multiphase, full-scale single-phase, and model-scale multiphase simulations.

The results indicate that $180°$ heading is preferable to $0°$, as it produces a more stable wake, lower drag, and avoids the constant offset lift forces observed in the $0°$ case. A shallower draft of 10 m is also favored, as both the free end and free surface effects help suppress coherent vortex shedding, reducing the risk of vortex-induced motion and lowering drag. Comparing models, full-scale single-phase simulations exhibit vortex shedding, while multiphase simulations develop a steady wake. This discrepancy arises from the unrealistic symmetry constraint at the free surface in single-phase cases. Finally, while model-scale simulations scaled by Froude's method can offer a conservative estimate for drag, they lack the fidelity needed to capture accurate vortex behavior.

These findings highlight the importance of using appropriate CFD models when evaluating towing strategies, and provide a foundation for optimizing semi-submersible transport operations in future floating wind projects.

Contents

List of Figures

List of Tables

Nomenclature

Abbreviations

Abbreviation	Definition
CFD	Computational Fluid Dynamics
VIM	Vortex-Induced Motion
VIV	Vortex-Induced Vibration
FFT	Fast Fourier Transform
Fr	Froude number
Re	Reynolds number
St	Strouhal number
Co	Courant number
RMS	Root mean square
Std	Standard deviation

Symbols

Symbol	Definition	Unit
U	Velocity	[m/s]
ρ	Density	[kg/m^3]
L	Characteristic length	[m]
V_r	Reduced velocity	[-]
ν	Kinematic viscosity	[m^2/s]
S	Wetted surface area	[m^2]
p	Pressure	[Pa]
$u_\star$	friction velocity	[-]
τ_w	wall shear stress	[Pa]

<div align="right">

1

</div>

<div align="right">

Introduction

</div>

1.1. Motivation

With the continuous development of renewable-energy technology, the cost of solar energy, wind energy, and other sources is gradually decreasing. The transition from traditional energy sources like fossil fuels to renewable energy sources is now a global trend. According to DNV [12], renewable energy sources are expected to provide 82% of the global power supply by 2050, with wind energy accounting for 33%. Additionally, 20% of this will come from onshore wind, 11% from bottom-fixed offshore wind, and 2% from floating offshore wind. The onshore wind and bottom-fixed offshore wind technologies are quite mature, while floating offshore wind technology is still in the early stages of development. Looking at the 2% of floating offshore wind, which is approximately 264 GW, the floating offshore wind market is expected to grow rapidly in the next few years. Assuming an average capacity of 15 MW per wind turbine, this would require around $17,600$ floating wind turbines.

80% of the world's offshore wind resources are located in waters over 60 m in depth [11]. To be able to make use of the wind resources in such areas, the technology of floating offshore wind is inevitable. Moreover, there are quite a few advantages of floating offshore wind turbines compared to bottom-fixed ones. The wind resources in deeper waters are generally better than in shallow waters close to shore. This is because of the higher wind velocity and less turbulence from the disturbance of the land. Also, floating wind turbines can be higher and bigger for better efficiency and performance [15].

There are some prototypes of floating wind turbines installed around the world, but the commercial development is still in its infancy. The initial designs and technologies of floating offshore wind were experience transferred from the long-existing oil and gas industry. However, the difference in transportation and installation costs comes into play when developing a commercial-scale offshore wind farm. As for the oil and gas industry, only a few drilling and production platforms need to be deployed for a field, whereas offshore wind farms can consist of 50 or even more wind turbines. Therefore, the scaling effect on the cost of transport and installation can be significant.

Figure 1.1 [17] shows the three common types of floating platforms for supporting wind turbines: the spar type, the semi-submersible type, and the TLP (tensioned-leg platform) type. The spar type requires a large water depth exceeding 100 m [7], and TLP is relatively more complicated to install than the other two types. Therefore, semi-submersible is a common type of floater used in water depths ranging from 60 m to 100 m. This can be seen as it has been used in many projects, such as WindFloat Atlantic, WindFloat Kincardine, Volturn US, and other projects under development [15]. Semi-submersible platforms are typically composed of cylinders, whose diameters can be uniform or varying.

Figure 1.1: Floating wind turbine platform types. From left to right: Spar, Semi-submersible, and TLP [17].
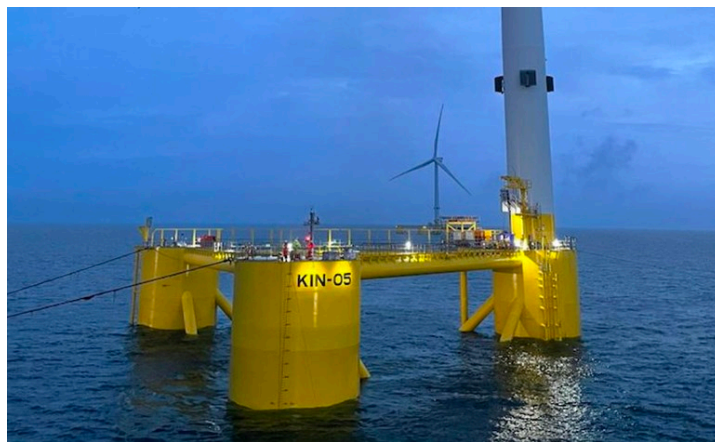
Figure 1.2: Semi-submersible platform of WindFloat Kincardine [22]

Transportation is a key factor in the cost and duration of the installation [14] due to the high day rates of the installation vessels. The two main transporting methods for semi-submersible platforms are by heavy marine transport vessels and wet-towing. The former requires costly heavy marine transport vessels, and the latter only requires tug boats. Since the semi-submersible platforms are self-floating, wet-towing can be more cost-efficient depending on the distance.

Wet-towing operation is a transporting method for floating structures by directly towing the structures across the water at sea level. However, this method requires careful planning to control the stability and

the loads from wind, wave, and current. The operability strongly depends on the weather. Nevertheless, it has proven to be a practical and cost-efficient method as it has been used in many projects. Figure 1.3 below is a picture of the wet-towing operation for the Kincardine project carried out by Boskalis.

Figure 1.3: Kincardine tow-out from Rotterdam to Scotland [2]

However, wet-towing also introduces hydrodynamic interaction between the platform and the water. It is known that vortex shedding occurs when fluid flows around a cylindrical structure, and the main components of semi-submersible platforms are circular cylinders. Vortices are created at the separation points on the cylinders and thus create a periodic variation in pressure distribution on the cylinder. The periodic pressure variation then leads to a periodic oscillation in the lift force and drag force. The oscillation forces can cause undesired motion responses in the wet-towing operation, especially if the force oscillation frequencies are close to the natural frequency of the towing system. Therefore, it should be studied, and that is the goal of this project.

Although there are some studies investigating vortex-induced motions (VIM) of floating platforms at their installed positions, very few have focused on the wet-towing phase. For performing wet-towing operations, the required drag force for towing the structure is important. This is to select the vessel with the right capacity. Furthermore, the design of towing system should also account for the potential vortex shedding as mentioned above. Since floating offshore wind is still in its early stages of commercial development, there is limited historical data or operational experience to rely on for understanding the vortex behavior during transportation. Boskalis already has experience in wet-towing operations with the Kincardine project. However, this experience remains limited and cannot fully inform all aspects of wet-towing hydrodynamics.

Further study is needed to optimize the towing configuration, in terms of heading and draft, understand what towing load to expect for different floaters, and what vessel to use. The chosen floater should be general so that the results can be extended to other similar floaters. For these reasons, the DeepCWind OC4 floater is chosen, as it is a general semi-submersible floater. The DeepCWind OC4 project is a test campaign held by NREL (National Renewable Energy Laboratory) together with many institutes and universities. Therefore, many studies have been carried out on this floater.

The scope of this study only includes the hydrodynamic interaction between uniform flow and the

semi-submersible floater. Other sources, such as wave, wind, current from an oblique angle, and propeller slipstream from the tug boat, are not included.

In Chapter 1, the findings from the literature review and the research plan are addressed. Subsequently, the fundamentals of CFD modeling are explained in Chapter 2. Based on that, the model setups for this study are demonstrated in Chapter 3. The model is then validated and verified in Chapter 4. The main findings and results are described in Chapter 5. Finally, the conclusions and the limitations of this study are wrapped up in Chapter 6 and 7.

1.2. State of research

The findings from the literature review are stated in this section. It includes relevant studies on this topic and some results from the literature for later validation in the research.

1.2.1. Vortex shedding and vortex-induced vibrations

Vortex shedding is a dynamic fluid phenomenon that occurs when fluid flows over a bluff body. At the boundary layer upstream of the separation point, vortices are generated, then convected downstream with the flow [23]. Figure 1.4 below shows the periodic pattern of vortex shedding. Vortex shedding and vortex-induced vibration of flow over circular cross-section structures are some widely studied topics due to their relevance in offshore engineering applications.
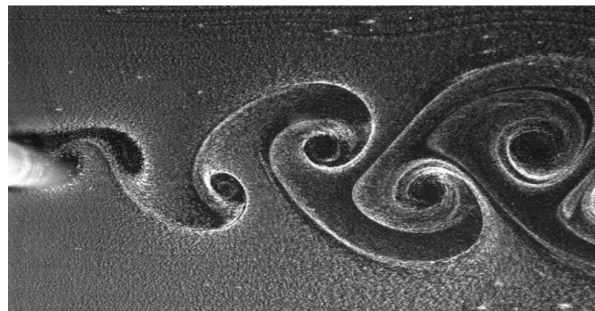
Figure 1.4: Vortex shedding period pattern [38]

Vortex shedding results in oscillatory forces both in the drag and lift directions on the object. The frequency of the forces should be investigated to prevent resonance with the system's natural frequencies. Figure 1.5 shows the periodic oscillation of lift and drag coefficients caused by vortex shedding. The lift coefficient oscillates with a mean around zero, and the frequency is the vortex-shedding frequency. On the other hand, the drag coefficient oscillates around a mean drag value, and the frequency is twice the vortex shedding frequency.
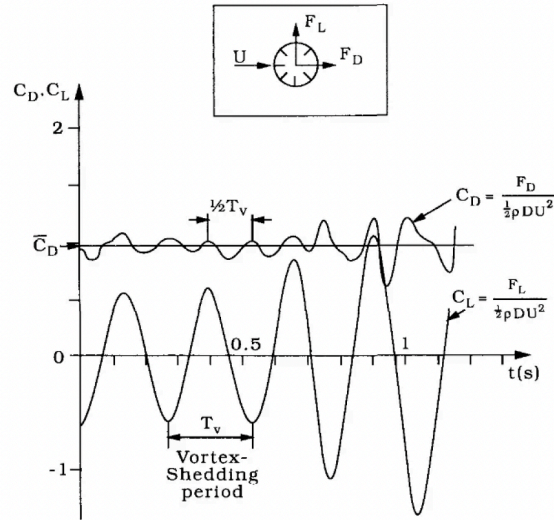
Figure 1.5: An example of drag and lift coefficient oscillations [20]

To quantify the vortex shedding frequency in a dimensionless way, the Strouhal number is introduced. The definition of Strouhal number is shown in Equation 1.1 [20].

$$\mathrm{St} = \frac{fL}{U_\infty} \tag{1.1}$$

The f is the shedding frequency, L is the characteristic length, and U_∞ is the free stream velocity. It describes the ratio of inertial forces due to the local acceleration of the flow to the inertial forces due to the convective acceleration. The Strouhal number is found to be a function of Reynolds number, which is defined in section 2.2, for flow over an infinite cylinder, and the relation is shown in Figure 1.6. It is found that the Strouhal number is roughly a constant of 0.2 at subcritical Reynolds numbers and increases with the Reynolds number in transcritical and supercritical regimes. The Strouhal number becomes a very large range depending on the surface roughness in high Reynolds number regimes.
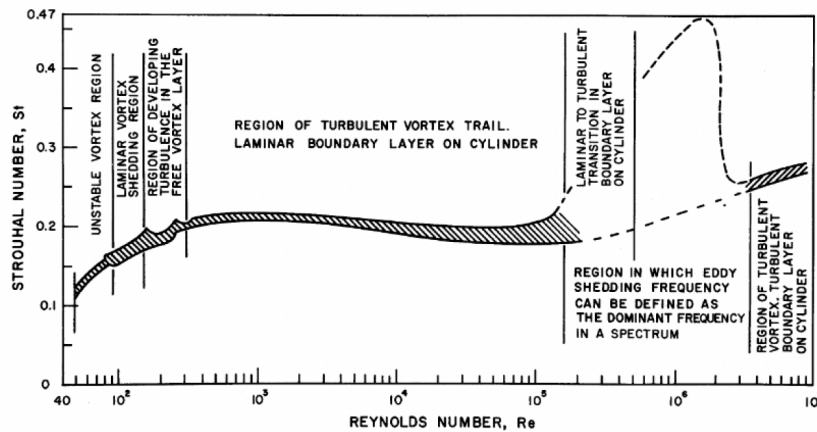
Figure 1.6: Relation between Strouhal number and Reynolds number for flow over infinite cylinders [19]

However, the aspect ratio L/D is typically not that high in wet-towing operations due to the shallow draft. Therefore, Benitz [4] suggested that it might be more appropriate to compare the Strouhal number to flow over spheres, for which the aspect ratio is 1. Kato [21] studied the vortex shedding of flow over spheres, and the relation between the Strouhal number and the Reynolds number is shown in Figure 1.7. As seen in the figure, multiple Strouhal numbers are found at the same Reynolds numbers. Therefore, the shedding frequencies of flow over spheres have a much wider range compared to flow over cylinders.
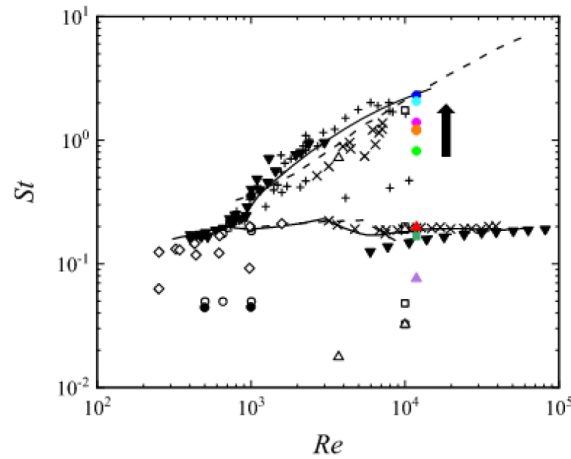
Figure 1.7: Relation between Strouhal number and Reynolds number for flow over spheres [21]

1.2.2. Flow interference of multiple cylinders

Semi-submersible platforms mainly consist of three or more circular cylinders; therefore, the interference between cylinders should also be investigated. Zdravkovich [39] presented Figure 1.8 to show that the interference can be defined as three different regions: proximity interference, wake interference, and no interference. This shows that if two cylinders are close together, the flow behavior and the forces acting on the structure might interfere with each other.
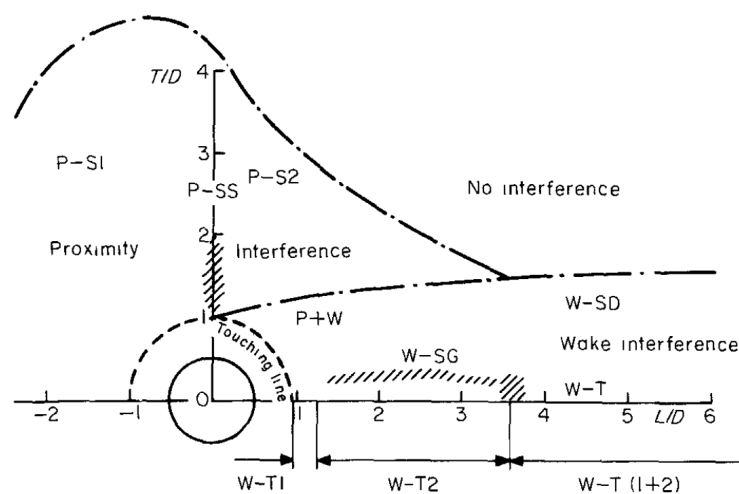
Figure 1.8: Flow interference regions for two-pipe arrangements [39]

For example, Igarashi [35] did model tests in a wind tunnel to find the effect of the spacings between tandem cylinders under relatively high Reynolds numbers. The result is shown in Figure 1.9a, the curve C_{D1} shows is the drag coefficient of the upstream cylinder, while C_{D2} is the downstream. The drag coefficient of the downstream cylinder is found to be lower than that of the upstream cylinder due to blockage. Additionally, as the distance increases from $L/d = 1$ to $L/d = 3.5$, the drag coefficient of the upstream cylinder decreases while that of the downstream cylinder increases. Exceeding $L/D = 3.5$, the interference between the two cylinders weakens, and the drag coefficients of both cylinders increase with a jump.
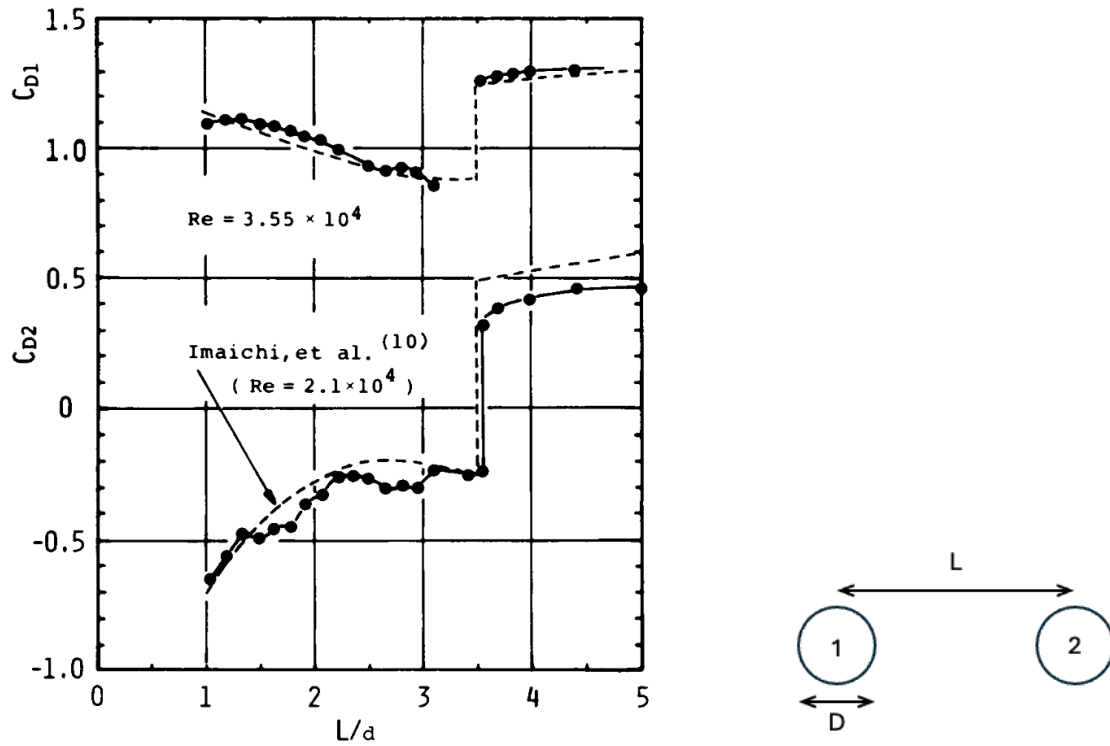
(a) Drag coefficients of upstream and downstream cylinders as a function of spacing ratio [35].

(b) Sketch of the upstream–downstream cylinder arrangement.

Figure 1.9: (a) Drag coefficient trends from Igarashi's study; (b) corresponding cylinder configuration.

1.2.3. Influence of vortex shedding on semi-submersible platforms

Looking into VIM of semi-submersible platforms, Jiang [18] and Liu [25] studied the vortex-induced motion of the INO WINDMOOR 12 MW semi-submersible platform, and the DeepCWind OC4 floater, respectively. The floaters are in their installed position, and the mooring line stiffness is simplified with an equivalent spring stiffness. The simulations are carried out in model scale, and single-phase with a double-body assumption.

In Jiang's [18] study, CFD simulations at model scale were carried out, and the results were verified with experimental results. Figure 1.10 a) shows the normalized VIM amplitude (A_y/D) over the reduced velocity ($U/(f_n D)$) of the INO WINDMOOR floater, and it is found to peak at a reduced velocity of 8. From Figure 1.10 b), it is also found that the sway motion period is closest to the natural period of sway at reduced velocity of 8. This shows that the main issue of VIM is when the frequency is close to the natural frequency and causes resonance.
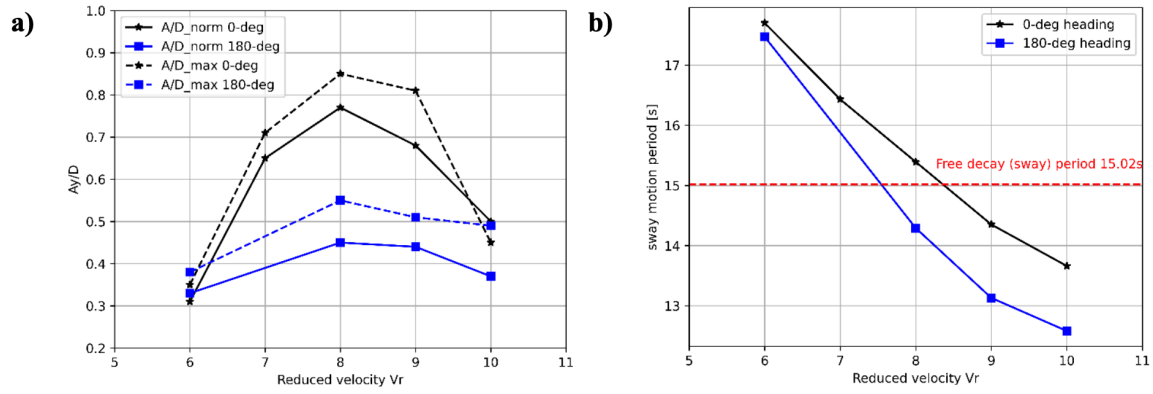
Figure 1.10: VIM amplitude and period of the INO WINDMOOR floater at different reduced velocities [18]

Jiang [18] also carried out a full-scale simulation at a reduced velocity of 8, where the sway motion is the largest. However, Table 1.1 shows that the normalized sway amplitude is much smaller in full-scale compared to the model-scale. This is likely due to the scaling effect from Froude scaling, where the velocity is scaled by the square root of the length ratio ($\sqrt{\lambda}$) and leads to a different Reynolds number. The Reynolds number in full-scale is 250 times larger than that of model-scale, which means that the flows are in completely different regimes.

Scale	Case	A_y/D_{max}	A_y/D_{norm}
Model Scale	V_r = 8	0.85	0.77
Full Scale	V_r = 8	0.14	0.11

Table 1.1: Comparison of model scale and full scale VIM amplitude of the INO WINDMOOR floater [18]

Liu [25] studied the VIM of the DeepCWind OC4 floater, which also has a similar geometry to the INO WINDMOOR floater. Model-scale numerical simulations are carried out in this study. The sway motion amplitude is shown in Figure 1.11. The maximum sway motion is also found at reduced velocity around 8. However, since both Jiang and Liu carried out their simulations at model scale, the Reynolds numbers are mismatched compared to full-scale in real life. Additionally, both studies focused on the floater while in its installed position, where the restoring force is from the mooring system.
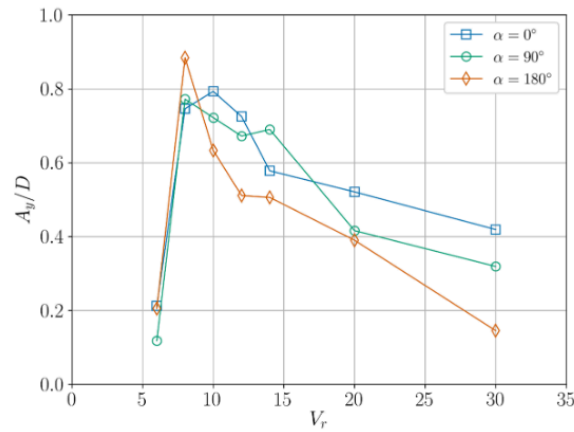
Figure 1.11: Normalized sway motion amplitude of the DeepCWIND OC4 floater over the reduced velocity in different headings [25]

Benitz [5] has also calculated the hydrodynamic loads of the DeepCWind OC4 floater using CFD tools. The simulations were also carried out on a model scale in their installed position. The geometry of the floater is simplified down to only the three side columns, i.e., the center column and the bracings are neglected. Figure 1.12 shows the inline and transverse forces when the flow speed is 0.085 m/s, which is 0.6 m/s in full-scale with Froude scaling, and with the configuration of one cylinder in front and two cylinders trailing symmetrically. The inline forces of the left and right columns are identical, and the transverse forces are 180 degrees out of phase. The transverse force oscillation period due to vortex shedding is around 7.5 seconds. Benitz mentioned that the transverse forces on the left and right columns are larger than the front column is likely due to flow diffraction and vortex shedding on the downstream columns, which means that the vortex shedding of the front column is likely suppressed due to the existence of the trailing columns.
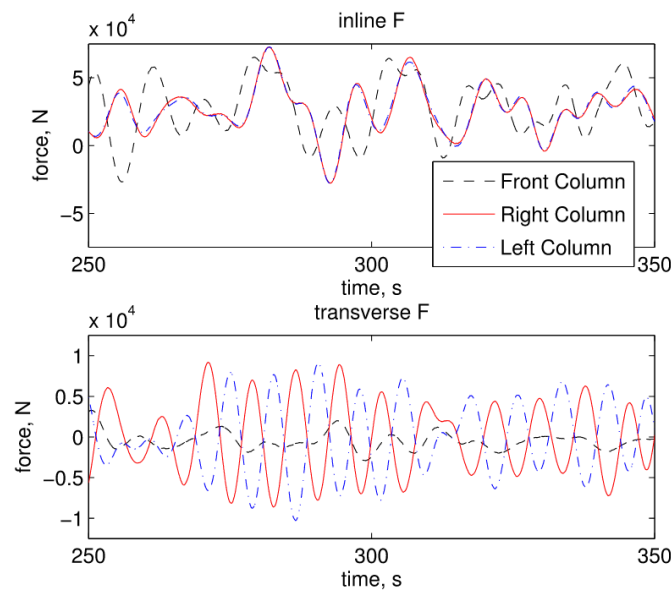
Figure 1.12: Inline and transverse forces on Front, Left, and Right column under 0.6 m/s flow speed predicted from OpenFOAM [5]

Benitz [3] also studied the effect of simplifying the geometry to only the side columns. Three simulations with different parts of the geometry were carried out:

- Large components: Only the three side columns
- Small components: The center column and the bracings
- Full geometry: Including both large components and small components

Figure 1.13 shows the inline and transverse forces of the large components, small components, and full geometry simulations. The large components and the small components have roughly the same drag force. However, the drag force on the full geometry is about 50% higher than the sum of the forces on the large components and the small components. This shows that superposition is not an accurate approach. This is likely because the flow is accelerated around the outer columns, and the accelerated flow leads to a higher drag force on the interior region of the flow. In contrast, the transverse force on the full geometry has a smaller amplitude compared to the large components, likely due to the added small components breaking the vortices. Overall, the drag force on the large components covers less than half of the full geometry. For an accurate prediction of the full geometry, the small components should not be neglected. However, for studying the transverse forces, it is more conservative to study the large components than to study the transverse force on the full geometry.
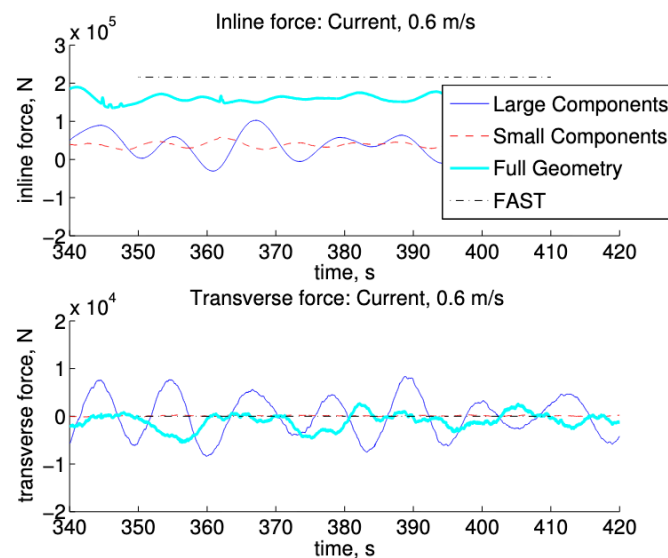
Figure 1.13: Inline and transverse force of large components, small components, and full geometry from CFD, and FAST with drag coefficient of 1 [3]

Ramachandran[31] conducted experimental tests on the towing operation with the $1:50$ model-scale DeepCWind OC4 floater from 1 knot to 6 knots, i.e., 0.514 m/s to 3.084 m/s. The draft of 10 m is found to provide sufficient stability and can be used for wet-towing operations to reduce the drag force. Two different towing configurations shown in Figure 1.14 below are tested.

(a) Towing configuration 1

(b) Towing configuration 2
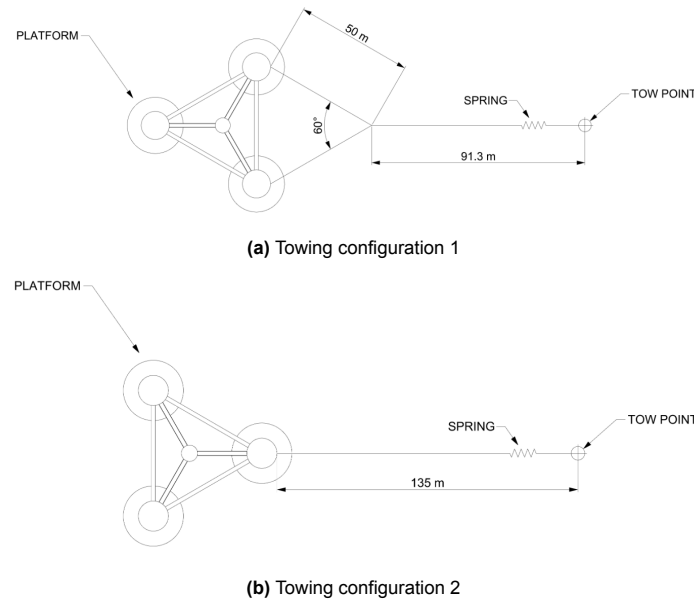
Figure 1.14: Two tested towing configurations [31]

The normalized sway motion amplitude at various speeds is shown in Figure 1.15. Configuration 1 has smaller sway motions at all speeds than configuration 2, likely due to the higher stability from the extra bridle connection. The maximum sway amplitude occurs at 1.5 m/s for configuration 1 and 1 m/s for configuration 2.
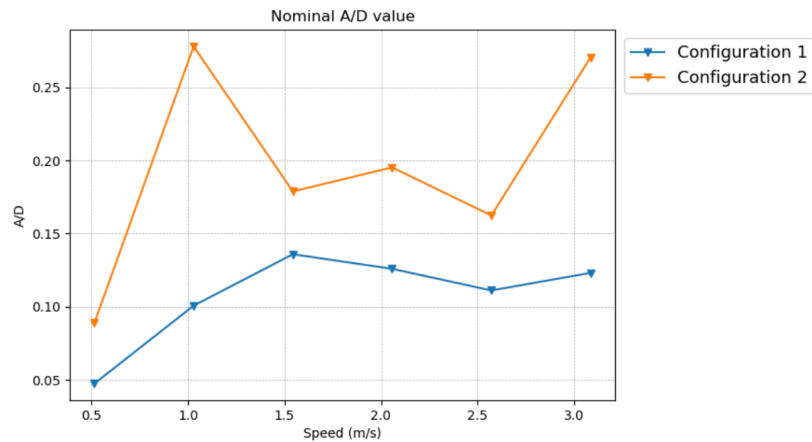
Figure 1.15: Normalized sway amplitude for both configurations[31]

The findings from the literature review can be concluded as follows:

- Numerous studies have investigated hydrodynamic behavior and vortex shedding characteristics of the DeepCWind OC4 semi-submersible floater in its installed position. However, the majority of numerical simulations have been conducted at model scale, which Reynols number is in the order of 10^4, with only a limited number performed at full scale, which Reynols number is in 10^7. This shows that the flow behavior can be completely different.

- For studying VIM on semi-submersible platforms numerically, only single-phase simulations are done, and no multiphase simulation is found. The maximum normalized sway amplitude (A_y/D) is found to be roughly 0.9 when the shedding period is close to the natural period of sway motion in its installed position.

- Even though the decreased-draft version of the floater has been examined experimentally to represent wet-towing conditions during transit operations, there are no numerical studies for this configuration. This gap limits the understanding of unsteady flow phenomena, such as vortex shedding and wake interactions, under wet-towing conditions.

The present study aims to address these gaps by performing full-scale CFD simulations of the DeepCWind OC4 floater in different towing configurations, with other parametric studies, such as draft effect, scaling effect, and free surface effect.

1.3. Research plan

The primary objective of this study is to **investigate the hydrodynamic behavior and the wake dynamics of a semi-submersible platform during wet-towing operations**. To be more specific, a few research questions and the methods are stated below.

1.3.1. Research Questions

What is the more preferable towing heading between 0° and 180° and draft depth in terms of drag and wake dynamics?

This goal is set to find a more preferable wet-towing configuration. From the model test Ramachandran has done, it is seen that the towing configuration with two columns leading is more preferable since the sway motion is generally smaller. However, the fluid and vortex behavior are not obtained. This gap is addressed by performing numerical simulations on both towing configurations. Furthermore, the wake dynamics of 10 m draft and 20 m draft are of interest. This is to select a more stable draft for the towing configuration.

What is the influence of the free surface on studying VIM of semi-submersible platforms?

Both Jiang [18] and Liu [25] investigated VIM in single phase with a double-body assumption boundary condition, neglecting the free surface. The influence and appropriateness of this assumption on vortex behavior are of interest.

What are the accuracy and efficiency of drag prediction and vortex behavior from full-scale multiphase model, full-scale single-phase model, and model-scale multiphase model?

Since most simulations are conducted at model scale, the differences in vortex behavior and drag prediction between model scale and full scale are of interest. Furthermore, model-scale simulations are much more efficient, so the level of representativeness of model-scale simulations is also of interest. Additionally, the drag forces obtained from CFD simulations are also compared to the drag force predicted with the drag coefficient from the explicit relation between drag coefficient and Reynolds number for flow over cylinders.

1.3.2. Research Methods

To address the research questions, multiple CFD models are developed and simulated under different configurations, scales, and boundary conditions using *OpenFOAM*. Each model corresponds to a

specific scenario designed to isolate the effects of towing direction, free surface presence, and model scaling.

- To investigate the influence of towing heading, simulations were conducted for both $0°$ and $180°$ configurations using a fixed semi-submersible model in multiphase flow. The drag forces and vortex shedding behavior are analyzed and compared. Furthermore, to select a preferable draft, a 10 m draft model is compared to a 20 m draft model.

- To assess the impact of the free surface, two models are constructed at full scale: one with a single-phase double-body assumption (symmetry at the free surface), and the other with a multiphase setup. Drag forces, lift fluctuations, and vortex structures are compared.

- To explore the effect of scaling and the trade-off between accuracy and computational efficiency, a model-scale model is conducted in multiphase flow. The drag force and vortex structures are compared with the full-scale multiphase model.

2

CFD modeling Fundamentals

2.1. Computational Fluid Dynamics

There are a few common ways to study the behavior and interaction of fluid flows between structures. The simplest way is by solving the analytical solution with potential flow theory. However, potential flow theory assumes the flow to be irrotational, which does not serve the purpose of studying vortices. Other two common methods are by conducting model tests in water tanks or ocean basins, or by simulating the flow using Computational Fluid Dynamics (CFD) tools. CFD simulations are often used in engineering fields such as aerodynamics and hydrodynamics to predict the lift and drag force, as well as other flow properties.

The most common numerical method employed by CFD tools is the finite volume method, which ensures that conservation principles are maintained within each discrete control volume (mesh cell).

2.1.1. Conservation principles

Conservation laws are the fundamentals of computational fluid dynamics. The motion of the fluid can be completely determined by the conservation laws of mass, momentum, and energy. A conservation law means that the variation of the property within a given volume is zero. There is flux crossing the boundary surface, entering and leaving the domain. However, the overall net balance is zero.

$$\frac{\partial}{\partial t} \int_{\Omega} \rho \, d\Omega + \oint_{S} \rho \vec{v} \cdot \, d\vec{S} = 0 \tag{2.1}$$

Equation 2.1 [13] is the conservation of mass equation, also known as the continuity equation, where Ω is the controlled volume and S is the boundary of the controlled volume. It states that the rate of change of mass within a controlled volume is equal to the net mass flow rate across the boundary of the volume.

$$\frac{\partial}{\partial t} \int_\Omega \rho \vec{v} \, \mathrm{d}\Omega + \oint_S \rho \vec{v} (\vec{v} \cdot \mathrm{d}\vec{S}) = \int_\Omega \rho \vec{f_\mathrm{e}} \, \mathrm{d}\Omega + \oint_S \bar{\bar{\sigma}} \cdot \mathrm{d}\vec{S} \tag{2.2}$$

Equation 2.2 [13] is the conservation of momentum equation, also the so-called Navier-Stokes equations. The $\vec{f_\mathrm{e}}$ is the external force and $\bar{\bar{\sigma}}$ is the internal stress tensor. It shows that the rate of change of momentum within a controlled volume must come from external forces. The internal force, which is the last term in Equation 2.2, mostly cancels out for points inside the volume. Therefore, only the points that lie on the boundary surface remain.

$$\frac{\partial}{\partial t} \int_\Omega \rho E \, \mathrm{d}\Omega + \oint_S \rho E \vec{v} \cdot \mathrm{d}\vec{S} = \oint_S k \vec{\nabla} T \cdot \mathrm{d}\vec{S} + \int_\Omega \left(\rho \vec{f_\mathrm{e}} \cdot \vec{v} + q_H \right) \mathrm{d}\Omega + \oint_S (\bar{\bar{\sigma}} \cdot \vec{v}) \cdot \mathrm{d}\vec{S} \tag{2.3}$$

Lastly, Equation 2.3 [13] is the conservation of energy equation. Breaking down each term in the equation, the two terms on the left-hand side of the equation are the rate of change of the energy within the volume and the energy flux across the boundary, respectively. The first term on the right-hand side of the equation is the heat flux, where k is the thermal conductivity and T is the absolute temperature. The second term is the source term, which is the sum of energy contributions from external forces and heat generation. Finally, the last term is the surface source, which is the work done by internal shear stress.

2.2. Dimensionless parameters

In this section, a few dimensionless parameters that are commonly used in fluid dynamics and will be used later in the following sections are introduced.

2.2.1. Reynolds number

The Reynolds number is a dominant dimensionless parameter that describes the flow behavior. It represents the ratio of inertial forces to viscous forces and can be calculated as shown in Equation 2.4.

$$\mathrm{Re} = \frac{UL}{\nu} \tag{2.4}$$

The U is the free stream velocity, L is the characteristic length, and ν is the kinematic viscosity of the fluid. Figure 2.1 shows the flow regimes for flow around a smooth cylinder in different Reynolds numbers.
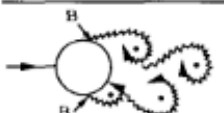
a)		No separation. Creeping flow	$Re < 5$
b)		A fixed pair of symmetric vortices	$5 < Re < 40$
c)		Laminar vortex street	$40 < Re < 200$
d)		Transition to turbulence in the wake	$200 < Re < 300$
e)		Wake completely turbulent. A:Laminar boundary layer separation	$300 < Re < 3 \times 10^5$ Subcritical **Typical model-scale Re**
f)		A:Laminar boundary layer separation B:Turbulent boundary layer separation;but boundary layer laminar	$3 \times 10^5 < Re < 3.5 \times 10^5$ Critical (Lower transition)
g)		B: Turbulent boundary layer separation;the boundary layer partly laminar partly turbulent	$3.5 \times 10^5 < Re < 1.5 \times 10^6$ Supercritical
h)		C: Boundary layer completely turbulent at one side	$1.5 \times 10^6 < Re < 4 \times 10^6$ Upper transition
i)		C: Boundary layer completely turbulent at two sides	$4 \times 10^6 < Re$ Transcritical **Typical full-scale Re**

Figure 2.1: Regimes of flow around a smooth cylinder [20]

For Reynolds numbers below 200, the flow is considered laminar. As the Reynolds number increases, the wake first turns turbulent, and eventually, the boundary layer also turns turbulent. As an example, model-scale simulations of wet-towing scaled down with Froude scaling roughly have a Reynolds number in the order of 10^4, while full-scale simulations fall in 10^7. From Figure 2.1, it is seen that the model-scale may still have laminar boundary layer separation, while it is completely turbulent at full scale.

The Reynolds number also affects the separation. Figure 2.2 [30] below shows the relation of the drag coefficient for a cylinder to the Reynolds number from multiple experiments. The drag coefficient decreases as the Reynolds number increases. This is because when the flow becomes more turbulent, the flow can follow the surface of the cylinder for longer, which delays the separation point. This makes the wake smaller and also reduces the drag force.
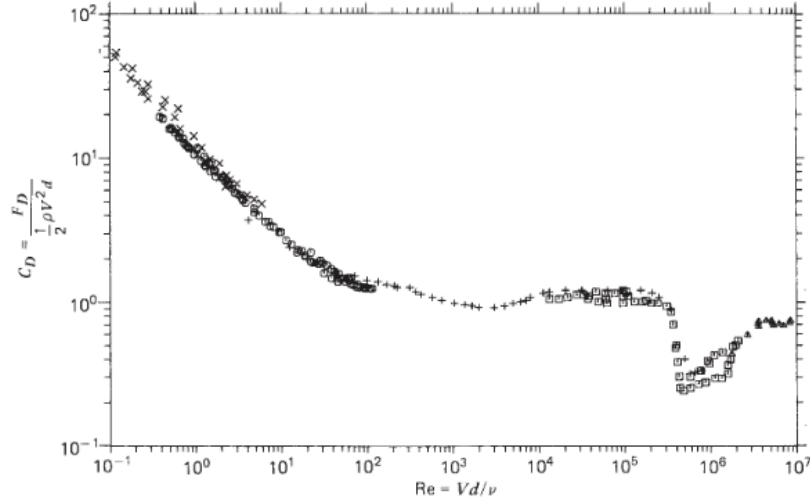
Figure 2.2: Drag coefficient for a cylinder [30]

2.2.2. Froude number

The Froude number is a dimensionless quantity that compares inertial forces to gravitational forces in free-surface flow, and it is defined as Equation 2.5.

$$\text{Fr} = \frac{U}{\sqrt{gL}} \tag{2.5}$$

The U is the characteristic velocity, g the gravitational acceleration, and L the characteristic length. It is often used to determine the similarity of the gravity waves in free-surface flows when scaling prototype models down to model scale. Froude scaling is the most common scaling approach in fluid mechanics. This ensures that the wave patterns are scaled correctly and reproduce the same wave-making effects as the full-scale scenario.

Froude scaling not only allows model-scale results to be representative of full-scale results, but it is also more efficient in time. Assume that the length scale ratio is λ, the velocity scale ratio would be $\sqrt{\lambda}$ following Equation 2.5. This means that the time scale is also $\sqrt{\lambda}$. Table 2.1 below shows an overview of how each physical quantity is scaled in Froude scaling, and also the ratio between the model-scale and full-scale model in this study. Details on Froude scaling forces are shown in section 2.7

			Model scale	Full scale
Length	m	λ^1	1	50
Speed	m/s	$\lambda^{0.5}$	1	$\sqrt{50}$
Time	s	$\lambda^{0.5}$	1	$\sqrt{50}$
Acceleration	m/s^2	λ^0	1	1
Area	m^2	λ^2	1	2500
Force	N	λ^3	1	125000
Moment	$N-m$	λ^4	1	6250000

Table 2.1: Froude scaling factors and the ratio between model scale and full scale in the present study

For the towing speeds considered in this study, the Froude numbers and the corresponding model-scale and full-scale velocities are shown in Table 2.2 below.

Towing speed [knot]	Fr	Model-scale velocity [m/s]	Full-scale velocity [m/s]
1	0.047	0.073	0.514
2	0.095	0.145	1.028
3	0.142	0.218	1.542

Table 2.2: Towing speeds considered in this study, and the corresponding Froude number, model-scale and full-scale velocity

2.2.3. Drag coefficient

Since semi-submersible floaters mostly consist of cylinders, the more common way to represent the resistance in a dimensionless way is with the drag coefficient (C_D). Differ from typical ship hull resistance, which is with a total resistance coefficient (C_T). The total resistance coefficient is non-dimensionalized with the wetted surface area (S), while the drag coefficient is non-dimensionalized with the projected frontal area (A) to the flow. Figure 2.3 below shows an example of how the projected frontal area is calculated for flow over a single side column of the DeepCWind OC4 floater.

$$\text{Drag} = \frac{1}{2}\rho A U^2 C_D \qquad (2.6)$$
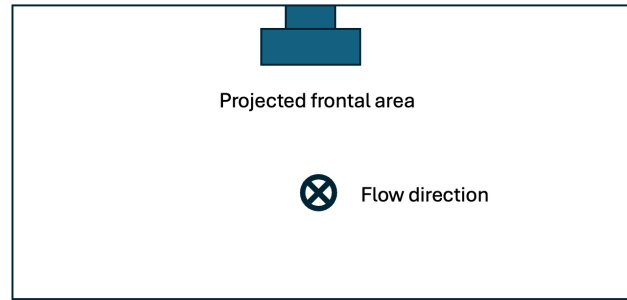
Figure 2.3: Sketch showing how the projected frontal area is defined to non-dimensionalize the drag force

2.2.4. y^+

The y^+ is the dimensionless wall distance that is used to determine the first cell height closest to the wall region. It is crucial because the quality and accuracy of the result depends on it. The y^+ is defined as Equation 2.7, where y is the distance from the wall to the centroid of the first cell, and u_* is the friction velocity [10].

$$y^+ = \frac{y u_*}{\nu} \qquad (2.7)$$

Figure 2.4 shows that y is measured from the boundary face to the center of the first cell. The velocity profile from the right also shows that a sufficiently small first cell height is required to properly capture the boundary velocity profile.
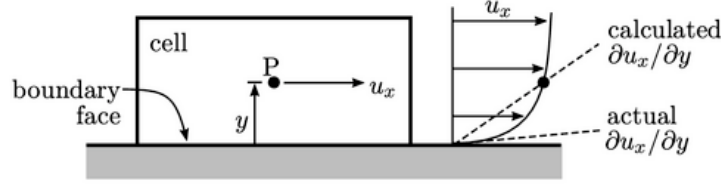
Figure 2.4: Sketch showing how y is measured [29]

The friction velocity is a derived dimensionless quantity to describe the shear stress between a fluid and a solid boundary. It is defined as Equation 2.8, where τ_w is the wall shear stress [34]. And the wall shear stress is the friction force per unit area that the fluid exerts on the wall, and can be calculated from the friction coefficient C_F as shown in Equation 2.9.

$$u_* = \sqrt{\frac{\tau_w}{\rho}} \tag{2.8}$$

$$\tau_w = \frac{1}{2} C_F \rho U^2 \tag{2.9}$$

Many different empirical equations exist for estimating the friction coefficient C_F. Here, the one from ITTC-1957 [32] is shown and used in the study. It is defined as a function of Reynolds number shown in Equation 2.10.

$$C_F = \frac{0.075}{(\log_{10} \mathrm{Re} - 2)^2} \tag{2.10}$$

The target y^+ value depends on whether wall functions are applied or not. If wall functions are used, the target y^+ value should be between 30 and 300. Details regarding wall function are explained in section 2.3. If wall functions are not used, the target y^+ value should be around 1 to 5 to be able to resolve the entire boundary profile.

2.2.5. Reduced velocity

The reduced velocity (V_r) is a dimensionless parameter that helps in understanding the interaction between the fluid flow and the oscillation of a structure and can be calculated as Equation 2.11. It is very similar to the reciprocal of the Strouhal number. The only difference is in the frequency. The U is the inflow velocity, f_n is the natural frequency of the structure instead of the shedding frequency, and D is the characteristic length. It is especially important for determining when the vortex shedding frequency is in synchronization with the natural frequency of the structure. In that case, the shedding frequency equals the natural frequency of the structure, and $V_r = 1/St$.

$$V_r = \frac{U}{f_n D} \tag{2.11}$$

2.2.6. Courant number

The Courant number, often denoted as Co, is a dimensionless parameter that arises from the stability condition of numerical schemes used to solve transient fluid flow problems. It is defined as

$$Co = \frac{U \Delta t}{\Delta x} \tag{2.12}$$

where U is the local flow velocity, Δt is the time step, and Δx is the characteristic cell size. The Courant number represents the ratio of physical distance travelled by the flow in one time step to the size of the computational cell. In explicit schemes, stability typically requires $Co < 1$, while implicit schemes such as PIMPLE in OpenFOAM [29] allow larger values, though accuracy and convergence may still cause issues if Co is too high. In this study, since implicit schemes are used, the maximum Co allowed for full-scale simulations is 5, and for model-scale simulations is 1.

2.3. Wall function

Figure 2.5 below shows the normalized velocity profile of a turbulent boundary layer. The n^+, also known as y^+, is the dimensionless wall distance, while u^+ represents the dimensionless velocity. The viscous sublayer of a boundary layer is very thin at high Reynolds numbers. Therefore, it is difficult to use a fine enough mesh to resolve it and capture the near-wall velocity profile. This problem can be avoided by using wall functions, which solve the boundary layer analytically instead of numerically.
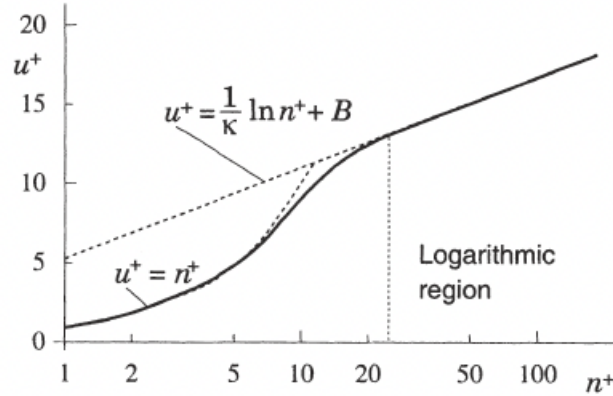
Figure 2.5: The velocity profile of turbulent boundary layer (n^+ is equivalent to y^+) [10]

As seen in Figure 2.5, the boundary layer profile can be divided into three regions, which is the viscous sublayer ($y^+ < 5$), the buffer layer ($5 < y^+ < 30$), and the inertial sublayer ($30 < y^+ < 200$) [8]. The two dotted lines in Figure 2.5 are empirical functions used to approach the viscous sublayer and the inertial sublayer, respectively.

Below are two common wall functions used in CFD simulations:

- Standard Wall Function: For standard wall functions, the velocity profile follows Equation 2.13 [29], where κ is constant 0.41 and B (typically 5.5 for boundary layer over smooth flat plate) is also constant related to the thickness of the viscous sublayer. y_{lam}^+ is where the two empirical functions

intersect, which is around 11.25. Neither line fits the profile in the buffer layer well, which is why the first cell height should be chosen to avoid the buffer layer when using standard wall functions.

$$u^+ = \begin{cases} y^+ & \text{if } y^+ \leq y^+_{lam} \\ \frac{1}{\kappa} \ln y^+ + B & \text{if } y^+ > y^+_{lam} \end{cases} \tag{2.13}$$

• Spalding's wall function: An alternative to the discontinuous standard wall function is Spalding's wall function, which is a continuous function that fits the profile in the buffer region better. The velocity profile follows Equation 2.14 [29], where E is the wall roughness parameter. This wall function allows the y^+ to be in the range from 1 to 300.

$$y^+ = u^+ + \frac{1}{E} \left[\exp(\kappa u^+) - 1 - \kappa u^+ - 0.5(\kappa u^+)^2 - \frac{1}{6}(\kappa u^+)^3 \right] \tag{2.14}$$

2.4. Turbulence modeling

Turbulent flows are characterized by complex, chaotic, and multi-scale structures such as eddies and vortices. Capturing the effects of turbulence accurately is essential in many engineering applications, including offshore hydrodynamics, where flow-body interaction and vortex-induced effects are critical. However, the full resolution of all turbulent scales is computationally expensive, especially at high Reynolds numbers. To handle this, various modeling approaches are used depending on the required fidelity and available computational resources. Figure 2.6 shows the pros and cons of each turbulence modeling method.
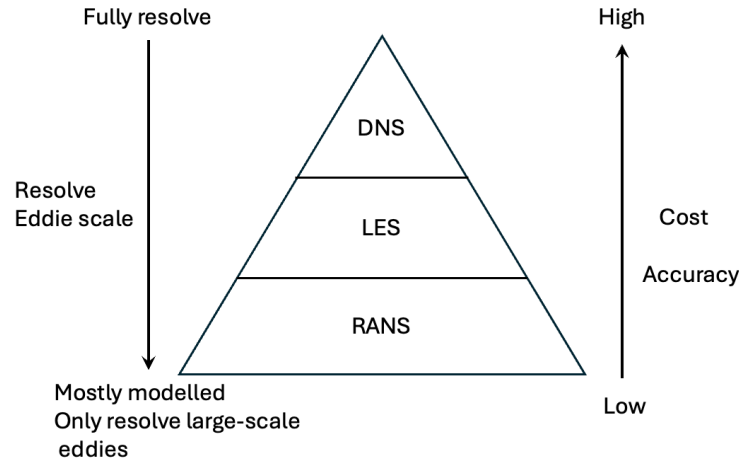
Figure 2.6: Pros and cons of each turbulence modeling method

2.4.1. Direct Numerical Simulation (DNS)

Direct numerical simulation resolves all scales of turbulence by directly solving the unsteady Navier-Stokes equations without any modeling. This approach provides the most accurate representation of turbulent flows, capturing eddies of all scales. However, the mesh resolution also needs to be incredibly fine to do so. Thus, DNS is extremely computationally demanding.

2.4.2. Large eddy simulations (LES)

In Large eddy simulations, a limiting scale size is set, any vortex smaller than that scale is filtered out and modeled, while the vortices larger than the limiting scale, which contain most of the energy,y are directly resolved. In Kolmogorov's 1941 theory [24], it is stated that turbulence at different scales is statistically similar. Additionally, the process of energy transfer when eddies break down is the same in the intermediate scale. This allows the large eddies to be explicitly resolved and implicitly accounts for the small eddies. If eddies at all scales are resolved, then it turns into a direct numerical simulation (DNS).

2.4.3. Reynolds-averaged Navier-Stokes (RANS)

In Reynolds-averaged Navier-Stokes modeling method, the turbulence fluctuation over time is ignored and calculating only the averaged turbulent flow. While in URANS (unsteady Reynolds-averaged Navier-Stokes), the averaging process is done in such way to obtain the mean turbulent quantities, at the same time retaining the time-dependent phenomena. RANS models can either model the turbulence of all scales or resolve the large eddies and only model for smaller-scale eddies.

In all, these three methods can be chosen based on the balance of computational cost and accuracy, and also the requirements of the phenomena being investigated. The RANS modeling method is chosen for this study for the efficiency, and the turbulence models for RANS modeling are shown in the next section.

2.5. Turbulence models

The Navier–Stokes equations are decomposed into mean and fluctuating components to model turbulence in LES and RANS. This leads to additional unknowns representing turbulent stresses. In RANS, these are modeled using turbulence models. Common two-equation models, such as k-ϵ and k–ω, solve transport equations for turbulence kinetic energy and its dissipation or specific rate.

2.5.1. Standard k-ϵ model

The two governing transport equations are characterized by the kinetic energy (k) and the dissipation per unit mass (ϵ). k is defined as the average kinetic energy per unit mass, and ϵ is defined as the rate at which turbulent kinetic energy (k) is dissipated per unit volume per unit time, as shown in Equation 2.16. These two equations are derived from the Reynolds stress equation shown in Equation 2.15, which calculates the stress due to turbulence.

$$-\rho \overline{u_i' u_j'} = \mu_t \left(\frac{\partial \overline{u}_i}{\partial x_j} + \frac{\partial \overline{u}_j}{\partial x_i} \right) - \frac{2}{3} \rho k \delta_{ij} \tag{2.15}$$

$$\epsilon = \nu \overline{\frac{\partial u_i'}{\partial x_k} \frac{\partial u_i'}{\partial x_k}}$$
$$k = \frac{1}{2} \overline{u_i' u_i'} \tag{2.16}$$

Equation 2.17 are the two governing equations for the k-ϵ model, where μ_t is the eddy viscosity, G_k and G_b are the generation of turbulence energy due to mean velocity gradients and buoyancy, respectively. Y_M represents the contribution of the fluctuating dilatation in compressible turbulence to the overall

dissipation rate. $C_{1\epsilon}$, $C_{2\epsilon}$, and $C_{3\epsilon}$ are constant coefficients, S_k and S_ϵ are some user-defined source terms.

$$\frac{\partial}{\partial t}(\rho k) + \frac{\partial}{\partial x_i}(\rho k u_i) = \frac{\partial}{\partial x_j}\left[\left(\mu + \frac{\mu_t}{\sigma_k}\right)\frac{\partial k}{\partial x_j}\right] + G_k + G_b - \rho\epsilon - Y_M + S_k$$

$$\frac{\partial}{\partial t}(\rho\epsilon) + \frac{\partial}{\partial x_i}(\rho\epsilon u_i) = \frac{\partial}{\partial x_j}\left[\left(\mu + \frac{\mu_t}{\sigma_\epsilon}\right)\frac{\partial\epsilon}{\partial x_j}\right] + C_{1\epsilon}\frac{\epsilon}{k}(G_k + C_{3\epsilon}G_b) - C_{2\epsilon}\rho\frac{\epsilon^2}{k} + S_\epsilon$$

(2.17)

The k-ϵ model is widely used due to its simplicity. However, it lacks accuracy for complex flows. One notable weakness is its relatively poor performance near walls compared to many other models. Despite these limitations, it remains popular in industrial applications where detailed near-wall effects are less critical.

2.5.2. Standard k-ω model

Kolmogorov [24] first proposed the k-ω model in 1941. It uses two parameters: the turbulence kinetic energy (k) and the specific dissipation rate (ω), where $\omega = \epsilon/k$. After decades of refinement, Wilcox [37] introduced the most recent version of the k-ω model in 2006, which is shown in Equation 2.18. In the below equation, G_k, Γ_k, and Y_k represent the generation of kinetic energy due to mean velocity gradients, effective diffusivity of k, and dissipation of k due to turbulence, respectively. And G_ω, Γ_ω, and Y_ω are analogous to the above, while S_k and S_ω are user-defined source terms.

$$\frac{\partial}{\partial t}(\rho k) + \frac{\partial}{\partial x_i}(\rho k u_i) = \frac{\partial}{\partial x_j}\left(\Gamma_k\frac{\partial k}{\partial x_j}\right) + G_k - Y_k + S_k$$

$$\frac{\partial}{\partial t}(\rho\omega) + \frac{\partial}{\partial x_i}(\rho\omega u_i) = \frac{\partial}{\partial x_j}\left(\Gamma_\omega\frac{\partial\omega}{\partial x_j}\right) + G_\omega - Y_\omega + S_\omega$$

(2.18)

The k-ω model performs well in the near-wall region, making it efficient for flows with complex boundary layers. It is also suitable for both low Reynolds number and high Reynolds number flows. On the other hand, the main downside of the standard k-ω model is its sensitivity to the turbulence in the free-stream region.

2.5.3. k-ω SST model

The k-ω SST model [26] combines the strengths of both the standard k-ω and k-ϵ models. It employs the k-ω model near walls, where it excels, and transitions to the k-ϵ model in the free-stream region, where the k-ω model is less reliable. Moreover, it can account for the transport of turbulent shear stress—a capability the standard model lacks. This allows a better prediction of the location of separation points, which is crucial for the accuracy of simulations.

The two governing equations of the k-ω SST model are shown in Equation 2.19, which can be found quite similar to the equations in Equation 2.18. However, the formation of G, Y, and S are slightly different since it includes a blending function to smoothly transition between two models. The additional D_ω term represents the cross-diffusion term. It is introduced because the SST model uses both k-ϵ and k-ω, and it is used to transform the k-ϵ model into equations based on k and ω.

$$\frac{\partial}{\partial t}(\rho k) + \frac{\partial}{\partial x_i}(\rho k u_i) = \frac{\partial}{\partial x_j}\left(\Gamma_k \frac{\partial k}{\partial x_j}\right) + \tilde{G}_k - Y_k + S_k$$

$$\frac{\partial}{\partial t}(\rho \omega) + \frac{\partial}{\partial x_i}(\rho \omega u_i) = \frac{\partial}{\partial x_j}\left(\Gamma_\omega \frac{\partial \omega}{\partial x_j}\right) + G_\omega - Y_\omega + D_\omega + S_\omega \tag{2.19}$$

This is also the model applied throughout the study. The reason is that the main focus of this study is on vortex behavior, and this requires a better prediction and higher accuracy on the separation and the boundary layer. Table 2.3 shows an overview and comparison of these three turbulence models. This indicates that the k-ω SST model better suits this purpose.

	Standard k-ϵ	Standard k-ω	k-ω SST
Near-wall accuracy	Poor	Excellent	Excellent
Free-stream sensitivity	Insensitive	Sensitive	Less sensitive
Turbulent shear stress	x	x	✓
Flow separation prediction	Poor	Less accurate	More accurate
Computational cost	Low	Moderate	Moderate to high

Table 2.3: Comparison of Turbulence Models

2.6. Boundary condition

In computational fluid dynamics (CFD), boundary conditions are essential to define how the flow variables behave at the edges of the computational domain. Proper specification of these conditions ensures physical realism and numerical stability.

For the simplified models in single-phase flow with a double-body assumption, the main variables are velocity U, pressure p, and turbulence quantities (e.g., k, ω).

To account for the effect of the free surface and to allow the free surface to move freely, the air phase needs to be included as well, which results in a multiphase model. For incompressible multiphase flow simulations, pressure in *OpenFOAM* is then p_{rgh} instead. This is to exclude the static pressure contributed by the gravitational force as shown in Equation 2.20. Additionally, volume fraction α is added to describe the fraction of the phases.

$$p_{rgh} = p - \rho g h \tag{2.20}$$

Boundary conditions in CFD are typically classified as `Dirichlet` or `Neumann` types. A `Dirichlet` boundary condition specifies the value of a variable directly at the boundary. In contrast, a `Neumann` boundary condition prescribes the gradient or derivative of a variable normal to the boundary, often set to zero to represent a natural outflow condition. Most practical CFD setups use a combination of both types, depending on the physical behavior expected at each boundary.

The boundary condition settings used in the study will be explained later in the report, depending on the case.

2.7. Resistance component

It is important to understand the resistance components as they are used to scale the resistance from model-scale measurements to full-scale structures in real life. Many different methods exist for separating the resistance components. The oldest and most widely used is Froude's method [27]. The total resistance coefficient (C_T) is divided into frictional resistance coefficient (C_F) and residual resistance (C_R) as shown in Equation 2.21. Residual resistance includes wave-making resistance and viscous pressure resistance (form drag). The frictional resistance is the frictional force due to the viscous friction between the hull and the fluid. The wave-making resistance comes from the energy lost while generating waves. Lastly, the viscous pressure resistance is the force caused by the pressure difference in the distribution, depending on the hull shape.

$$\text{Froude's method: } C_T = C_F + C_R \tag{2.21}$$

The frictional resistance coefficient is a function of the Reynolds number. The friction coefficient (C_F) is often estimated with the ITTC-1957 formula shown in Equation 2.10. Then, the frictional resistance can be estimated with Equation 2.22 below, where S is the wetted surface area.

$$R_F = \frac{1}{2}\rho U^2 S C_F \tag{2.22}$$

In Froude's method, the residual resistance is scaled by directly applying Froude scaling. The assumption is that the residual resistance coefficient in the model scale is identical to the full scale. The residual resistance is scaled with the cube of the length ratio as shown in Equation 2.24. However, it includes the form drag and the wave-making resistance as shown in Equation 2.25. As form drag does not follow Froude scaling, this method is conservative and tends to overestimate the total resistance.

$$C_{R,full} = C_{R,model} \tag{2.23}$$

$$R_{R,full} = R_{R,model}\lambda^3 \tag{2.24}$$

$$C_R = C_W + C_{form} \tag{2.25}$$

A more accurate approach is Hughes' method. Equation 2.26 shows the equation of Hughes' method. In this method, the form drag is separated from the wave-making resistance and included in the viscous component via a form factor (k).

$$\text{Hughes' method: } C_T = (1+k)C_F + C_W \tag{2.26}$$

Since the form factor (k) requires more simulations to obtain. Froude's method is used in this research despite that it tends to overestimate the resistance. This is because the form drag coefficient (k)

depends on the shape of the geometry and is typically larger than 0, and is not a function of Froude number. Froude's method is applied throughout the study to scale the drag force from model-scale to full-scale.

<div style="text-align: right; font-size: 3em;">3</div>

CFD modeling approach

3.1. DeepCWind OC4 floater

The OC4 semi-submersible floater is selected as the reference geometry for this study due to its extensive use in academic and research institutes related to floating offshore wind turbines. This floater is a widely accepted benchmark for validating hydrodynamic models and numerical solvers. Therefore, there are many studies done on this floater that allow easier validation. Moreover, the properties such as dimensions and mass properties are well-documented and publicly available, allowing easier comparison and reproducibility. Furthermore, the geometry is also very common for semi-submersibles, and can be representative of floaters with similar geometry. Figure 3.1 shows a $1/50$ model scale OC4 floater.

Figure 3.1: $1/50$ model scale OC4 floater [33]

The dimensions of the prototype OC4 floater are shown in Figure 3.2 with top and side views of the floater. The floater consists of three side columns, each with a larger base column and a smaller column stacked on top, a smaller center column in the center of the floater, and several bracings that support and connect the columns.
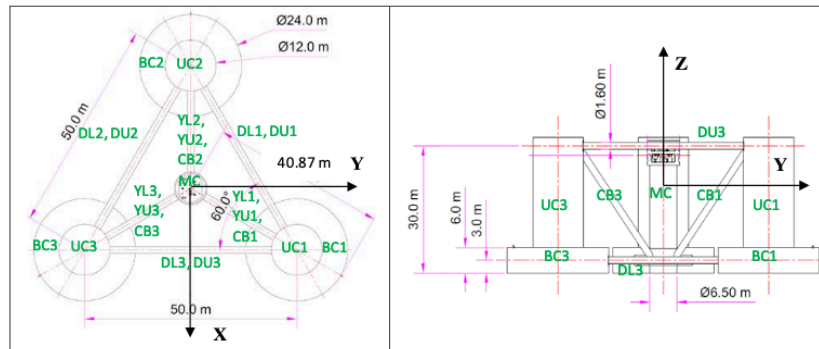
Figure 3.2: Dimensions of the OC4 floater [33]

The diameter and the length of the columns in both model scale and full scale are listed under Table 3.1. The designed installation draft of the OC4 floater is 20 m, which means the freeboard of the center column and side columns are 10 m and 12 m, respectively.

	Prototype	Model scale
Spacing between side columns	50 m	1 m
Diameter of center column	6.5 m	0.13 m
Diameter of side (upper) columns	12 m	0.24 m
Diameter of side (base) columns	24 m	0.48 m
Length of center column	30 m	0.6 m
Length of side (upper) columns	26 m	0.52 m
Length of side (base) columns	6 m	0.12 m

Table 3.1: OC4 floater dimensions

The model of the OC4 floater for this study is built using Rhino. For the sake of understanding the flow field and making it easier to identify vortex shedding, the bracings and the center column are not modeled. The model of the full-scale OC4 floater built in Rhino is shown in Figure 3.3. The designed waterline and the reduced draft version for wet-towing operations are marked on the figure as well. Note that this simplification is known to only capture about half of the drag force compared to the full geometry, seen in Benitz's study [3]. Therefore, the drag force cannot be compared to drag force of the full geometry.

(a) Top view of the floater geometry

(b) Side view of the floater geometry
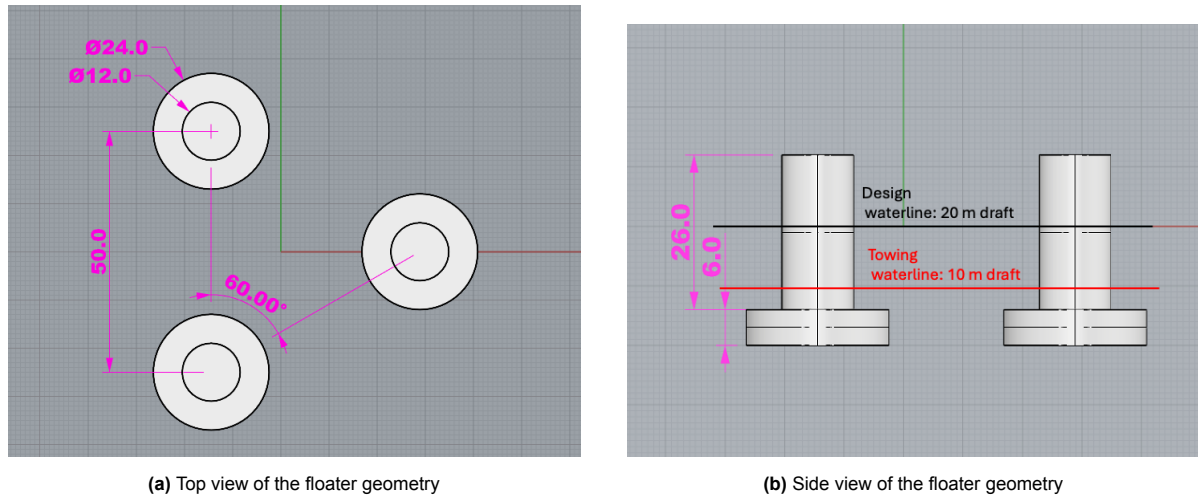
Figure 3.3: Geometry of the floater model in Rhino

3.2. Overview of the configurations and test cases for this study

Several simulations are conducted for the study, and an overview of the configurations is shown in Table 3.2, and they are labeled as C1 to C5. For studying the effect of towing heading, C1 and C2, which have $0°$ heading and $180°$ heading, are compared. Since vortex shedding is not observed in C1 and C2, a single-phase simulation (C4) is carried out to investigate the influence of the free surface. This is because, from the literature review, it is known that two studies focusing on VIM of semi-submersible floaters used single-phase setups, and the difference is of interest. Also, a multiphase simulation with the original designed draft of 20 m is simulated (C3) to see if an extra 10 m draft would lead to a different vortex behavior. Finally, the model-scale simulation (C5) is done for the comparison of drag prediction and efficiency.

	Scale	Phase	Towing heading	Draft
C1	Full-scale	Multiphase	$0°$	10 m
C2	Full-scale	Multiphase	$180°$	10 m
C3	Full-scale	Multiphase	$0°$	20 m
C4	Full-scale	Single-phase	$0°$	20 m
C5	Model-scale	Multiphase	$0°$	20 m

Table 3.2: Overview of the configurations for this study
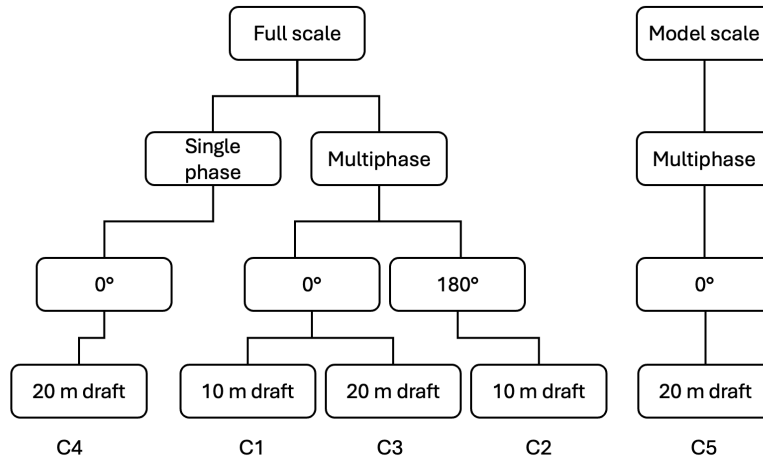
Figure 3.4: Flow chart showing the configuration of all the models simulated in this study

Table 3.3 shows the test cases done for each configuration. For C1 and C2, the focus is on drag prediction and vortex shedding frequency at different towing speeds. Therefore, towing speeds of 1, 2, and 3 knots are simulated. The highest towing speed is chosen to be 3 knots since wet-towing operations are normally limited to this speed from Boskalis' experience. While for the other configurations, the main focus is on the effect of simulation setups, so only the middle speed, i.e. 2 knots, is simulated.

	Towing speed [knot]	Fr	Re	Towing speed [m/s]
C1	1	0.047	6.17E+06	0.514
	2	0.095	1.23E+07	1.028
	3	0.142	1.85E+07	1.542
C2	1	0.047	6.17E+06	0.514
	2	0.095	1.23E+07	1.028
	3	0.142	1.85E+07	1.542
C3	2	0.095	1.23E+07	1.028
C4	2	0.095	1.23E+07	1.028
C5	2	0.095	3.48E+04	0.145 (Equivalent to 1.028 in full-scale)

Table 3.3: Test cases for each configuration in this study

3.2.1. Configuration for studying the effect of towing heading

The configurations of C1 and C2 for studying the effect of towing heading are demonstrated here to showcase the setup in more detail. These simulations are conducted to investigate the hydrodynamics involved in wet-towing operations, with a focus on drag forces and vortex shedding frequencies. The use of full-scale modeling is motivated by the findings of Jiang [18], who demonstrated that Reynolds number effects significantly influence vortex shedding behavior. The flow is much more turbulent in full scale compared to model scale, and the VIM amplitude in full scale is much smaller than model scale. Additionally, the simulations are multiphase to resolve the water–air interface, allowing the free surface

to deform naturally. This prevents artificial constraints that could otherwise distort the hydrodynamic forces, particularly drag. The two simulation setups are illustrated in Figure 3.5. These two setups serve the purpose of studying the effect of towing configuration.

(a) 0° configuration

(b) 180° configuration
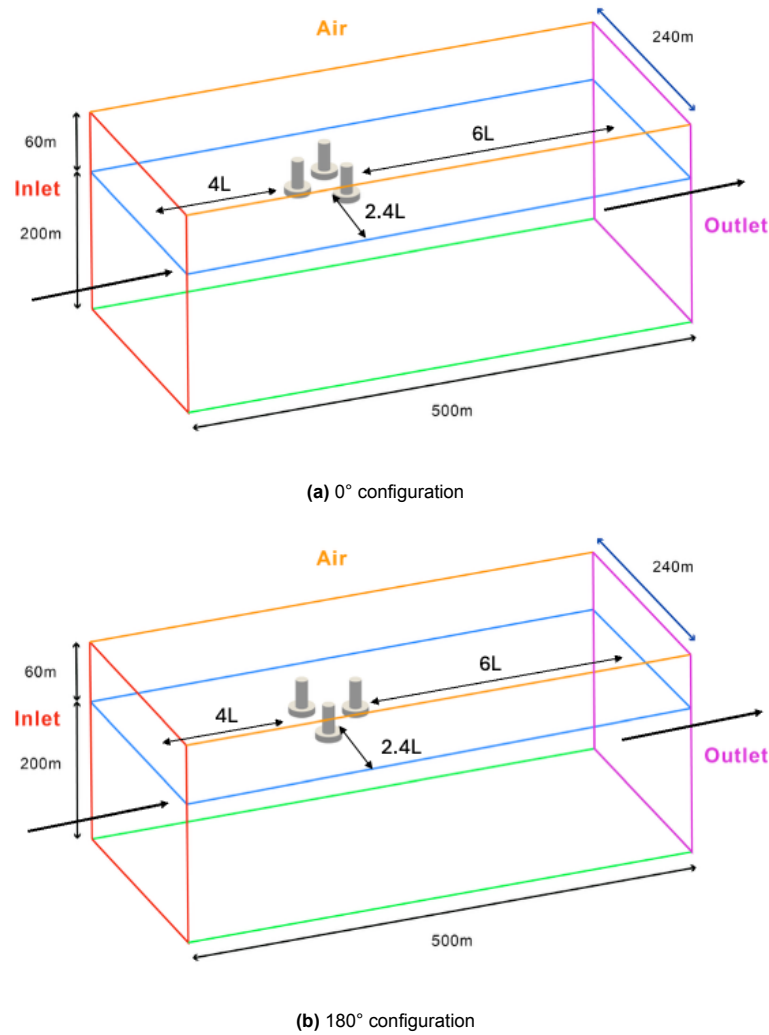
Figure 3.5: Illustration of two towing configurations

For easier notation, Figure 3.6 shows the name convention of the columns in both 0° heading and 180° heading that is used throughout the study.

(a) Naming convention at 0° towing heading

(b) Naming convention at 180° towing heading
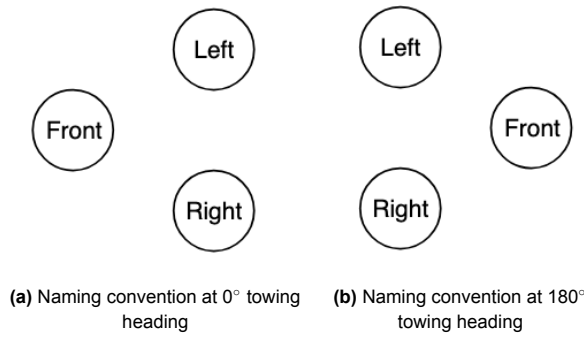
Figure 3.6: Naming convention of the floater geometry for different towing headings

Figure 3.7 shows the drag and lift force directions convention, or sometimes also mentioned as inline and transverse forces on a column in this study.
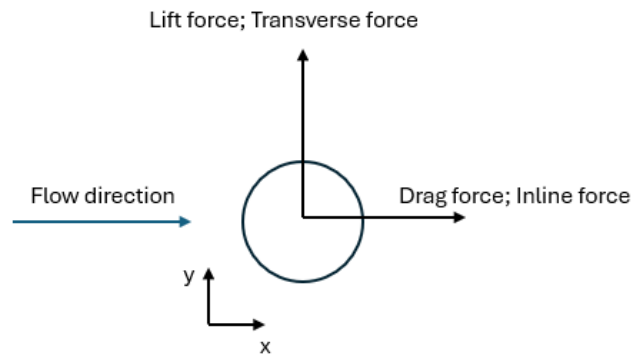
Figure 3.7: Sketch showing drag and lift force direction used in the study

Instead of simulating the towing motion directly, the floater is kept fixed while a uniform inlet velocity equal to the towing speed is applied. This approach replicates the relative velocity between the water and the floater, allowing the hydrodynamic forces to be captured more efficiently. This setup inherently includes the Froude–Krylov force, as the pressure gradient in the flow direction acts on the submerged body and contributes to the overall hydrodynamic load. However, notice that the VIM is not captured in this study since the floater is fixed in place.

Additionally, the floater draft is reduced from the designed installation draft of 20 m to 10 m, based on the findings of Ramachandran [31]. In the study of Ramachandran, a 1:50 model-scale model is used for the experimental tests. This reduced draft has been shown to maintain sufficient stability during wet-towing while reducing drag, which in turn lowers fuel consumption and the required towing power.

Both simulations are conducted in an identical computational domain measuring 500 m in length ($10L$), 240 m in width ($4.8L$), and 260 m in height ($5.2L$), where L is the distance between columns, which is 50 m. The inlet face is $4L$ upstream, the outlet face is $6L$ downstream, and the sides are $2.4L$ from the center of the floater. The water depth is set to 200 m ($4L$), with an additional 60 m of air ($1.2L$) included

above the water surface to capture free-surface effects. These can be seen in Figure 3.5 above. The domain size is chosen based on the reference case of Benitz [5], which aligns with the dimensions of the towing tank at MARIN, where experimental test campaigns have been performed.

Furthermore, damping zones are implemented to reduce reflections. Damping zones are added to the inlet, outlet, and sides. The lengths of the damping zones are set to 100 m ($2L$) at the inlet and outlet, and 20 m at the sides ($0.4L$). The damping zones cover the entire water depth, and damping is applied in both horizontal and vertical directions. An illustration of where damping zones are placed is highlighted and shown in Figure 3.8. These are done by implementing `explicitPorositySource` in `fvOptions`. Linear damping following *Darcy*'s law is used, which is the first-order term in Equation 3.1 [36], where D is the first-order damping coefficient and F the second. However, due to limited information on the function, a coefficient of 500 is set by trial and error. This is applied to all simulations throughout the study.
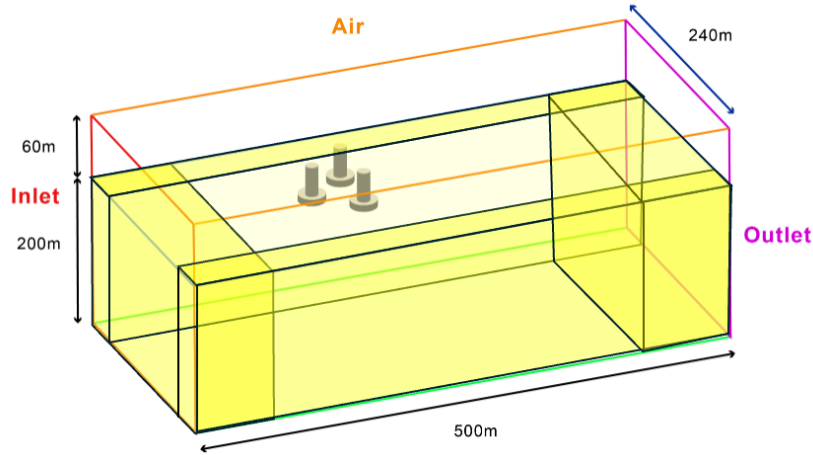
Figure 3.8: An illustration of the positions where damping zones are placed

$$\mathbf{F} = -\left(D\,\mathbf{U} + F\,|\mathbf{U}|\,\mathbf{U}\right) \tag{3.1}$$

The `explicitPorositySource` is understood as an object with small holes on it. Fluids are allowed to pass through, but resistance is added. The amplitude of initial waves generated at the surface of the floater decreases faster at the start of the simulation, however, the effect is limited. The amplitude only decreases to an extent, and the standing waves in the domain still influence the hydrodynamic forces.

Towing speeds of 1, 2, and 3 knots are simulated, and the corresponding Froude numbers and Reynolds numbers are shown in Table 3.4.

Full scale speed [m/s]	Fr	Re
0.514 (1 kn)	0.0474	6.14E+06
1.028 (2 kn)	0.0947	1.23E+07
1.543 (3 kn)	0.1421	1.84E+07

Table 3.4: Test cases for studying the effect of towing heading

3.2.2. Configuration for studying the effect of free surface

A single-phase simulation with double-body assumption (C4) is carried out for a few reasons. First, both Jiang [18] and Liu [25] studied VIM on semi-submersible platforms using single-phase simulation with double-body assumption, the effect of this assumption and the difference compared to multiphase simulation are of interest. Second, the hydrodynamic forces in the multiphase model are influenced by reflection waves, and the single-phase simulation can isolate this.

The double-body assumption is a simplification commonly used in CFD simulations where the free surface is neglected by imposing a symmetry plane at the waterline. This is often used to study the resistance of ship hulls at low Froude numbers, where wave-making effects are minimal and the flow is dominated by viscous and pressure resistance. This assumption is known to be suitable for slender, streamlined structures. However, it is uncertain if it is also suitable for bluff bodies like semi-submersible platforms.

The simulations are done with a $0°$ heading configuration with a draft of 20 m. Both simulations are done at full scale. For the case with a double-body assumption, the model is truncated at the free surface and only includes the part under water. The top boundary, which is at the free surface, is set to a symmetry plane boundary condition. Since no free surface needs to be captured, the mesh for the double-body assumption has a uniform mesh size in the vertical direction. Figure 3.9 shows the side views of the mesh for both simulations.
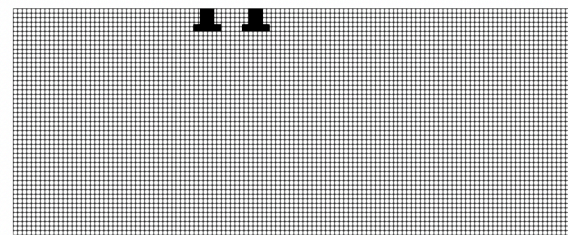
(a) Mesh used for double-body (single-phase) simulation
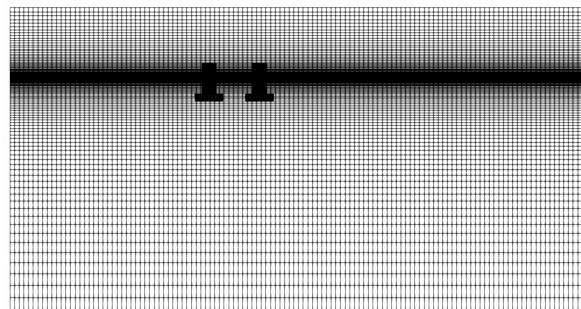
(b) Mesh used for multiphase simulation

Figure 3.9: Side views of the mesh for double-body assumption and multiphase simulation

The solver settings and the boundary conditions follow the ones shown later in this chapter for single-phase and multiphase simulations, respectively. The top boundary of the single-phase model is set to a symmetry plane, which is equivalent to a slip wall in this case.

A towing speed of 2 knots is simulated, and the corresponding Froude number and Reynolds number

are shown in Table 3.5.

Full scale speed [m/s]	Fr	Re
1.028	0.0947	1.23E+07

Table 3.5: Test cases for double-body assumption and multiphase comparison

3.2.3. Configuration for studying the scaling effect

A model scale simulation (C5) is carried out for a few reasons. For example, added layers are not required or less demanding compared to full scale. This saves a lot of cell counts, so the computational cost is lower. Additionally, the time is scaled by the square root of the length scale, which is $\sqrt{50}$ in this case. This means that for a time span of 350 s in full-scale, only approximately 50 s of simulation is needed in model scale. This can dramatically bring down the cost. However, it is shown in Figure 1.6 that the Strouhal number depends on the Reynolds number. It is unclear how representative model-scale simulations are. This case is done to investigate the influence of this Reynolds number mismatch on drag prediction and vortex behavior.

It is known that the main difference between model-scale and full-scale simulations is the Reynolds number mismatch. In this study, the length ratio between model-scale and full-scale is 1:50, and the velocity is scaled following Froude scaling. Due to Froude scaling, the Reynolds number is very different between model scale and full scale, which are shown in Table 3.6. In physical aspect, this means that the full-scale is much more turbulent compared to model scale, and the flow regime are completely different. For a more turbulent flow, the flow can better follow the surface of the structure and delay the separation point.

Two simulations are set up for this study, one is model-scale and the other is full-scale. Both simulations are multiphase, and the floater has a draft of 20 m, which is its designed installation draft. They both have a heading of $0°$, and an illustration of the equivalent setup in full-scale is shown in Figure 3.10.
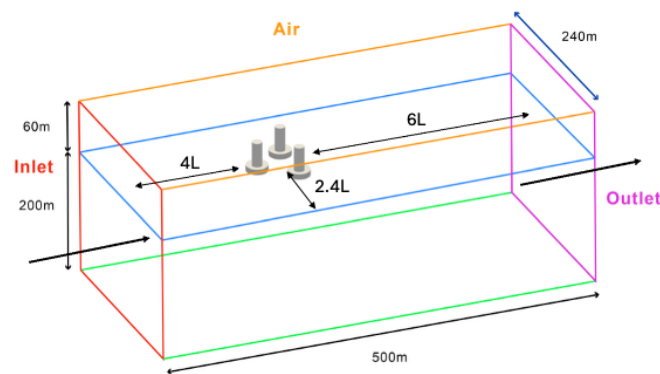
Figure 3.10: Illustration of setup in full-scale

The towing speed is chosen to be 1.028 m/s in full-scale, which is 2 knots. The speed for the model-scale simulation is calculated based on Froude scaling. The corresponding Reynolds numbers and Froude numbers are shown in Table 3.6 below.

Model scale speed [m/s]	Full scale speed [m/s]	Fr	Model scale Re	Full scale Re
0.145	1.028	0.0947	3.48E+04	1.23E+07

Table 3.6: Test cases for model-scale and full-scale comparison

The boundary conditions and the solver settings follow the multiphase settings which are shown in the next section. The only difference is that the max Courant number for the model-scale simulation is set to 0.5 for a smaller time step.

The mesh of the model-scale simulation is also scaled down from full-scale following the procedure in section 3.3. The added layers are not added since the mesh size of 2 cm around the floater is already fine enough for resolving the boundary layer.

3.3. Mesh generation in OpenFOAM

The meshes for the CFD simulations are created by the native meshing functions in OpenFOAM. Mesh generation in OpenFOAM typically involves two steps: an initial background mesh using `blockMesh`, followed by local refinement and geometry-based meshing using `snappyHexMesh`. This combination provides control over domain size and boundary refinement while ensuring compatibility with complex geometries, such as the semi-submersible floater used in this study.

3.3.1. blockMesh

The `blockMesh` function is the native function in OpenFOAM that creates a structured, hexahedral mesh based on manually defined vertices, faces, and blocks. It is used to generate the background mesh that defines the overall computational domain. In this study, the size of the background mesh in the horizontal direction is chosen to be 4 m. In the vertical direction, to have sufficient resolution for the water surface, the size of the mesh gradually decreases towards the water surface. For mesh 1 m above and below the water surface, a mesh size of 10 cm is used. Figure 3.11 is a side view that shows how the mesh is refined in the vertical direction.
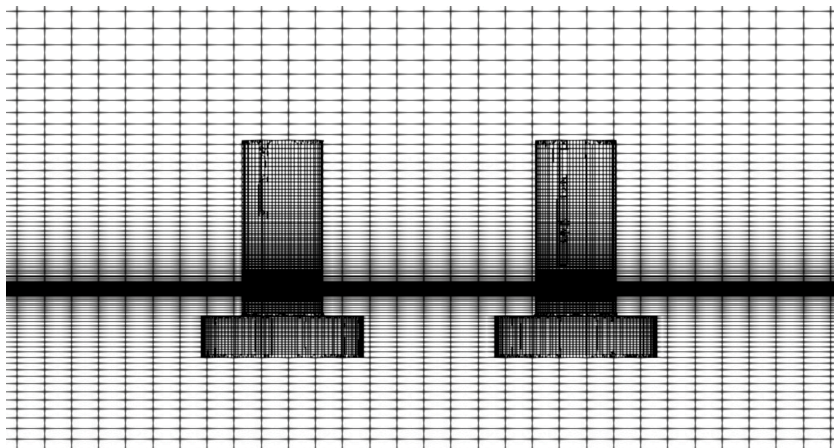
Figure 3.11: Mesh refinement around water surface

3.3.2. refineMesh

The utilities `topoSet` and `refineMesh` are employed to conduct local mesh refinement in regions closer to the surface. `topoSet` is used to select cell sets based on user user-defined box. These sets are then passed to `refineMesh`, which splits all the selected cells in half in user-defined directions. This approach allows refinement in only the horizontal plane and not the vertical direction to have a cell count under control.

From the 4 m size background mesh, two `refineMesh` commands are done to have a mesh size of 2 m and eventually 1 m around the floater to preserve the geometry of the floater. Figure 3.12 is an example of a top view of the mesh of one case that shows how the mesh is refined.
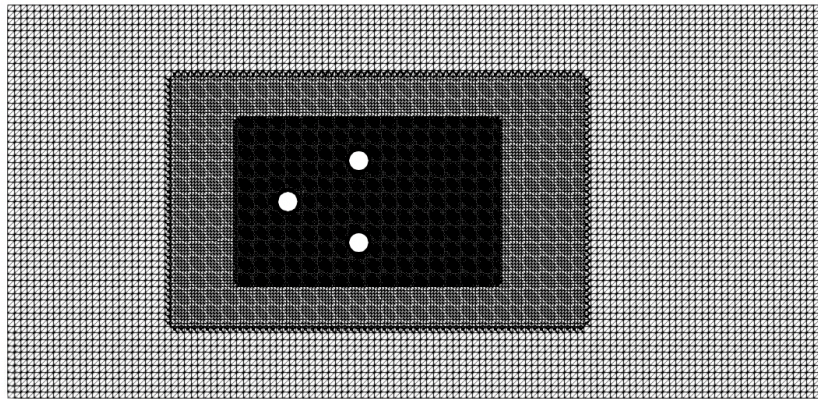
Figure 3.12: Top view of the mesh

3.3.3. snappyHexMesh

The `snappyHexMesh` function performs automatic mesh refinement around a provided STL geometry, which is the model in Figure 3.3 built in Rhino. It uses the background mesh generated from `blockMesh` and performs three main steps.

The first step is castellated mesh generation. Cells that intersect with the geometry surfaces are refined for the resolution of the geometry. The refinement level is set to 1, which means the cells that intersect with the geometry surfaces are split once again. This gives a mesh size of 0.5 m on the surface of the floater. Also, the cells that are not intersecting with the geometry surface and are inside the geometry are removed.

The next step is surface snapping. In this step, the cells are snapped onto the surface of the geometry. This surface snapping step is crucial for a smooth and high-quality mesh of the geometry.

Finally, the last step is layer addition. This is used when the mesh is not fine enough for the boundary layer resolution. Wall functions are used in this study; therefore, the target y^+ is roughly 50. The first layer thickness can then be estimated based on the formulas shown in subsection 2.2.4, which is 1 cm. The expansion ratio is chosen to be 1.2 to ensure a smooth transition. Four layers are added to the surface of the geometry. However, the method that OpenFOAM uses is squeezing the layer addition from the inside of the geometry. Therefore, not too many or too thick layers can be added since it will

distort the existing mesh on the outside and cause mesh quality issues. Figure 3.13 shows how the layers are added around the floater column.
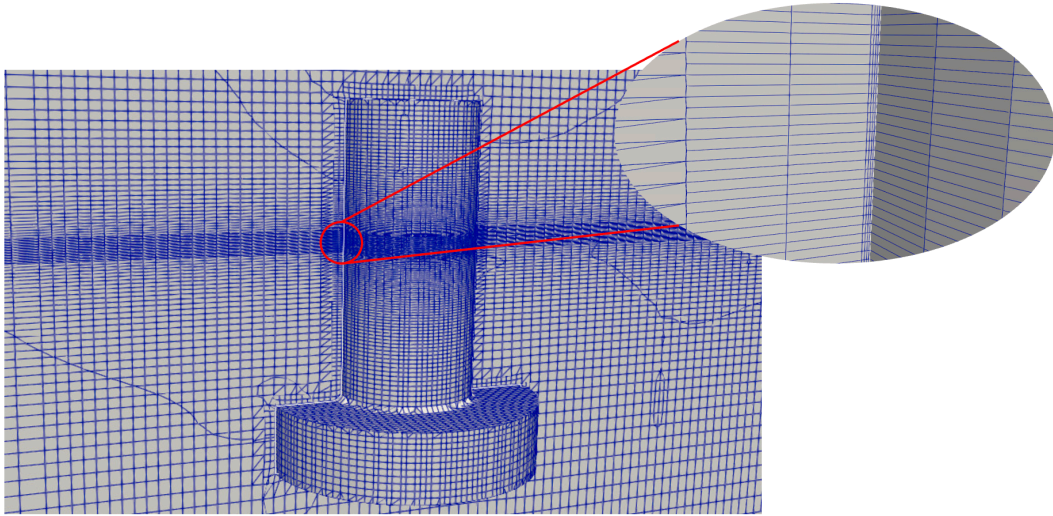
Figure 3.13: Added layers

3.4. Solver setup and computational methods

The different solvers used for multiphase simulations and single-phase simulations, computing method, and residuals regarding the numerical solver are documented in this section.

3.4.1. Solver

Two different solvers provided by OpenFOAM were employed depending on the type of flow simulated. For single-phase flow cases, the `pimpleFoam` solver was used, while for multiphase flow simulations involving a free surface, the `interFoam` solver was adopted.

The `pimpleFoam` solver is designed for transient, incompressible, and turbulent flows. It combines the SIMPLE and PISO algorithms through the PIMPLE algorithm, allowing for stable time-stepping with larger Courant numbers in transient simulations. This solver is particularly suitable for evaluating the flow-induced forces on the floater in calm water without any effect from the free surface.

For multiphase simulations, the `interFoam` solver was used. It solves the two-phase incompressible Navier–Stokes equations using the Volume of Fluid (VOF) method to capture the interface between air and water. This was essential for resolving free surface effects and wave-making resistance interactions in the wet-towing scenarios. This is also more representative of a real-life scenario.

Both solvers are configured to run in transient mode using the Crank-Nicolson time integration scheme with a blending factor of 0.9. This approach provides second-order local accuracy while introducing slight numerical damping to enhance the stability of the simulations in highly transient simulations. Time steps were dynamically adjusted to maintain a global Courant number around 5, which gives time steps of around 0.05 s. This is a balance between accuracy and efficiency that still provides good resolution for unsteady flow features.

3.4.2. Parallel computing

All simulations are performed using parallel computing to reduce computation time and enable high-resolution mesh refinement. The simulations are executed on the DelftBlue high-performance computing (HPC) cluster [1] provided by TU Delft. Depending on the complexity of the case, such as mesh size, geometry detail, and the inclusion of multiphase flow, each case is run using from 8 up to 24 CPU cores. As a reference, a full-scale multiphase simulation requires roughly 40 hours with 24 CPU cores running in parallel to complete a simulation of 350 s.

3.4.3. Residuals

Full-scale multiphase simulations are quite computationally heavy and take a long time to complete. Therefore, to ensure that the simulations are numerically correct and to find the balance for the number of correctors used. A Python script that reads the residuals from the output `solver.log` file is written to monitor the simulations in real-time.

When running a simulation, the residual of each property is monitored to ensure that the simulation is running efficiently. Figure 3.14 shows the residual of each property of a multiphase simulation. In this case, 5 `PIMPLE` iterations are run in each timestep. The initial residual drops down in each iteration, and when it moves on to the next timestep, the residual increases again. `p_rgh` determines the number of iterations used per timestep, as it can be seen that the residual of `p_rgh` is not decreasing effectively after 5 iterations.
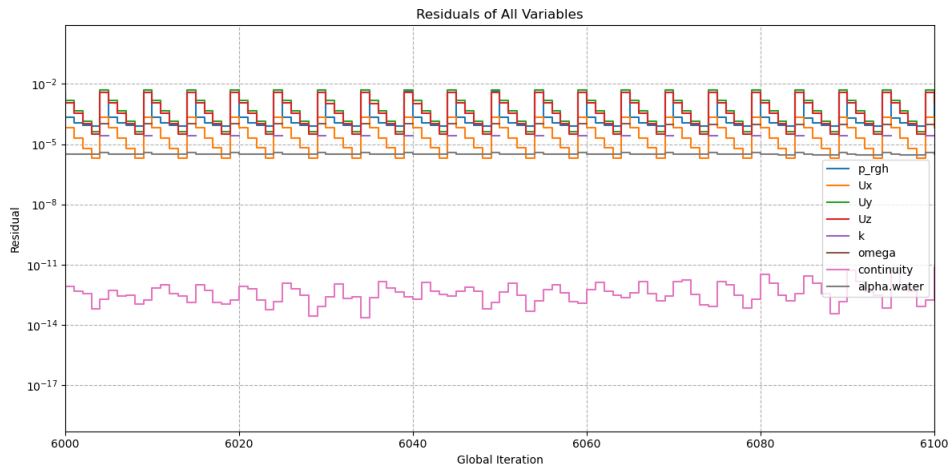
Figure 3.14: An example of the residuals of each property during a simulation

3.5. Boundary condition

The boundary condition setup is divided into two categories: one for single-phase simulations using `pimpleFoam`, and another for multiphase simulations using `interFoam`. Each case involves specific treatment of the domain boundaries to reflect the intended physical behavior while maintaining numerical stability.

3.5.1. Single-phase simulations

The single-phase simulations attempt to simulate the flow with a double-body assumption. The computational domain consists of the following patches: inlet, outlet, sides, bottom, top, and wall

(representing the floater).

- **Inlet**: A velocity inlet boundary condition is applied using `fixedValue` for velocity (`U`), prescribing a uniform velocity vector corresponding to the towing speed. A `zeroGradient` condition is used for the pressure (`p`), allowing it to adjust naturally to the flow. The turbulence properties (`k` and ω) are also simply set to a fixed value.

- **Outlet**: A pressure outlet boundary condition is imposed using `fixedValue` for pressure (`p`) setting it to 0. This implies that the pressure has recovered and will match the pressure of the far field. The velocity `U` is set to `zeroGradient` to allow natural adjustment. The turbulence properties (`k` and ω) are also set to `zeroGradient` without constraints.

- **Wall (Floater surface)**: A no-slip condition is applied setting the velocity (`U`) to `fixedValue (0, 0, 0)`. The pressure (`p`) is set to `zeroGradient` to allow natural adjustment depending on the velocity. For the turbulence properties (`k` and ω), `kqRWallFunction` and `omegaWallFunction` are used to model the near-wall behavior. The turbulence viscosity (`nut`) is set to `nutUSpaldingWallFunction` using Spalding's wall function introduced in section 2.3.

- **Top, Sides, and Bottom**: The sides and bottom are all assumed to be far enough to have any influence on the flow. The top face in the single-phase simulations is meant to mirror the flow, assuming double-body and ignoring free surface effects. Therefore, all sides, bottom, and top are set to `symmetryPlane`. `symmetryPlane` states that there is no flow crossing the boundary, i.e., no normal flow, and no shear stress on the boundary.

An overview of the boundary conditions for single-phase simulations is shown in Table 3.7 below.

Patch	U	p	k / ω	nut
Inlet	fixedValue	zeroGradient	fixedValue	calculated
Outlet	zeroGradient	fixedValue (0)	zeroGradient	calculated
Wall (floater)	fixedValue (0 0 0)	zeroGradient	kqRWallFunction / omegaWallFunction	nutUSpalding WallFunction
Top, Sides, Bottom	symmetryPlane	symmetryPlane	symmetryPlane	symmetryPlane

Table 3.7: Boundary conditions for single-phase simulations with the double-body assumption

3.5.2. Multiphase simulations

In the multiphase simulations, the computational domain is similar, except that the top patch is air instead of the water surface. An additional property is the `alpha.water` that describes the volume fraction between air and water. Furthermore, `p` is here `p_rgh` instead. It is the pressure after correction for the static pressure contributed by gravity as shown in Equation 3.2.

$$p\_rgh = p - \rho gh \qquad (3.2)$$

- **Inlet**: A fixed inflow is prescribed for all fields. The velocity (`U`) and phase fraction (`alpha.water`) are set using `fixedValue`, ensuring a uniform flow field and consistent water level. The pressure (`p_rgh`) is set using `fixedFluxPressure` to maintain correct pressure-velocity coupling. Turbulence properties (`k`, `omega`, `nut`) are also set to fixed values.

- **Outlet**: The outlet allows natural flow and wave exit. A `variableHeightFlowRate` is applied for `alpha.water` to maintain a stable free surface. The velocity (`U`) uses `outletPhaseMeanVelocity`, and pressure is set to `zeroGradient`. Turbulence fields use `inletOutlet` conditions, allowing outflow without enforcing specific values, and preventing backflow.

- **Left / Right**: These lateral boundaries are treated as `symmetryPlane`, assuming a sufficiently wide domain to avoid sidewall effects. This enforces zero normal gradient and no shear across the plane, mimicking an unbounded domain.

- **Top**: The top boundary allows air to leave the domain. It applies `inletOutlet` for `alpha.water` and turbulence fields, `pressureInletOutletVelocity` for velocity, and `totalPressure` for `p_rgh`, which sets a reference pressure of 0 and adjusts the velocity to reach this total pressure.

- **Bottom**: The bottom boundary is also treated as a `symmetryPlane`, assuming the depth is sufficient to neglect seabed effects. This avoids introducing artificial resistance or reflection.

- **Wall (Floater surface)**: A no-slip condition is applied for velocity (`U`) using `fixedValue`. The pressure uses `fixedFluxPressure` to ensure proper pressure-velocity coupling. The phase fraction is set to `zeroGradient`, while turbulence quantities use appropriate wall functions: `kqRWallFunction`, `omegaWallFunction`, and `nutUSpaldingWallFunction`.

Patch	alpha.water	U	p_rgh
Inlet	fixedValue	fixedValue	fixedFluxPressure
Outlet	variableHeight FlowRate	outletPhaseMeanVelocity	zeroGradient
Left / Right	symmetryPlane	symmetryPlane	symmetryPlane
Top	inletOutlet	pressureInletOutletVelocity	totalPressure
Bottom	symmetryPlane	symmetryPlane	symmetryPlane
Wall (floater)	zeroGradient	fixedValue	fixedFluxPressure

Table 3.8: Boundary conditions for `alpha.water`, `U`, and `p_rgh` in multiphase simulations

Patch	k	omega	nut
Inlet	fixedValue	fixedValue	fixedValue
Outlet	inletOutlet	inletOutlet	inletOutlet
Left / Right	symmetryPlane	symmetryPlane	symmetryPlane
Top	inletOutlet	inletOutlet	zeroGradient
Bottom	symmetryPlane	symmetryPlane	symmetryPlane
Wall (floater)	kqRWallFunction	omegaWallFunction	nutUSpalding WallFunction

Table 3.9: Boundary conditions for `k`, `omega`, and `nut` in multiphase simulations

3.6. Turbulence modeling and near-wall treatment

The URANS (Unsteady Reynolds-averaged Navier-Stokes) modeling approach is used in this research. Unlike RANS, it can also capture time-dependent flow features such as vortex shedding. It is chosen over LES due to its lighter computational cost.

For the turbulent model, the k-ω SST model is used. This is because it uses the standard k-ω model

near the wall, and the standard k-ϵ model in the free-stream, where they both excel.

Spalding's wall function is used throughout the study. The reason is due to its continuity. Towing speeds from 1 to 3 knots are used in this study, and with Spalding's wall function, a y^+ of 1 to 300 is acceptable. This allows the mesh to be extensively used, instead of creating a mesh dedicated to each speed. Figure 3.15 shows an example at towing speed of 1 knot, most of the surface have y^+ of around 100.
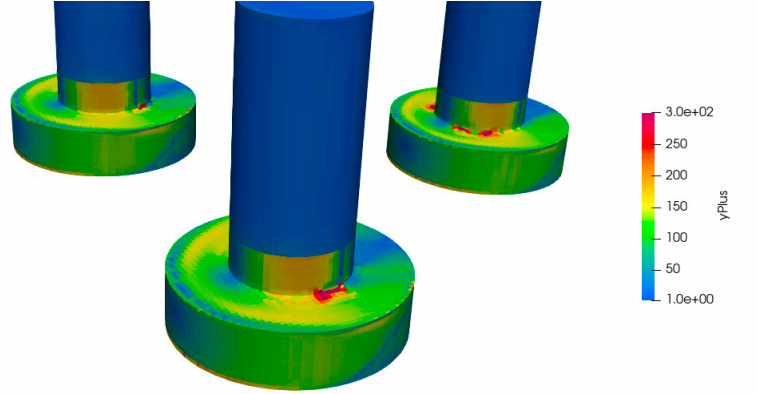
Figure 3.15: y^+ contour of towing speed of 1 knot averages roughly 100 after stabilize

3.7. Estimation of sway natural period

For checking if vortex shedding can cause resonance in the sway motion, some simple calculation is done to obtain an estimation on the sway natural period of the towing system. The configuration C4, full-scale single-phase model, with $0°$ heading is used since vortex shedding is only observed in this case. An illustration of the towing system is shown in Figure 3.16, where F_D is the drag force, F_R is the restoring force, and L is the towing line length, dy is the offset in sway direction.
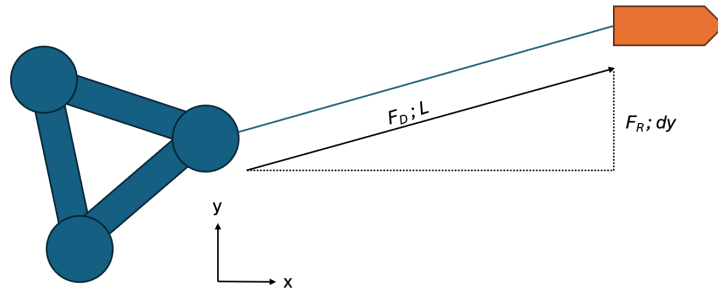
Figure 3.16: Illustration showing the towing system with the configuration C4

The assumption here is that the platform is being towed with a constant speed and the tension equals to the drag force. From Figure 3.16, it can be seen that at a fixed L and dy, the restoring force increases with the drag force. To be more conservative, a drag coefficient of 0.7 is used. At a towing speed of 2 knots, the restoring stiffness over the length of the towing line at different offset distance (dy) can be simply calculated with the geometry as shown in Figure 3.17. The stiffness lowers as the length of the towing line increases.
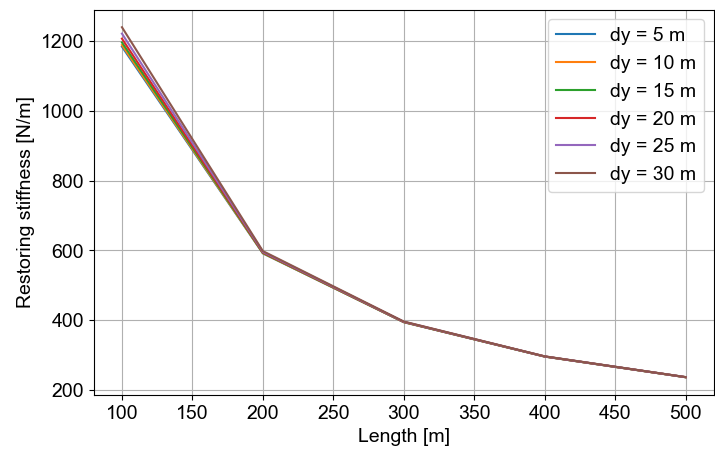
Figure 3.17: Restoring stiffness of the towing system at a towing speed of 2 knots over towing line length and offset distance

Subsequently, the natural period of sway motion of the towing system can then be estimated. Assuming an added mass coefficient of 1, the natural period over the length of towing line and offset distance is shown in Figure 3.18.
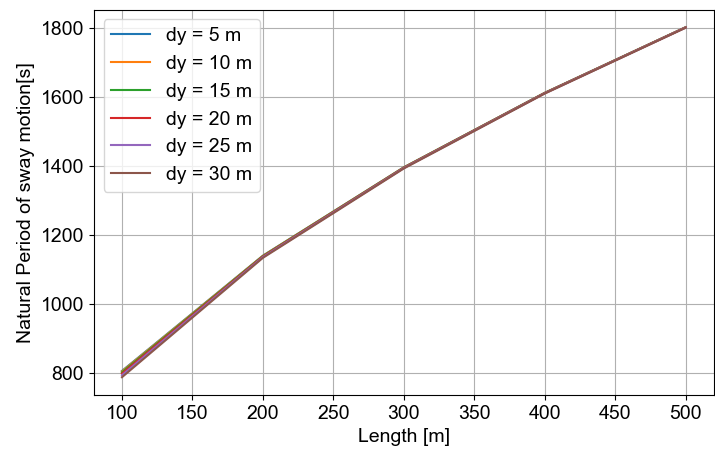
Figure 3.18: Natural period of sway motion at a towing speed of 2 knots over towing line length and offset distance

From Figure 3.18, looking at the extreme case, the natural period is about 800 s at $L = 100$ m.

4

Validation and verification

It is crucial for CFD simulations to conduct a validation and verification study because of the high sensitivity of CFD simulations to the mesh quality, and to ensure the reliability and accuracy of the numerical predictions. Therefore, this chapter presents a mesh sensitivity study and the reproduction of a benchmark case from the literature.

4.1. Mesh dependency test

A mesh dependency test is shown to demonstrate that the numerical results are not sensitive to the discretization of the domain. This step is important to confirm that the computed hydrodynamic forces and flow features are independent of the mesh resolution.

The mesh dependency is done on the case shown in Figure 4.1 below. The draft of the floater is 10 m, and the simulation is in full scale, with a towing speed of 1 knot, i.e., 0.514 m/s.
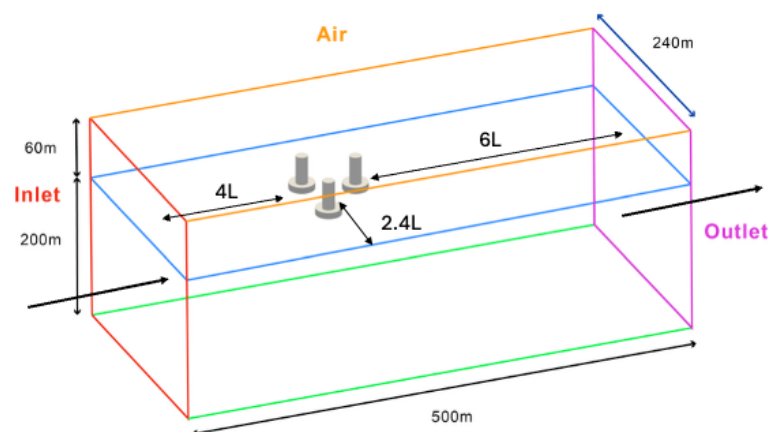
Figure 4.1: Case for mesh dependency study

Three different resolutions are used for meshing: one with a coarse mesh, one with a fine mesh, and one in between. All the relative mesh sizes of the refinement regions to the base mesh size are kept the same, only the sizes of the base mesh are changed. The meshes are created following the same procedure shown in section 3.3. The number of cells in fine mesh, mid mesh, and coarse mesh is around 2 million, 3 million, and 5.8 million, respectively. Figure 4.2 presents the mesh with the finer and coarser resolutions.

(a) Fine mesh
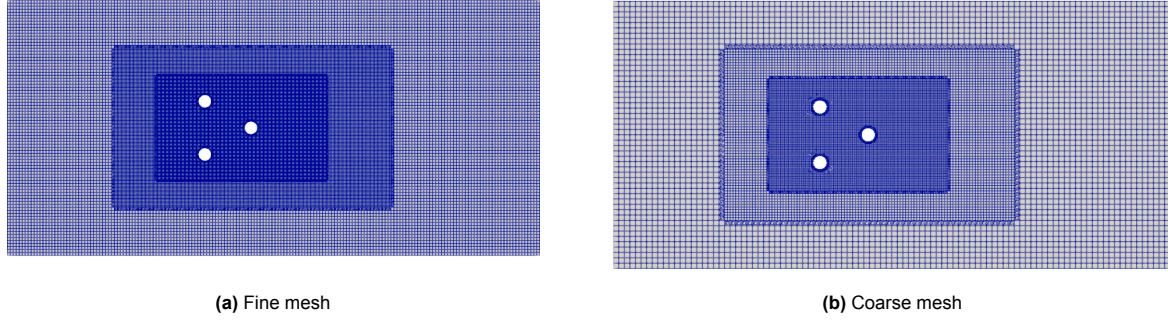
(b) Coarse mesh

Figure 4.2: Comparison between fine and coarse mesh resolutions

The solver settings and the boundary conditions follow the ones for multiphase shown in chapter 3. The mean drag force on the right column is chosen as the target value for the comparison.

To find the asymptotic solution, the curve of mean drag over the number of cells is fitted to Equation 4.1 shown below. The $F_{solution}$ is the solution that the drag force is converging to, N is the number of cells, a and p are coefficients for fitting the curve.

$$F = F_{solution} + \frac{a}{N^p} \tag{4.1}$$

The fitted curve is shown as the red dotted curve in Figure 4.3 below, and $F_{solution}$ is found to be around 15.7 kN. Looking at the relative error shown on the second axis, the relative errors are approximately 1%, 6%, and 11% compared to $F_{solution}$.
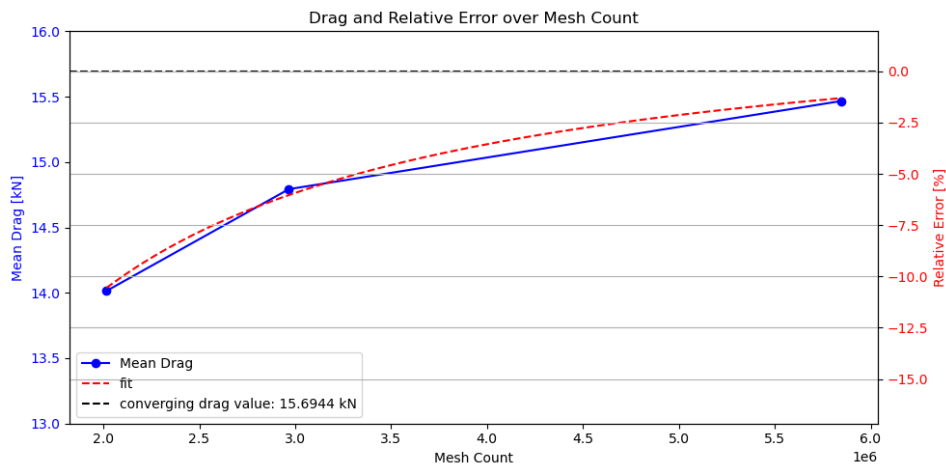
Figure 4.3: The mean drag force and relative error over the number of cells

Table 4.1 below shows the mean inline force and the relative errors of the mesh with different resolutions.

	Number of cells	Mean drag force [kN]	Relative error
Coarse	$2,016,297$	14.01	$-11\,\%$
Mid	$2,966,958$	14.79	$-6\,\%$
Fine	$5,846,580$	15.47	$-1\,\%$

Table 4.1: Number of cells and mean inline force on the right column of three levels of refinement mesh

It is seen that from the coarse mesh to mid-resolution mesh, the number of cells is increased by less than 1 million, but the relative error decreases by 5%. In contrast, from the mid-resolution mesh to the fine mesh, the number of cells is increased by roughly 3 million, and the relative error decreases by the same amount.

The results demonstrate that the mid-level refinement mesh has an acceptable accuracy of balancing the accuracy and the computational cost. Therefore, all the cases of different flow speeds are computed with the mid-level refinement mesh.

4.2. Validation case

To validate the setup of simulations, the cases found in literature [5] are replicated. The simulation setup is shown in Figure 4.4. The draft of the floater is 20 m. The simulation is in full scale, but the ones done in the literature [5] are in model scale. The reasons are that no full-scale simulation is found for validation. Furthermore, since the main simulations are in full-scale, it is better to ensure that the full-scale simulations are correct.
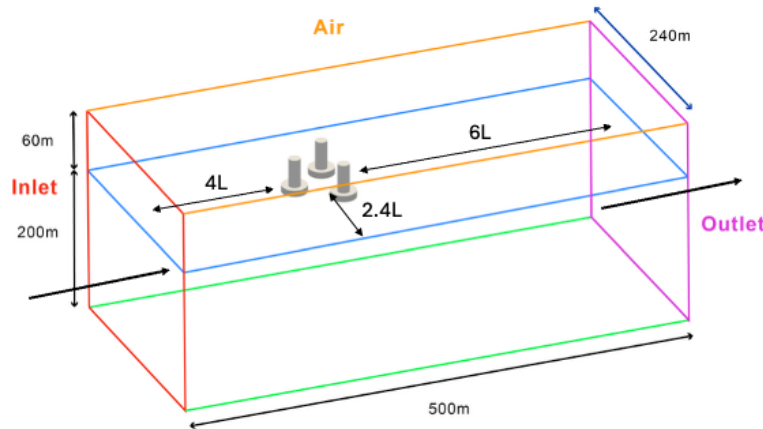
Figure 4.4: Validation case setup

The mesh is set up the same way as shown in section 3.3. The boundary conditions are set up following the multiphase boundary conditions shown in section 3.5. The difference compared to [5] is that no-slip boundary conditions are used on the velocity on the sides in the literature.

The turbulence model used in the literature is `Spalart-Allmaras`, for the reason of providing results matching best with the experimental results. However, in this study, a more general k-ω SST model is used. It provides a good near-wall accuracy and is also less sensitive to the free-stream, as shown in Table 2.3.

For the wall function, the *Spalding*'s wall function is used both in the literature and in this study, as it has a lower requirement on the y^+ values.

Two regions of damping zones are added near the water surface, 100 m from the inlet and the outlet, to suppress the reflections. This is because the negative drag seen in Figure 4.5b is questionable unless explained by reflections.

4.2.1. Test cases
The three cases tested are 0.3 m/s, 0.6 m/s, and 1.0 m/s in full scale as shown in Table 4.2.

Full-scale speed [m/s]	Fr	Full scale Re
0.3	0.0277	3.6E+06
0.6	0.0553	7.2E+06
1.0	0.0922	1.2E+07

Table 4.2: Test cases for validation

4.2.2. Validation results
The inline and transverse forces on each column with a flow speed of 0.6 m/s are presented here for further comparison. Figure 4.5b shows the inline and transverse force from literature [5], and Figure 4.5a shows the forces from this study.

(a) Inline and transverse force from present study   **(b)** Inline and transverse force from literature [5]
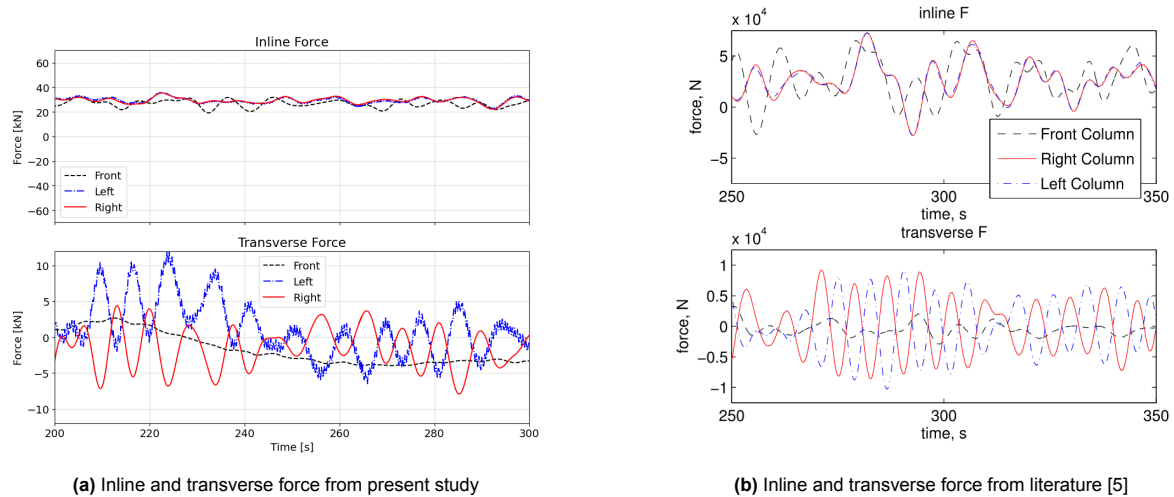
Figure 4.5: Comparison of inline and transverse force of a flow speed of 0.6 m/s

The forces are plotted over the same range. It can be seen that the amplitude of the inline force is much smaller in Figure 4.5a than in Figure 4.5b. This is likely due to the transient reflection waves depending on the startup and is pointed out in the next section. Looking at the lift forces, the left and

right columns are out of phase, which is in agreement with the literature, and the amplitudes of the lift forces are comparable, which are both within 10 kN.

(a) Frequency spectrum from the present study

(b) Frequency spectrum from literature [4]
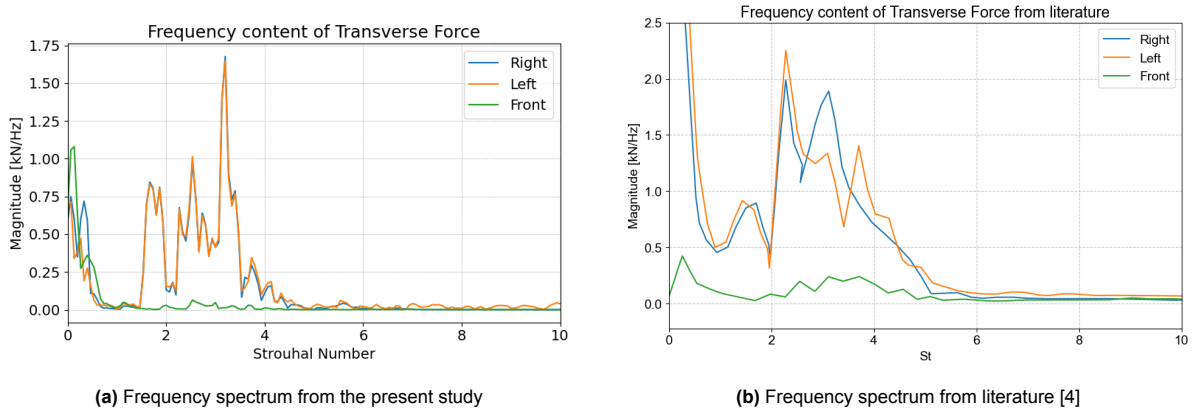
Figure 4.6: Frequency spectrum verification of the transverse force

In the literature, the columns are separated into the upper column and base column, while in the present study, they are not. The frequency spectra of the upper columns are extracted and compared. Comparing the frequency content of the lift force shown in Figure 4.6, both the peaks of the left and right columns in the present data and the literature fall between Strouhal numbers of 2 and 4. However, these peaks found in this study are actually the standing wave frequencies in the transverse direction, instead of the vortex shedding frequencies mentioned in literature [4]. This will be proved and further discussed later in chapter 5.

Figure 4.7 shows the time series of the drag force of the full floater in three different speeds. The time series are all oscillating around a mean value, which shows that the drag force is quite steady at this time.
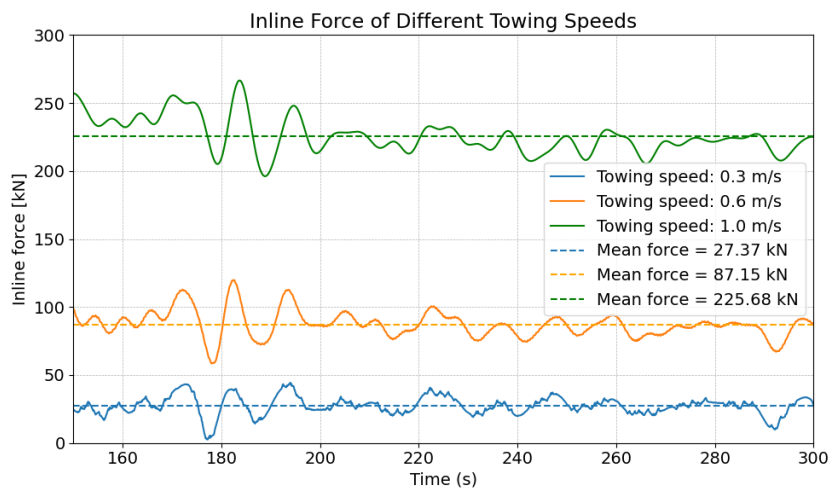
Figure 4.7: Time series of drag force of the full floater at various speeds

The mean drag forces of the full floater in three towing speeds are plotted in Figure 4.8 and compared to the results in literature [5].
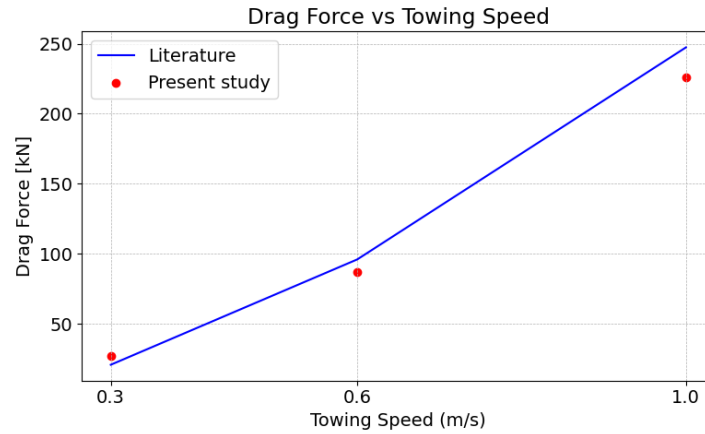
Figure 4.8: Validation of mean drag force of the full floater

The difference between present data and the literature is 31%, 9%, and 9% for 0.3 m/s, 0.6 m/s, and 0.9 m/s, respectively. The difference is much higher in 0.3 m/s because the absolute drag values are relatively low.

At these Reynolds numbers, the theoretical drag coefficients for cylinders are found to be around 0.7 from Figure 2.2. This shows that the theoretical drag coefficients are overestimating the drag forces compared to the results from CFD simulations.

	0.3 m/s	0.6 m/s	1.0 m/s
Present mean drag [kN]	27.37	87.15	225.68
Literature mean drag [kN]	20.86	96.05	247.37
Present mean drag coefficient	0.63	0.50	0.47
Literature mean drag coefficient	0.48	0.55	0.51
Error [%]	31	−9	−9

Table 4.3: Mean drag and differences of present data and literature

The source of differences could be attributed to a few things below. One is the Reynolds number mismatch, where model-scale simulations are in the order of 10^4 and full-scale is in 10^6. This can cause the flow to separate at a different position, which changes the wake and the pressure distribution. Another source could be the turbulence model, the one that is used in the literature [5] is the `Spalart-Allmaras` turbulence model, which the k-ω `SST` model is used in this study. Also, the mean drag coefficient from the literature is not monotonic to the flow speed, which might also indicate some error in the data.

<div style="text-align: right; font-size: 4em;">5</div>

Results and discussion

5.1. Towing configuration: $0°$ versus $180°$

Towing speeds of 1, 2, and 3 knots are tested. The cases with towing speeds of 2 knots are discussed further here. At a towing speed of 2 knots, the Reynolds number is $1.23E+07$.

5.1.1. Standing waves

First, looking at the $0°$ towing configuration, the lift and drag force time series and FFT of each column are shown in Figure 5.1 and Figure 5.2 below. The FFT is calculated by detrending a linear DC component from the signal, then applying a *hanning* window to reduce the spectral leakage from the ends. This method is used throughout the study. The simulation length is initially chosen following the literature as shown in Figure 4.5, since the frequency of the target oscillation is roughly 0.15 Hz. Looking at the drag force, the drag forces on the left and right columns are almost identical, while the front column has a slightly lower drag. The lift forces on the left and right columns are completely out of phase, which makes sense since they are symmetric and are also seen in Figure 4.5.
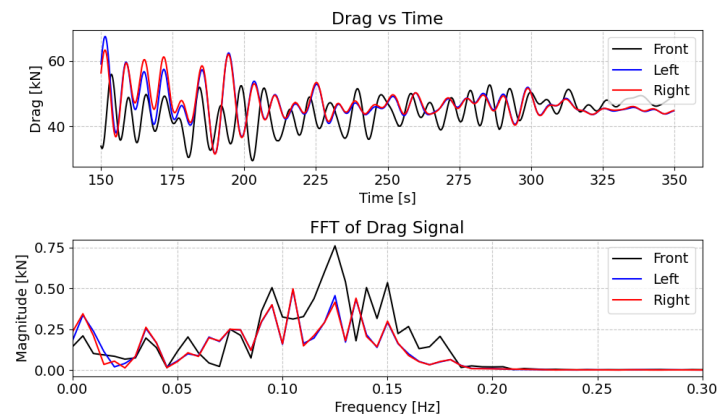
Figure 5.1: Drag force time series and FFT in $0°$ heading
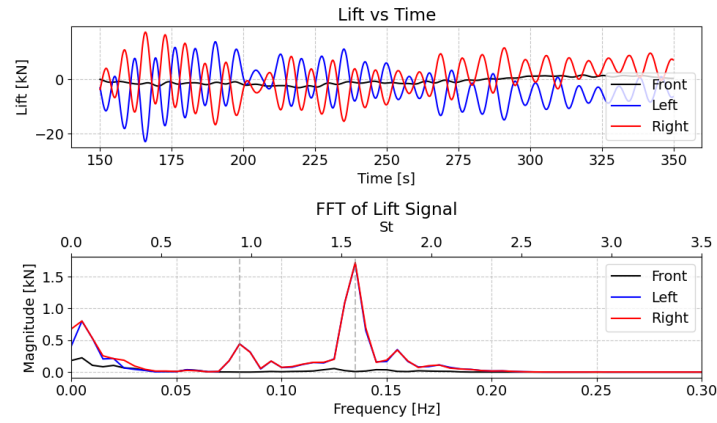
Figure 5.2: Lift force time series and FFT in 0° which is later found still in transient

To identify the source of the lift force oscillation, the vorticity field at $z = -2$ m and at $t = 305$ s is shown in Figure 5.3. However, the oscillation period of the asymmetric wake is found to be much lower than the dominant peaks in the lift force FFT at 0.08 and 0.14 Hz. These main oscillation frequencies are then suspected to be the numerical reflections due to the transient at the beginning of the simulation. To confirm that, the free surface elevation is shown in Figure 5.4. The figure shows that there are reflection waves in the domain affecting the results.
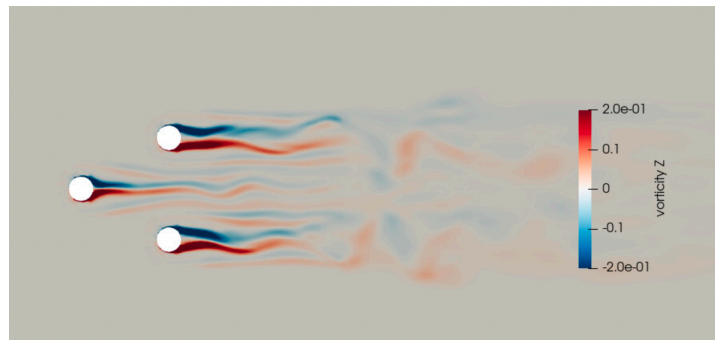
Figure 5.3: Vorticity field at $z = -2$ m plane at $t = 305$ s of 0° heading showing wake asymmetry
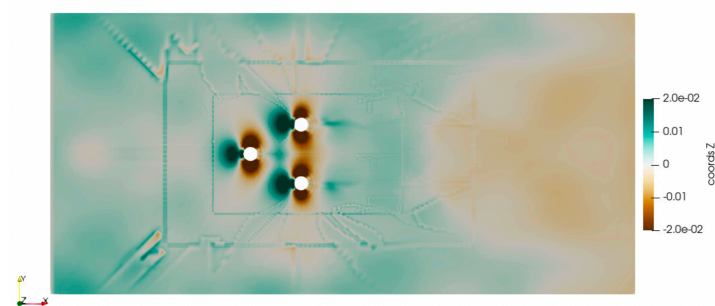
Figure 5.4: Free surface elevation at $t = 305$ s

An example time step of pressure over a line at $z = -2$ m and through the left and right columns is

shown in Figure 5.5. An animation over time is made, and symmetric pressure changes due to elevation change from the sides of the domain are spotted. Even though the elevation difference is only less than 5 cm in full-scale, the pressure difference is still influencing the integrated forces quite a lot.
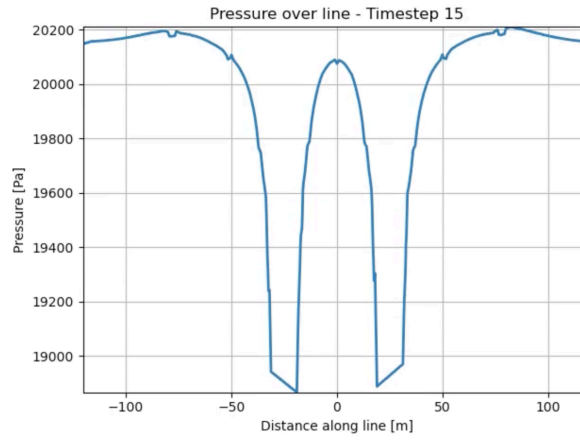
Figure 5.5: Pressure over line $z = -2$ m and through the left and right columns

Standing wave frequencies are calculated with the dispersion relation shown in Equation 5.1, where ω is the natural period, g is the gravity, k is the wave number, and h is the water depth. The standing wave modes observed in the domain correspond to the boundary condition of two free ends, forming a free–free standing wave system. The first 6 modes of standing wave are calculated, and the corresponding wavelengths and frequencies are shown in Table 5.1. The frequency peaks at 0.08 Hz and 0.14 Hz correspond to the frequencies of standing wave modes $n = 2$ and 6. The shapes of these standing wave modes are shown in Figure 5.6. They are found to be the symmetric standing wave modes.

$$\omega^2 = gk \tanh kh \tag{5.1}$$

n	Wavelength [m]	Frequency [Hz]
1	480	0.05673
2	240	0.08065
3	160	0.09878
4	120	0.11407
5	96	0.12753
6	80	0.13970

Table 5.1: Wavelength and frequency for different standing wave modes
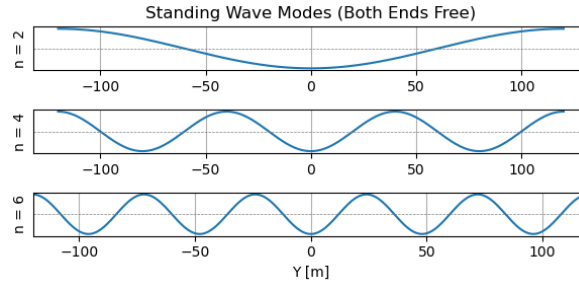
Figure 5.6: Standing wave modes of $n = 2, 4, 6$

This indicates that the frequencies at 0.08 Hz and 0.14 Hz are due to standing waves in the domain. Furthermore, since these are symmetry modes, it also explains that this oscillation is absent in the lift force on the front column.

The same also goes for the streamwise direction that is affecting the drag force. However, since the length of the domain in the streamwise direction is much larger, there are even higher wave modes in the streamwise direction. As seen in Figure 5.1, there is a wide range with various peaks, rather than only a few dominant ones.

This shows that although damping zones are implemented, the effect is limited. It is observed that the force oscillations due to the reflections decrease faster compared to models without damping zones. However, it only decreases to a certain extent.

For the above reasons, the magnitudes of the lift forces are not focused on, as they are affected by the reflections and are uncertain about their representation. However, the low-frequency oscillation due to wake asymmetry can still be seen after applying a moving average window. Also, the mean drag forces are still considered accurate as they are averaged over a long period.

5.1.2. Forces and the flow field

The effective time length of 200 s is too short for the long-period oscillation. Therefore, the simulation was extended to 650 s. To isolate the effects of the reflections, a rolling window of 50 s is applied to calculate the moving average for a better view on the low-frequency oscillation. The Strouhal number normalizes the lift frequency based on the diameter of the upper column, which is 12 m. Figure 5.7 shows the lift force and the FFT of the 0° heading case and the 180° heading case.

(a) Smoothed lift force time series and FFT at 0° heading

(b) Smoothed lift force time series and FFT at 180° heading
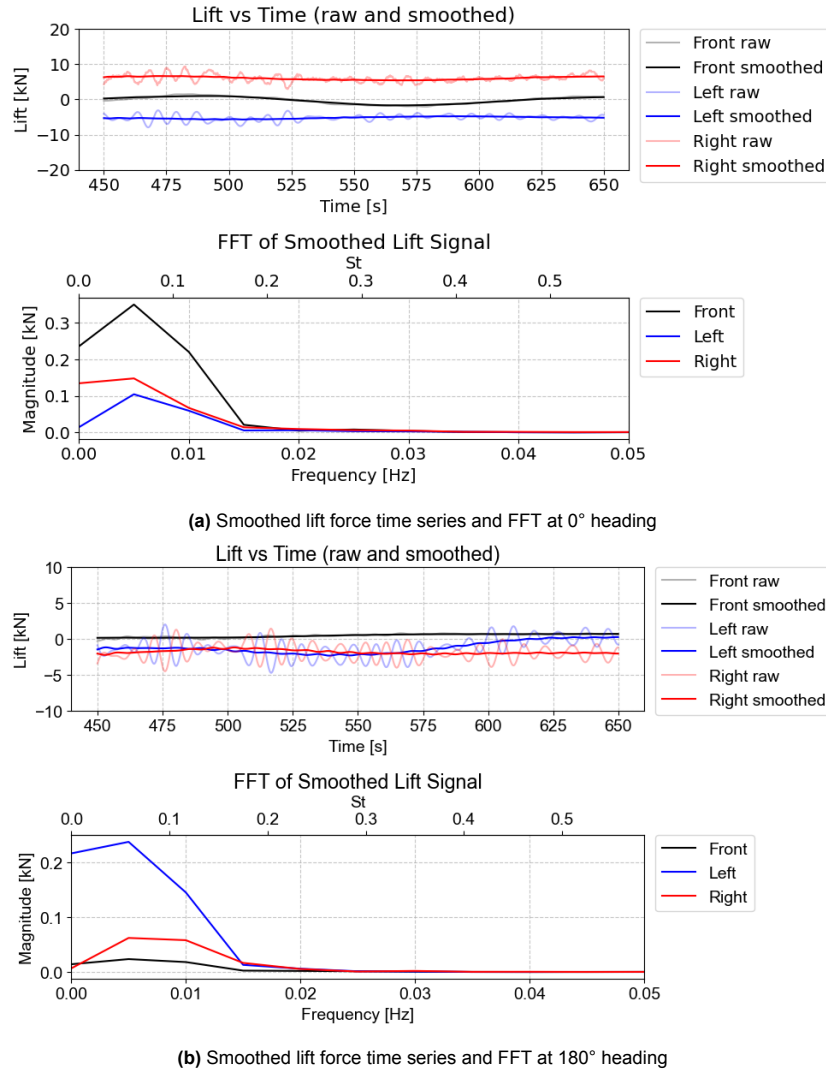
Figure 5.7: The smoothed lift forces of both 0° and 180° under flow speed of 2 knots after transient

In the earlier stage of the time series, the lift oscillation frequency in 0° heading due to the asymmetric wake is found to be around 0.006 Hz, corresponding to a Strouhal number of 0.07. While in 180° heading, the frequency is found to be 0.008, corresponding to a Strouhal number of 0.1. However, both cases eventually develop into a steady lift force as shown in Figure 5.7. The small fluctuations are likely attributed to slight irregular wake imbalance, as the vorticity fields shown in both Figure 5.8 and Figure 5.9 are steady. The left and right columns in 0° heading have a constant offset of lift force symmetric to zero in the end, while in 180°, the lift forces of all columns are close to zero.

Figure 5.3 shows the vorticity field at $t = 305$ s. Asymmetric vorticity is visible behind the side columns, indicating unsteady interactions in the wake. These flow features correspond to the low-frequency lift fluctuations observed in Figure 5.7a. However, the wake pattern does not persist as the simulation is extended, suggesting that it does not represent sustained vortex shedding but transient asymmetric wake structures. As the simulation continues, the unsteadiness diminishes. The vorticity field at $t = 650$ s in Figure 5.8a shows a symmetric and steady wake, and the corresponding lift forces also stabilize. This indicates that the early wake asymmetries are temporary and gradually suppressed. Numerical

damping from the solver and turbulence model could be possible sources causing the damping. This suggests that the simulation time may not have been long enough to capture the final wake state. Other cases showing unsteady behavior at earlier times might also develop into steady flow if the simulation is extended.

Figure 5.8 compares the vorticity fields of the 0° and 180° towing configurations at a horizontal plane 2 m above the base columns. In the 0° case, the wake is narrower and more concentrated along the centerline, indicating a better alignment with the free stream direction. The wake of the front column is smaller and more confined compared to the trailing columns. This suggests a channeling effect due to the front column deflecting flow into the region between the trailing columns. In contrast, the 180° configuration shows a broader and less interacting wake, with each column's wake developing independently. The wider wake and more uniform inflow in the 180° case lead to greater flow stability and reduced lift forces.

(a) Vorticity field at $z = -2$ m upper column and $t = 650$ s for 0° heading

(b) Vorticity field at $z = -2$ m upper column and $t = 600$ s for 180° heading
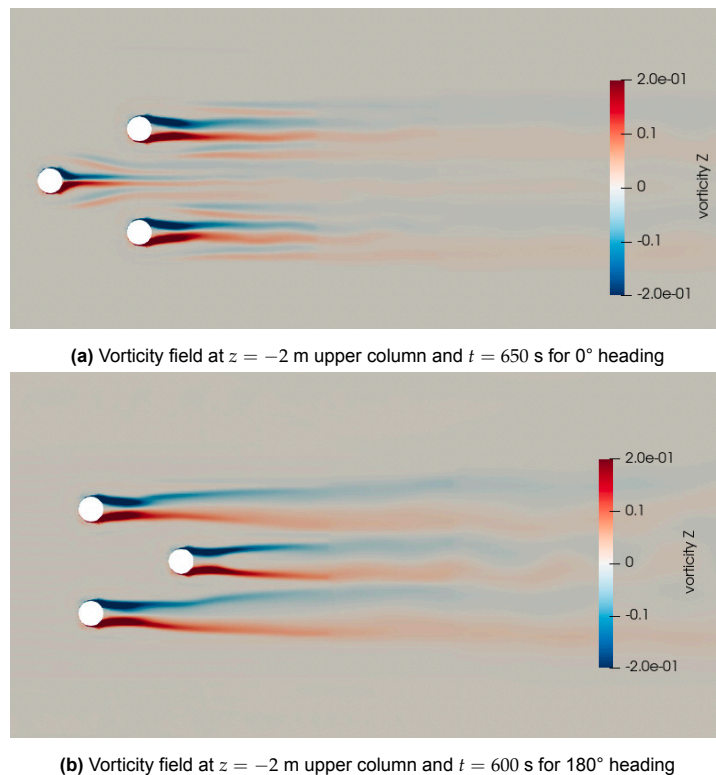
Figure 5.8: Both 0° and 180° turned steady, with 0° having a narrower waake and 180° having a more diverging and individually developed wake

At 10 m of draft, the base columns take up more than half of the draft, as their heights are 6 m. The vorticity fields at the mid-section of the base columns are also checked and shown in Figure 5.9. It can be seen that the vorticity fields are also steady at $t = 600$ s.

(a) Vorticity field at $z = -7$ m base column and $t = 600$ s for 0° heading

(b) Vorticity field at $z = -7$ m base column and $t = 600$ s for 180° heading
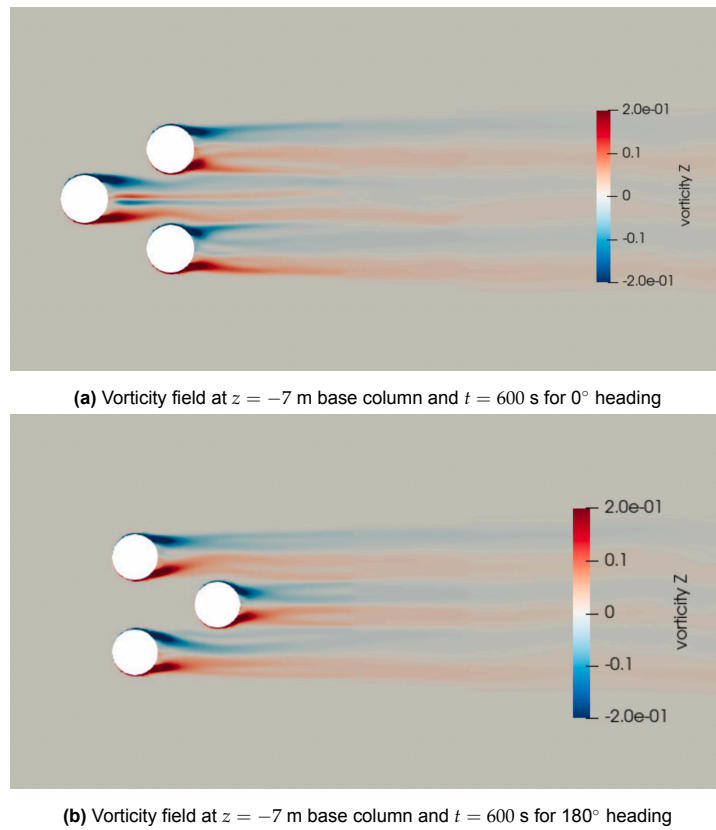
Figure 5.9: Both 0° and 180° turned steady and looks more similar compared to the upper columns

Both the base and upper columns of 0° and 180° cases exhibit a pair of vortices in their wake as shown in Figure 5.10. However, the vortex structures behind the base column are more helical due to the free end at the bottom, with limited lateral extent. This also stretches the vortices downstream behind the upper column. The vortex structures are highly three-dimensional, rather than forming a typical von Karman vortex street. As a result, no clear vortex shedding is observed. Furthermore, the pair of vortices behind the upper column in 0° heading is more organized and has a higher coherence compared to the 180° heading, which indicates a higher instability.

(a) Streamlines behind the right column in 0° heading

(b) Streamlines behind the right column in 180° heading
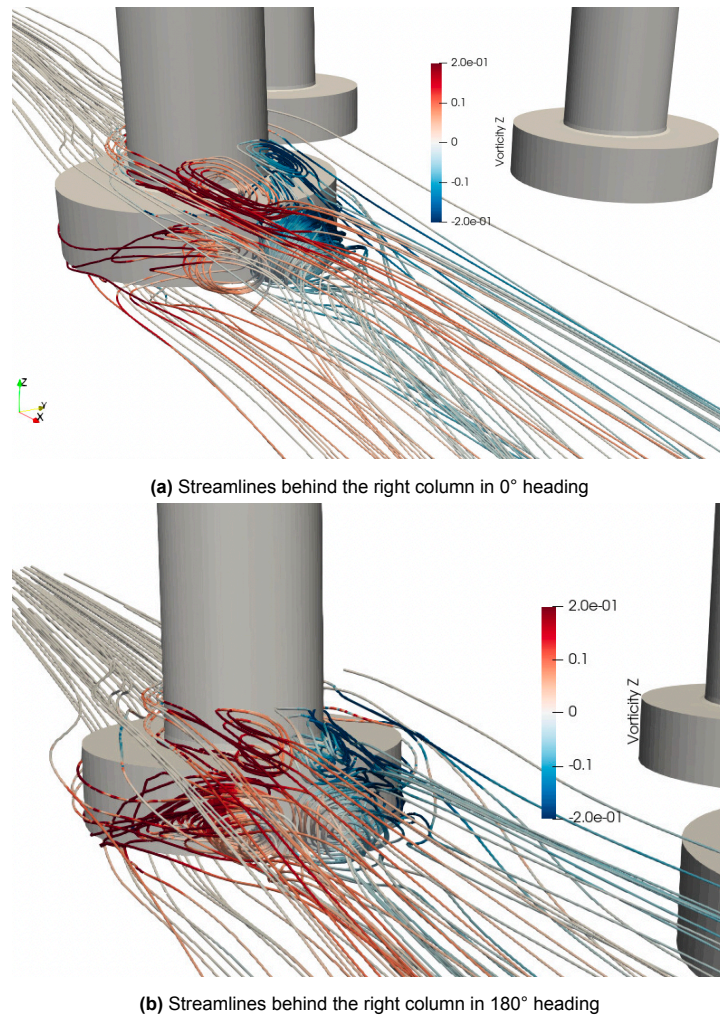
Figure 5.10: Both streamlines show highly three-dimensional flow, with 0° having slightly organized and higher coherence vortices behind the upper column.

Figure 5.11 shows the vorticity in the x-direction of both towing headings intersecting the left and right columns, with the flow directed out of the page. This figure clearly shows the three-dimensional flow and the helical vortices. Furthermore, the flow between left and right columns in 0° towing heading shows the influence of the wake of the front column.

(a) 0° towing configuration

(b) 180° towing configuration
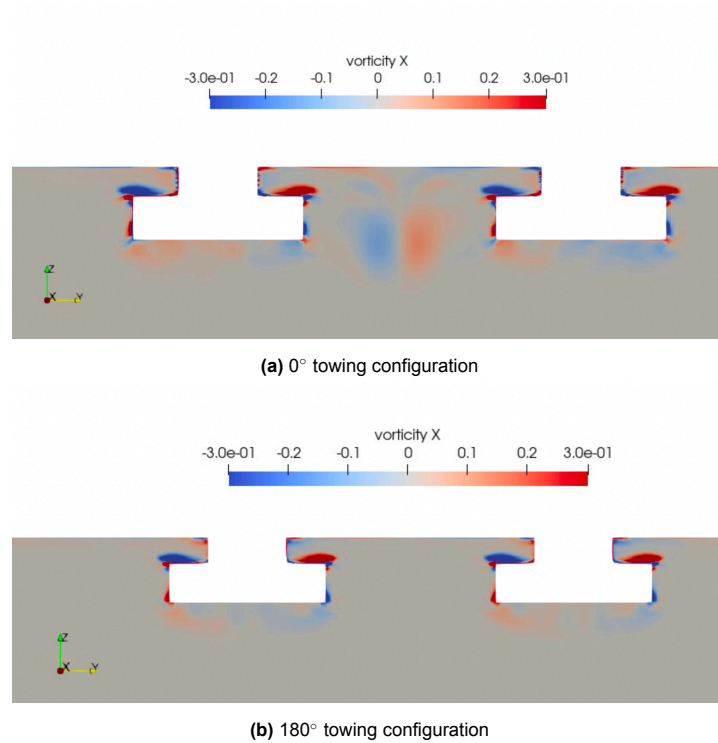
Figure 5.11: Streamwise vorticity (x-vorticity) field on the plane intersecting the left and right columns, illustrating three-dimensional flow structures under different towing headings. The flow direction is out of the page.

Figure 5.12 compares the overall streamline patterns between the 0° and 180° towing configurations. In the 0° case, the wake of the front column is deflected inward due to the presence of the two trailing columns and has a narrower wake. As a result, the velocity between the columns increases, creating a low-pressure region along the inner sides of the left and right columns. This asymmetry in pressure distribution leads to non-zero mean lift forces on the side columns, consistent with the lift forces shown in Figure 5.7a. In contrast, the flow between the columns remains relatively uniform, and the streamlines remain parallel throughout most of the domain in 180°. This leads to a more balanced force distribution and weaker lift response.

(a) Streamlines of the 0° towing configuration

(b) Streamlines of the 180° towing configuration
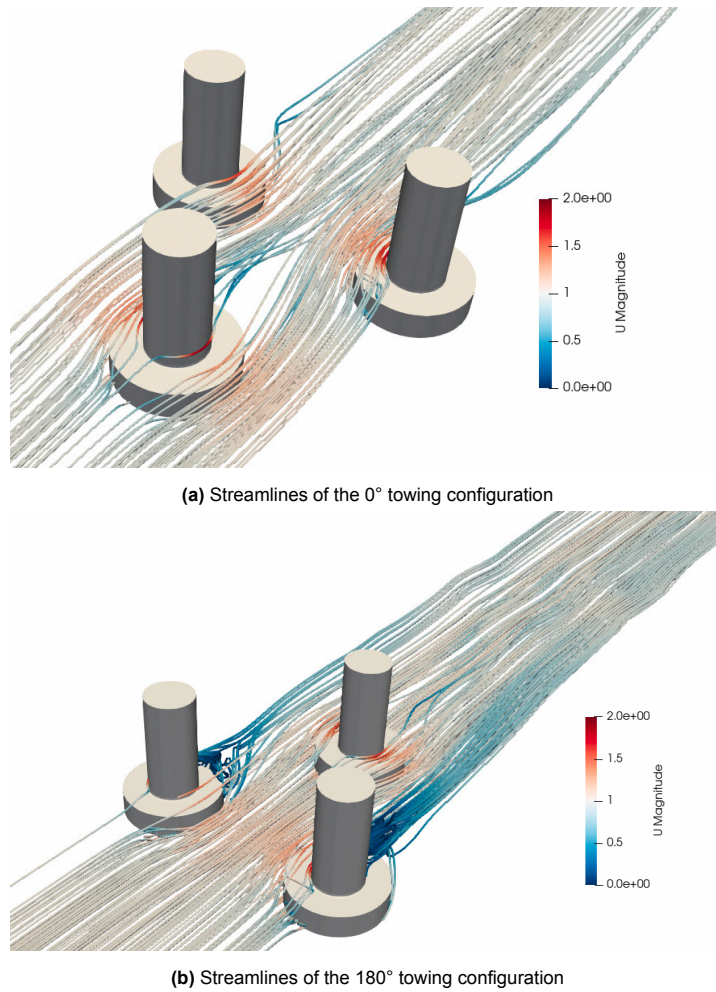
Figure 5.12: Streamlines of the wake in 0° are more deflected, while in 180° they are more parallel and uniform.

The mean drag force and RMS of lift force on each column in both configurations are shown in Table 5.2. The main difference in drag is found in the front column, where the drag in 180° is slightly lower than in 0°. This is due to the blockage effect of the left and right columns in the 180° heading. The lift forces on the left and right columns are generally higher in 0° heading, which is also seen in Figure 5.7a due to the non-zero mean.

	RMS lift [kN]		Mean drag [kN]		Drag coefficient	
	0°	180°	0°	180°	0°	180°
Front	1.18	1.6	44.7	41.8	0.43	0.40
Left	4.57	1.7	45.6	45.1	0.44	0.43
Right	4.8	2.2	45.7	45.1	0.44	0.43

Table 5.2: RMS of lift force and mean drag force on each column at towing speed of 2 knots

The drag coefficient at this Reynolds number from experiments found in Figure 2.2 is roughly 0.7, significantly higher than the ones shown in Table 5.2. However, this value is for flow over an infinite cylinder. In comparison, the aspect ratios (L/D) in these cases are lower than 1 and have significant

3D effects due to the free end at the bottom. The flow can escape from beneath, reducing the pressure difference. This is shown in section 5.4.

5.1.3. Comparison of different towing speeds

Simulations with the same settings for both towing headings are also done for towing speeds of 1 and 3 knots. However, the issue of reflections was only discovered late in the study. Due to time and resource limitations, they are not extended for longer than 350 seconds.

The time series and the FFT of the lift force on each column are shown in Figure 5.13 below. The first three rows show the forces individually, and the last row shows the sum of all three columns. Looking at the peaks at 0.08 Hz, 0.11 Hz, and 0.135 Hz, they exist in all three cases, independent of the towing speeds. Again indicates that this is due to reflections that depend on the water depth and the domain size. The amplitude increases with the velocity because of the larger velocity difference at the beginning of the simulation between the flow and the wall.
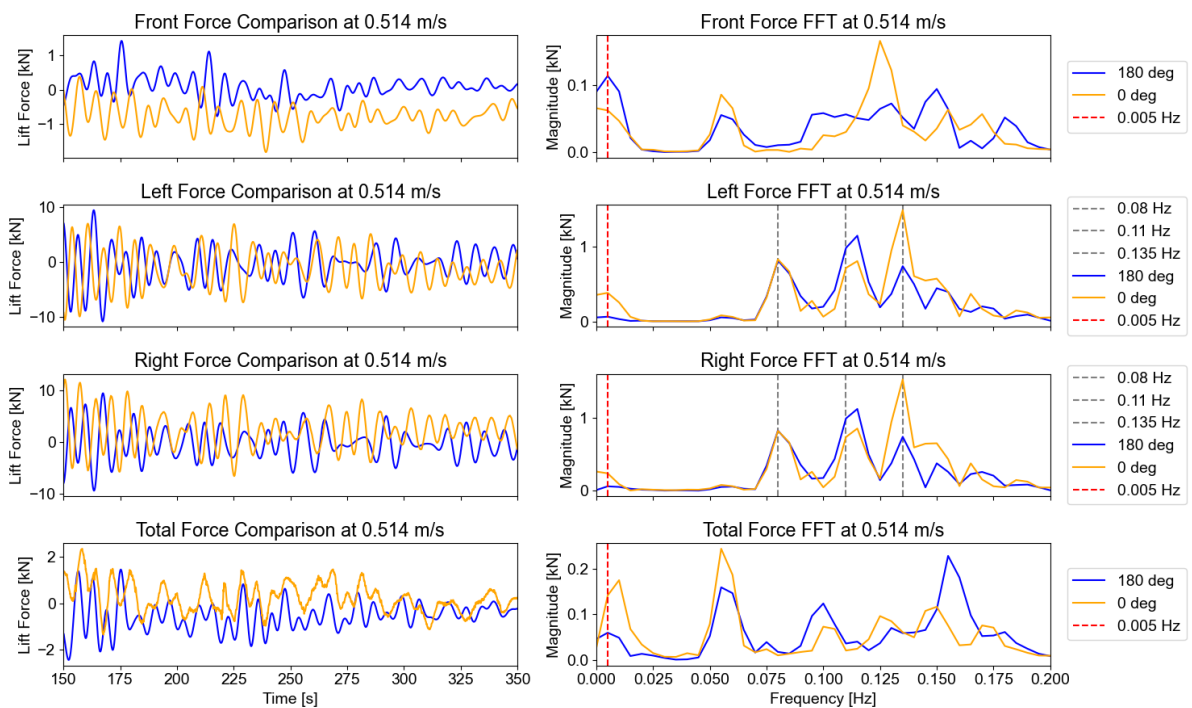
(a) Lift force and FFT on each column at 1 knot towing speed

Figure 5.13: Comparison of lift force and frequency spectra on each column where grey lines correspond to standing wave frequencies and red lines correspond to wake asymmetry (Part 1)
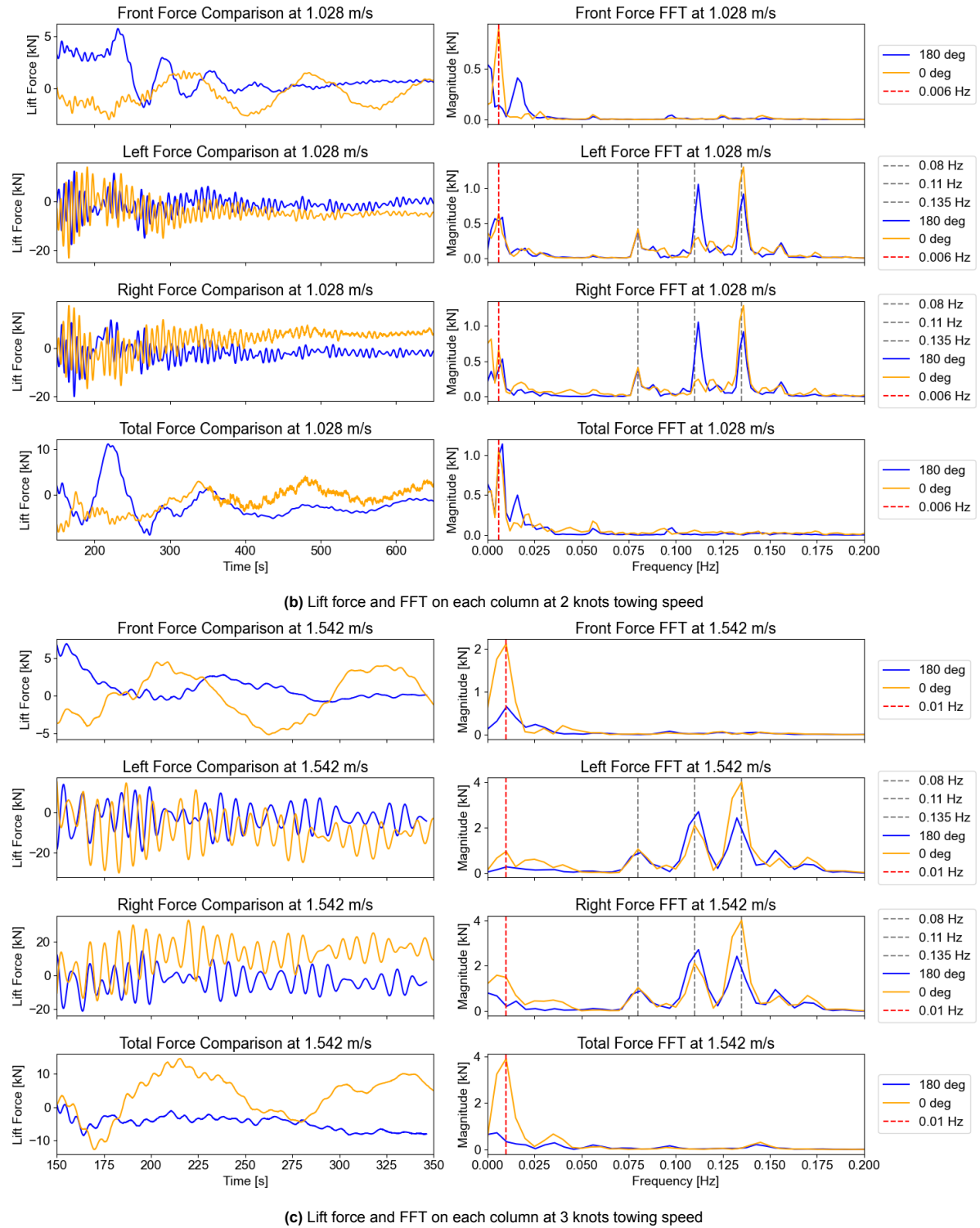
(b) Lift force and FFT on each column at 2 knots towing speed

(c) Lift force and FFT on each column at 3 knots towing speed

Figure 5.13: Comparison of lift force and frequency spectra on each column where grey lines correspond to standing wave frequencies and red lines correspond to wake asymmetry (Part 2)

The frequencies due to the asymmetry wake appear on the very low end of the frequency spectrum. The resolution is quite low due to the limited simulation length. However, it is still able to tell that the peak in 1 knot is roughly between the first and second data points, which is lower than 0.005 Hz. In 2

knots, the frequency can be seen more clearly at 0.006 Hz. In 3 knots, the frequency can be seen at roughly 0.01 Hz. This shows the dependency of the frequency on the towing speed. In all three speeds, the 0° heading configuration has a clearer peak compared to the 180° heading. As mentioned earlier, this is likely due to the non-uniform inflow and the higher instability in 0° heading.

Estimating the shedding frequency from a Strouhal number of 0.2, the shedding frequency of the upper columns in towing speeds of 1, 2, and 3 knots should be 0.008, 0.017 Hz, and 0.025 Hz, respectively. And for the base columns, the shedding frequencies should be 0.004 Hz, 0.008 Hz, and 0.013 Hz. However, the observed unsteady behavior is not attributed to classical vortex shedding, but rather to wake asymmetry. As a result, the dominant frequencies obtained from the lift signals are lower than those estimated based on the typical Strouhal number of 0.2. These lower frequencies reflect large-scale, transient instabilities in the wake rather than periodic shedding from individual columns. Additionally, they are expected to evolve into a steady flow due to the highly three-dimensional flow, and the experience from the 2 knots cases.

Figure 5.14 shows the drag force on each column of both headings over the towing speed. The drag forces on the left and right columns of the two towing configurations are similar, while the drag force on the front column is generally higher in 0° heading due to the absence of the blockage effect. As a result, the total drag force of the floater is slightly higher at 0° compared to 180°. This can also be seen in Table 5.3. The total drag force in 0° is generally slightly higher than 180°, although the difference is small. The drag coefficients are also very similar in different towing speeds, with the differences being roughly 5%.
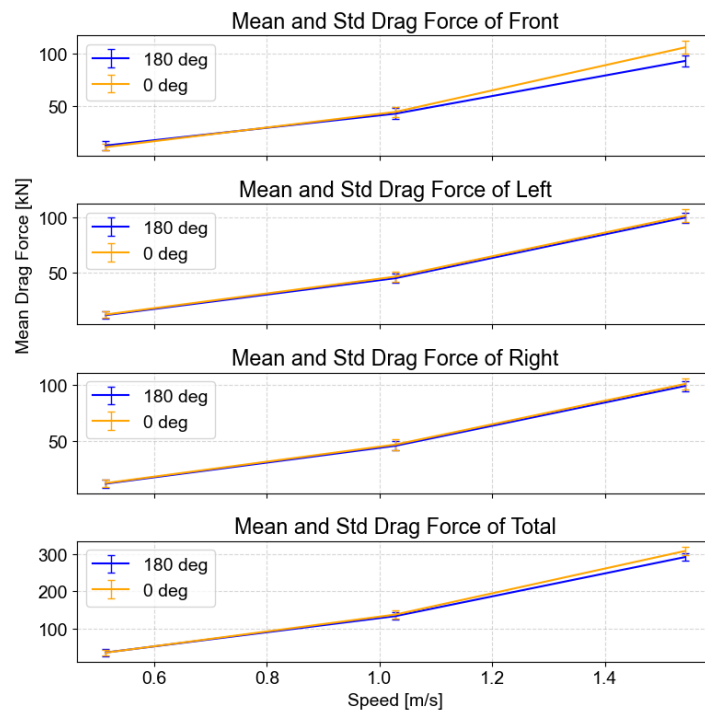
Figure 5.14: Drag forces of 0° and 180° heading on each column and the total at three different towing speeds.

	Mean drag [kN]		Drag coefficient	
	0°	180°	0°	180°
0.514 m/s	36.7	36.6	0.47	0.47
1.028 m/s	138.1	134.0	0.44	0.43
1.542 m/s	308.2	292.0	0.44	0.42

Table 5.3: Mean drag force and drag coefficients of the full floater at various towing speeds and headings

Figure 5.15 shows the total drag of two configurations, and the drag force estimated with a drag coefficient of 0.7 found from Figure 2.2, based on the relationship between drag coefficient and Reynolds number for flow over infinite cylinders from experiments. It can be seen that the end effect does affect significantly and lowers the drag force by 33%, 36%, and 37% for 1, 2, and 3 knots, respectively.
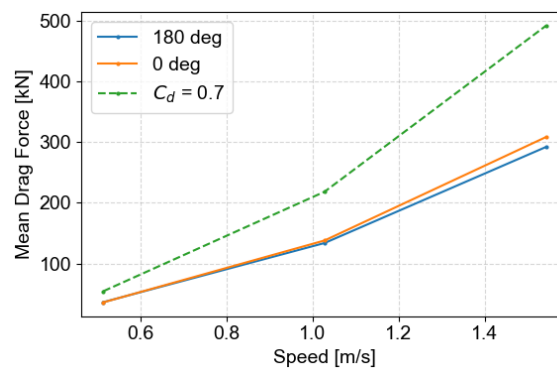
Figure 5.15: Total drag estimated from theoretical drag coefficient overestimates by more than 30%.

Overall, the flow in 180° has less wake instability. It is seen from Figure 5.7 that the 0° case takes more time for the wake to stabilize, and the left and right columns have non-zero mean lift force. This could possibly cause yaw motion in wet-towing configurations when the forces are not perfectly symmetric. Furthermore, the drag force in 0° is also slightly higher than 180°. Therefore, from the perspective of hydrodynamic forces alone, the 180° towing configuration may be considered more favorable.

5.2. Effect of free surface: double-body assumption versus multiphase

Figure 5.16 shows the drag force time series and FFT from both simulations. The first thing observed is that the time series from the double-body assumption does not have the high-frequency oscillations as in the multiphase simulation. This again indicates that the multiphase simulation results are contaminated by the reflections inside the domain. Furthermore, the drag forces obtained from the double-body assumption are higher than those of the multiphase simulation. This is not expected since the double-body assumption excludes the wave-making resistance. However, literature [6] shows that the inclusion of a free surface in flow over a cylinder can reduce the drag coefficient compared to single-phase flow. The reason is that the flow can better follow the surface of the cylinder with the inclusion of the free surface. Therefore, the transition of the shear layer is delayed in multiphase simulation, and the regular vortex shedding near the free surface is attenuated. This can also be

clearly seen in Figure 5.17 and Figure 5.18. The wake of the double-body assumption is much wider than that of the multiphase simulation. Additionally, the vortex shedding can be seen clearly in the double-body assumption, while the strength of the vortices in the multiphase simulation is lower and not fully detached.

(a) Double-body assumption (single-phase)

(b) Multiphase simulation
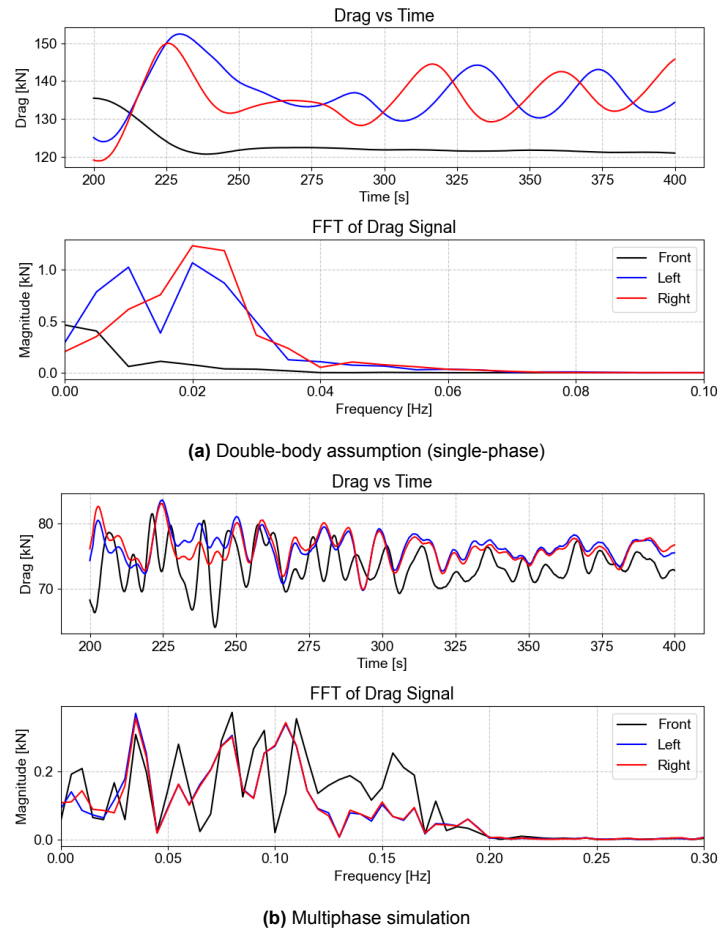
Figure 5.16: Drag forces in single-phase do not have high-frequency oscillations compared to the multiphase, indicating the effect of the reflection waves. Also, higher drag forces in single-phase.
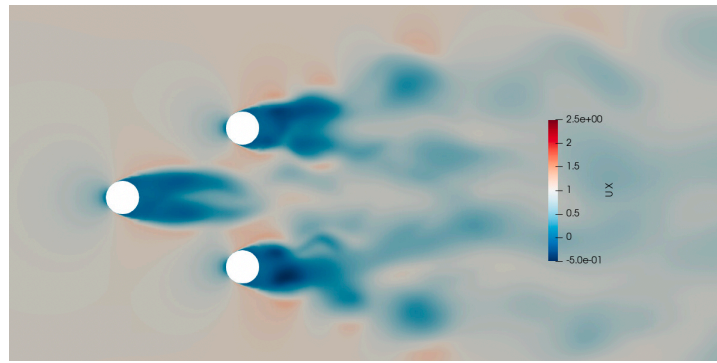
(a) U_x velocity field from double-body (single-phase) simulation at $z = -7$ m.

(b) U_x velocity field from multiphase simulation at $z = -7$ m.

Figure 5.17: U_x velocity field in single-phase shows earlier separation and wider wake resulting in the higher drag.
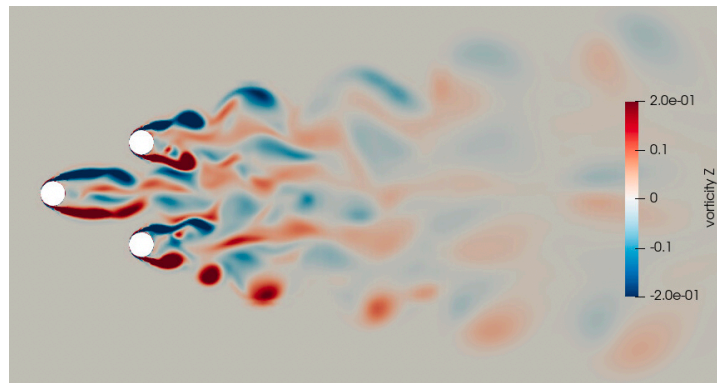
(a) Vorticity field from double-body (single-phase) simulation at $z = -7$ m.
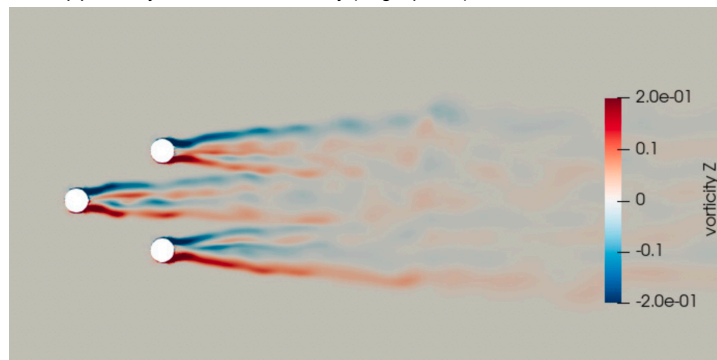
(b) Vorticity field from multiphase simulation at $z = -7$ m.

Figure 5.18: Vorticity field in single-phase shows clear vortex shedding with a period of roughly 50 s, which is not seen in the multiphase simulation.

Table 5.4 shows the mean drag and drag coefficient of the individual columns and the full floater. The drag force obtained from the double-body assumption simulation is found to be 75% higher than the multiphase simulation.

	Mean drag [kN]		Drag coefficient	
	Double-body assumption	Multiphase	Double-body assumption	Multiphase
Front	122.8	73.5	0.72	0.43
Left	136.9	76.3	0.81	0.45
Right	135.5	76.2	0.80	0.45
Total	395.2	226	0.78	0.45

Table 5.4: Mean drag force and drag coefficient comparison of double-body assumption and multiphase simulation
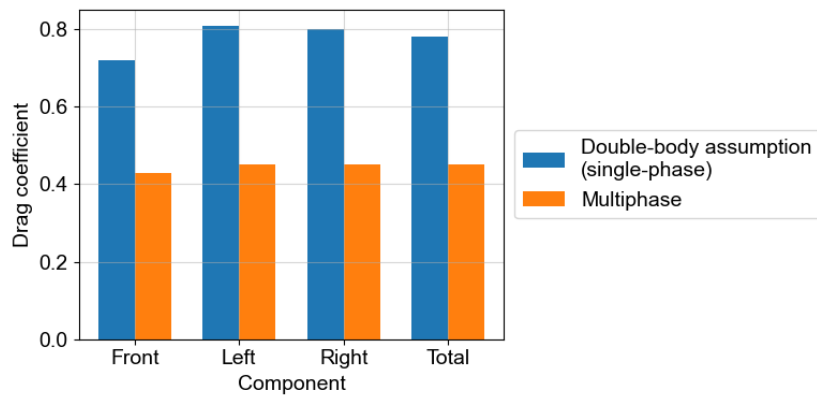
Figure 5.19: Drag forces are overestimated by 75% in single-phase simulation

Figure 5.20 shows the lift force and the FFT on each column. The lift forces on the left and right columns in the single-phase simulation are roughly $180°$ out of phase, with a slight phase shift. The frequency found in the double-body assumption matches the visualized frequency of vortex shedding found in the shot of the vorticity field in Figure 5.18a. The dominant frequency is roughly 0.02 Hz, which is 50 seconds, and corresponds to a Strouhal number of 0.23, which is also close to a theoretical value of 0.2. The lift forces of the multiphase simulation are affected by the reflections and therefore are smoothed with a rolling window of 50 s. The surface elevation shown in Figure 5.21 points out that the main reflections have a period of roughly 8 s. Even though the wave height of the reflections is only approximately 4 cm, the results are still highly influenced. The lift forces in the multiphase simulation do not have regular oscillating forces but some irregular fluctuations due to the imbalance in the complex wake. The essential point to convey is that regular oscillation is found in the single-phase simulation due to vortex shedding, while it is not observed in the multiphase simulation.

(a) Double-body (single-phase)

(b) Multiphase simulation
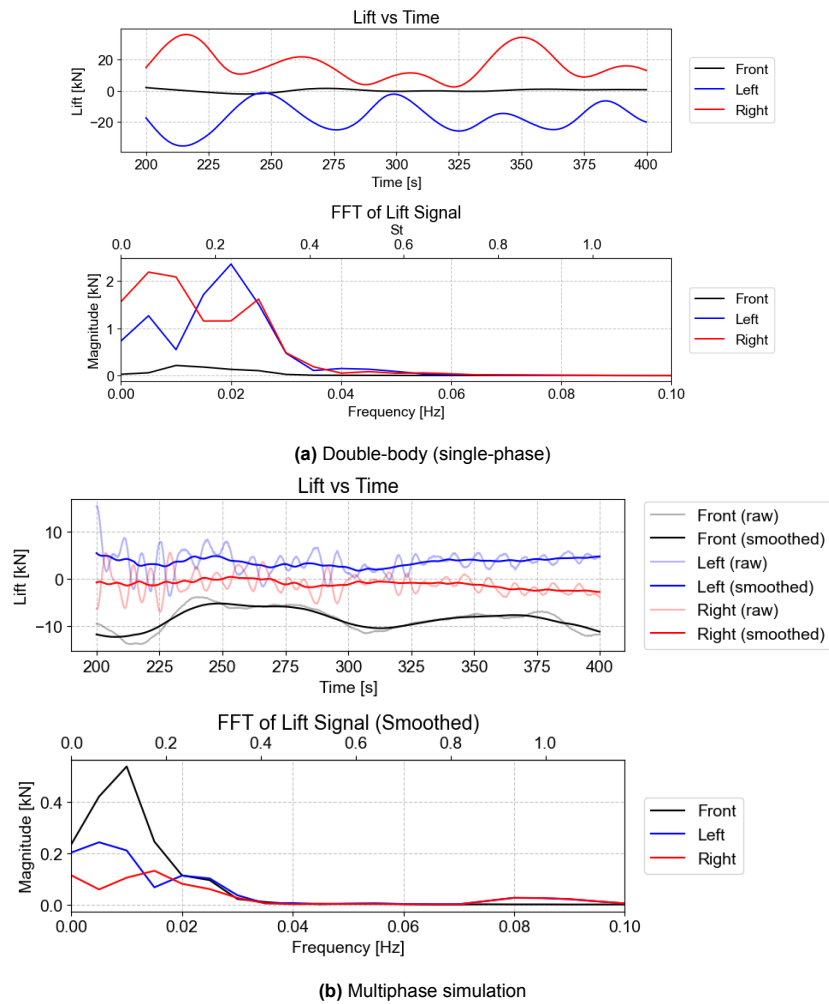
Figure 5.20: Lift forces in single-phase simulation show oscillation with a period of roughly 50 s due to vortex shedding, while comparing the magnitude, relatively steady in multiphase simulation

(a) Free surface elevation at $t = 364$ s

(b) Free surface elevation at $t = 372$ s
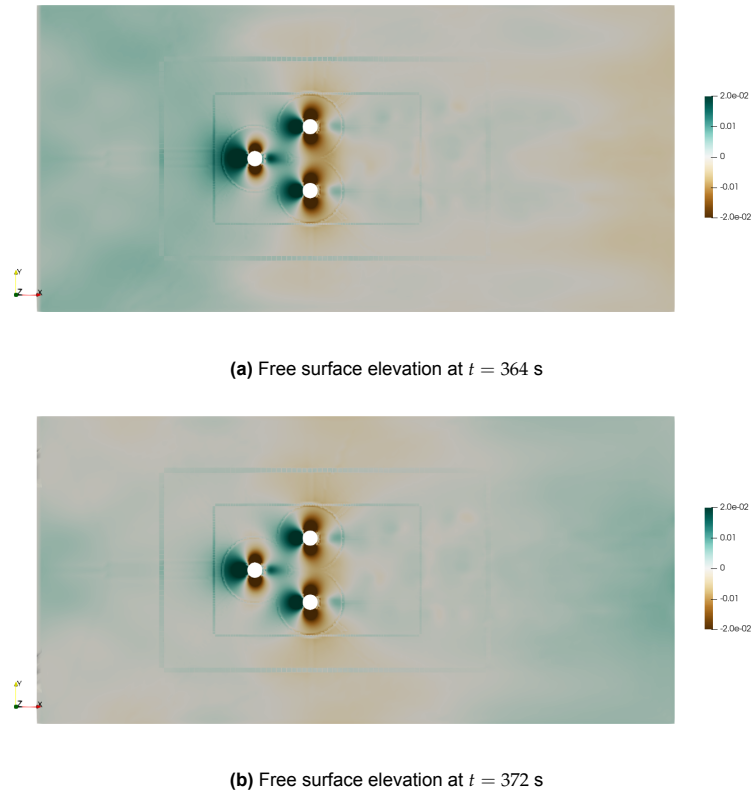
Figure 5.21: Numerical reflections with a period of roughly 8 s in the multiphase simulation

The combined force of all three columns from the single-phase simulation is shown in Figure 5.22. It is seen that the oscillation can still be seen in the combined force as they are not canceled out. The amplitude of the lift forces are within 20 kN. Comparing the lift force oscillation period of 50 s to the natural period of sway motion of the towing system obtained in section 3.7, which is at least 800 s in the extreme case, the lift force oscillation is unlikely to cause resonance.
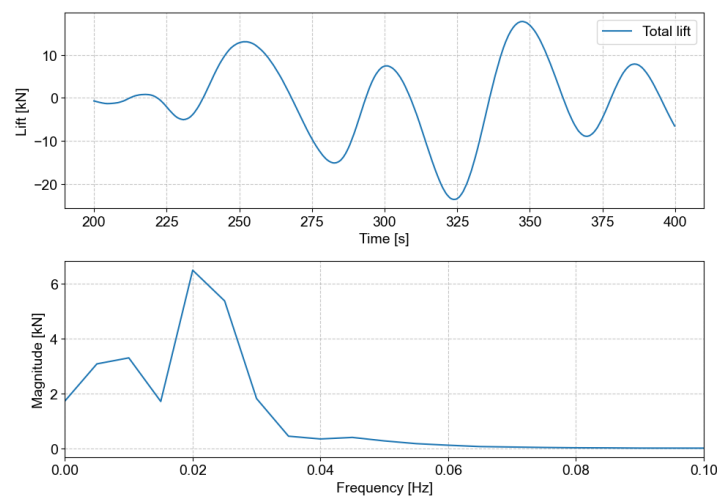
Figure 5.22: Lift force and FFT of the full floater from the single-phase simulation

The streamlines behind the right column in the multiphase simulation and the double-body assumption simulation are shown in Figure 5.23 and Figure 5.24. In the double-body assumption simulation, a symmetry boundary condition is applied at the top of the domain. This restriction forces the flow to remain planar along the upper column and suppresses the development of three-dimensional effects near the free surface. As shown in Figure 5.24, this results in the formation of stronger and more coherent vortex structures behind the column. The vortices are clearly detached from the column surface, and the regular frequency due to vortex shedding is clear. In contrast, the free surface in the multiphase simulation introduces additional 3D effects that disrupt vortex coherence.
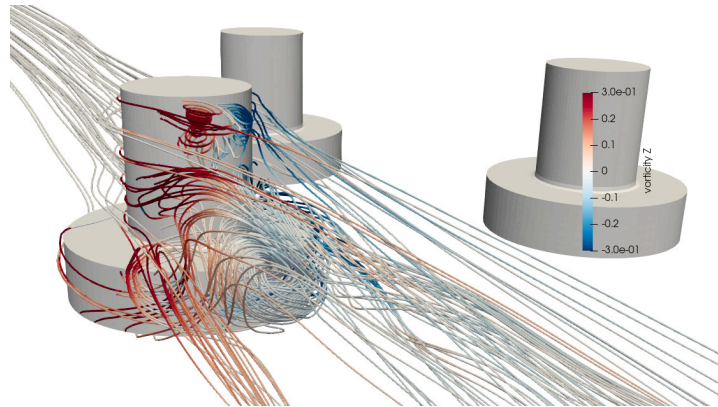
Figure 5.23: Streamlines behind the right column in the multiphase indicate a highly three-dimensional flow and nearly no coherence in the vortices.

(a) Side view of the vortex structure behind the right column

(b) Top view of the vortex structure behind the right column
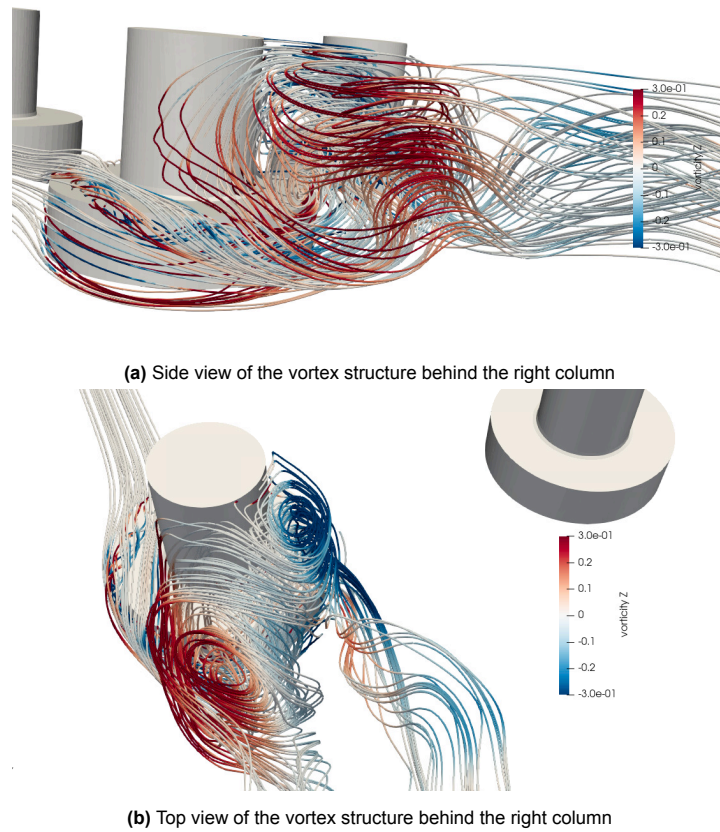
Figure 5.24: Streamlines in single-phase simulation indicate that flow is constrained to horizontal planar near surface and forces high coherence, hence vortex shedding occurs.

This section shows that the simulation with the double-body assumption dramatically overestimates the drag force by 75% compared to the multiphase simulation, indicating this simulation does not serve the purpose of accurately predicting drag force well. However, the vortex shedding is very clear and the period is found to be roughly 50 s, which matches the theoretical Strouhal number well. This simulation serves the purpose of finding the potential vortex shedding frequency well. Yet, the comparison shows that the effect of free surface on vortex shedding is significant, and is questionable if it can represent the case in real life.

5.3. Scaling effect: Model-scale versus Full-scale

The forces and time scale of the model-scale simulation are scaled to full scale following section 2.7 using the Froude's method. The comparisons below are done at equivalent full-scale for easier comparison.

Figure 5.25 shows the velocity field (U_x) of both model scale and full scale. They are both plotted over a range of 1.5 times higher and lower than the inflow velocity. The model scale's separation point is found to be more upstream than the full scale. This is expected due to the difference in Reynolds number. In higher Reynolds numbers, the flow is more turbulent and can better follow the surface of the column, delaying the separation. Therefore, the wake of the model scale is much wider than the full scale.

(a) Model-scale velocity field (U_x) at $z = -7$ m and $t = 400$ s. Re = 3.4×10^4

(b) Full-scale velocity field (U_x) at $z = -7$ m and $t = 400$ s. Re = 1.23×10^7
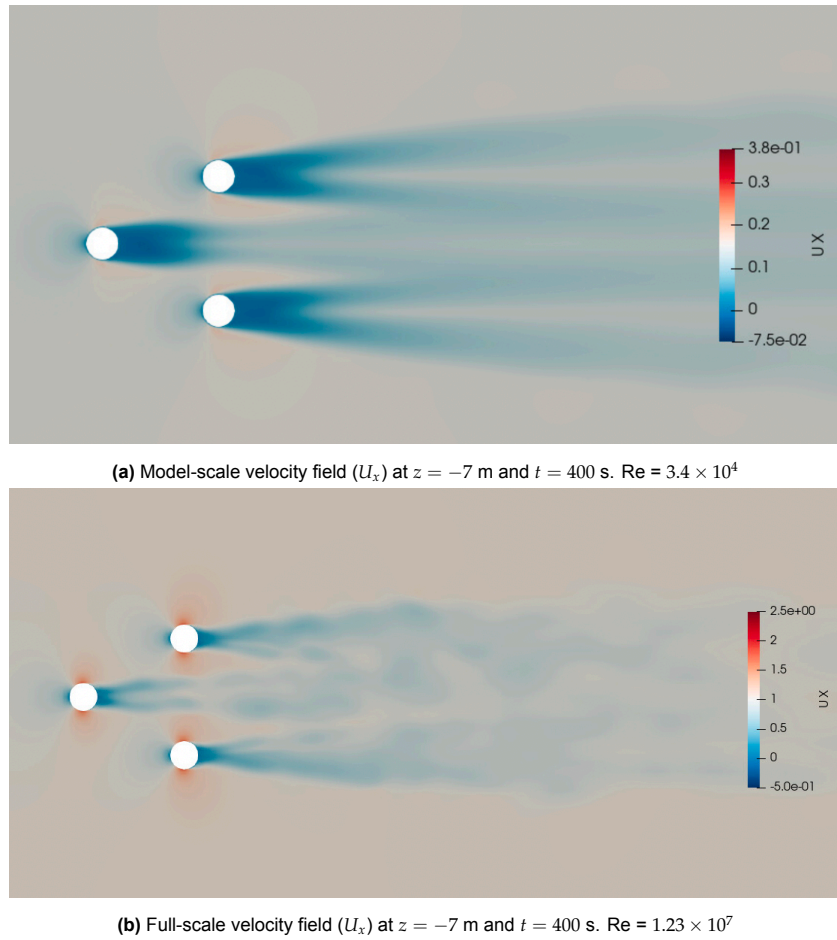
Figure 5.25: U_x in model-scale shows earlier separation and wider wake due to the difference in Reynolds numbers.

Figure 5.26 shows the mean drag forces on each column of both simulations. In both cases, the drag force on the left and right columns are almost identical, and the front column has a slightly lower drag force. This is interesting as the front column is leading in this configuration. It can be explained more clearly through the pressure field of the model-scale shown in Figure 5.27. The front column is affected by the high pressure in front of the two trailing columns, so the pressure difference between upstream and downstream of the front column is lower, resulting in a slightly lower drag force. It is found to be more obvious in model scale than in full scale.
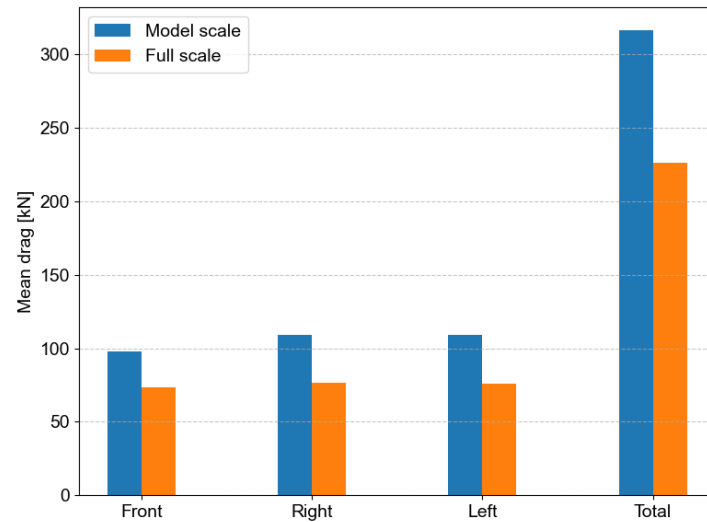
Figure 5.26: Mean drag force at towing speed of 2 knots, 20 m draft predicted from model scale simulation and full scale simulaiton
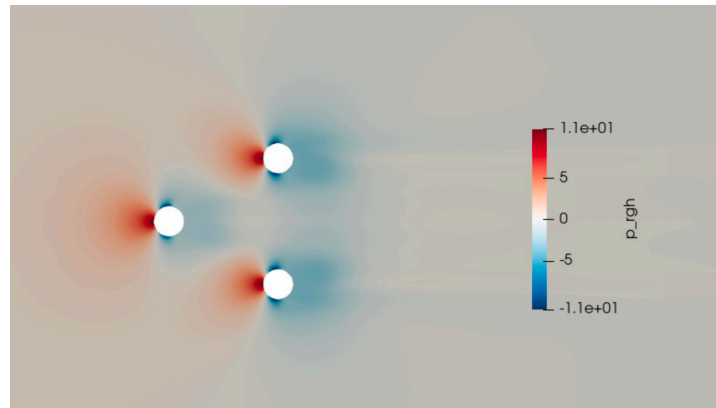
Figure 5.27: Pressure field of the model scale simulation at $z = -7$ m and $t = 400$ s shows that the lower drag force on the front column is due to the high pressure upstream of the trailing columns.

The mean drag force and the drag coefficients of the individual columns and the total floater are shown in Table 5.5. The total drag force of the model scale is found to be nearly 40% higher than the full-scale model, part of it can be attributed to the form drag, which is a kind of pressure drag, that is not separated from the residual resistance and is being directly Froude scaled. This shows that the cylinders have quite high form drag, so it is very conservative not to separate the form drag and wave-making resistance. The calculated form drag $(1 + k)$ to match the drag of full-scale from model-scale is 14.3, which is very high due to the bluff body. The theoretical drag coefficients for infinite cylinders found in Figure 2.2 for model-scale and full-scale Reynolds numbers are roughly 1 and 0.7, respectively. Considering the end effect demonstrated in section 5.4, these drag coefficients are reasonable.

	Mean drag [kN]		Drag coefficient	
	Model-scale	Full-scale	Model-scale	Full-scale
Front	97.8	73.5	0.57	0.43
Left	109.1	76.3	0.64	0.45
Right	109.2	76.2	0.64	0.45
Total	316.1	226	0.62	0.45

Table 5.5: Mean drag force and drag coefficient comparison of model-scale and full-scale
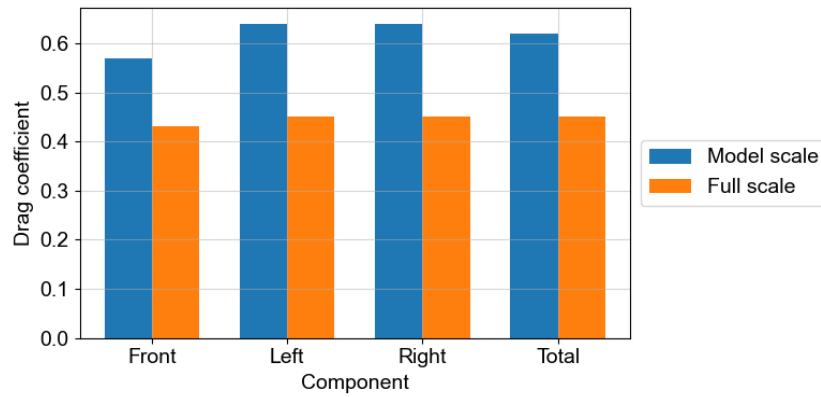
Figure 5.28: Drag forces are overestimated by approximately 40% in model-scale simulation.

Figure 5.29 shows the vorticity field at the mid-section of the upper column, which is $z = -7$ m and at $t = 400$ s. As expected, the vorticity field looks quite different. The vorticity field of the model-scale simulation is much smoother than the full scale. This is a result of the difference in Reynolds number. Furthermore, the vorticity field in the full-scale case is more irregular due to the convective vertical flow behind the columns.

(a) Model-scale vorticity field at $z = -7$ m and $t = 400$ s. Re = 3.4×10^4

(b) Full-scale vorticity field at $z = -7$ m and $t = 400$ s. Re = 1.23×10^7
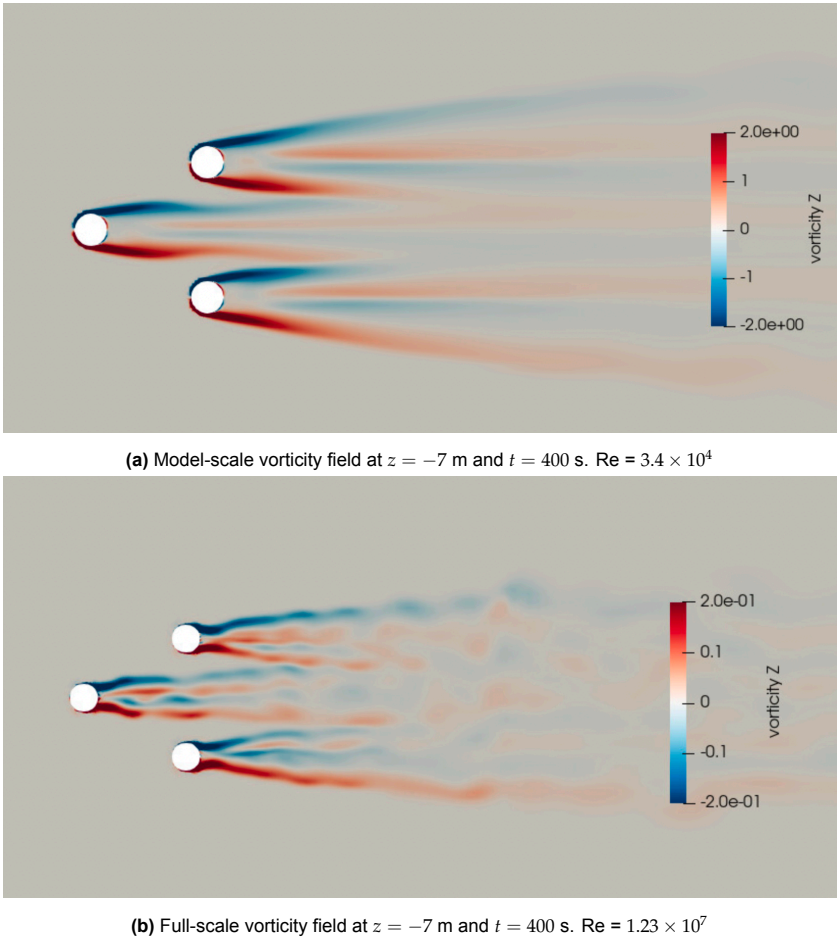
Figure 5.29: Vorticity field looks smoother in model-scale due to the difference in Reynolds numbers.

Figure 5.30 shows the mean lift forces on each column of both model scale and full scale. As mentioned in section 5.2, the lift forces of the multiphase simulations are diturbed by the numerical reflections. The total lift forces are expected to be close to zero since the floater is symmetric. However, they are not, which indicates that the simulation may still be in the transient phase. Nevertheless, it is shown here to convey that the forces are relatively small, and is relatively less relevant to the main focus of the study.
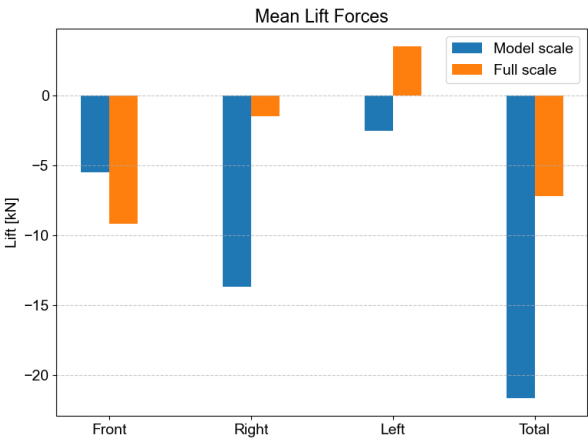
Figure 5.30: Mean lift forces after initial transient.

Figure 5.31 shows the streamlines behind the right column in model-scale and full-scale simulations. In the model-scale simulation, the influence of the free end is more pronounced. The circulation persists all the way to the water surface showing only a pair of vortices, and the backflow behind the column is obvious. In contrast, the full-scale case shows two distinct vortex pairs, one circulating from the base column and the other behind the upper column. These differences show that studying vortices in model scale might not be representative of what is happening in full scale. Nevertheless, in both cases, the free-end effect significantly suppresses the development of organized vortex shedding. As a result, the lift force becomes steady over time, and no clear periodic shedding pattern is observed.

(a) Streamlines behind the right column in model scale

(b) Streamlines behind the right column in full scale
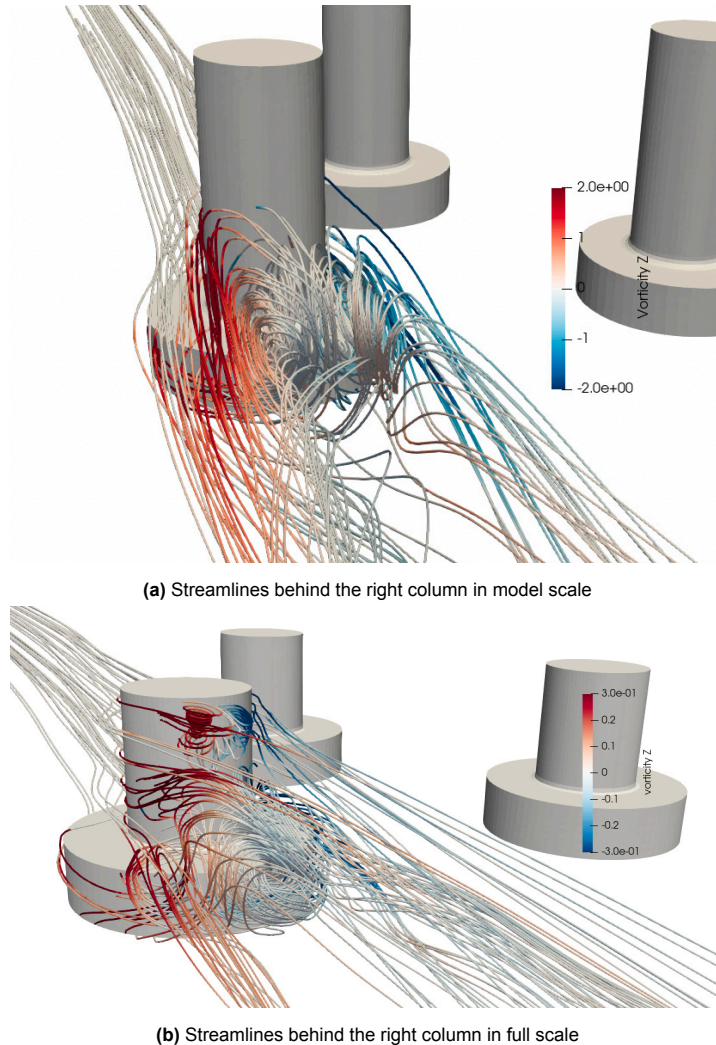
Figure 5.31: Streamlines in model scale show only a pair of vortices, while two are found in the full scale. However, both are highly three-dimensional and show little to no coherence.

This section shows that the model-scale multiphase simulation overpredicts the drag force by roughly 40% due to the earlier separation point. The drag force from model-scale can be scaled more accurately, but this requires the form drag coefficient to separate the viscous pressure drag and the wave-making resistance. The streamlines of model scale and full scale show quite different behavior. Therefore, studying vortex shedding in model scale might not be representative of real applications. Nevertheless, the vortices in these cases are strongly affected by the free end effect and are very three-dimensional. As a consequence, they do not have vertical coherence to form a typical von Karman street.

Drag prediction

One of the research questions was to compare the efficiency and accuracy of drag prediction from different models. To do so, three models are compared: the full-scale multiphase model, the full-scale single-phase model, and the model-scale multiphase model. The drag coefficient reading off the explicit relation between drag coefficient and Reynolds number for flow over cylinders is compared as well. Figure 5.32 shows the drag coefficients obtained from these three CFD models and from the explicit relation.
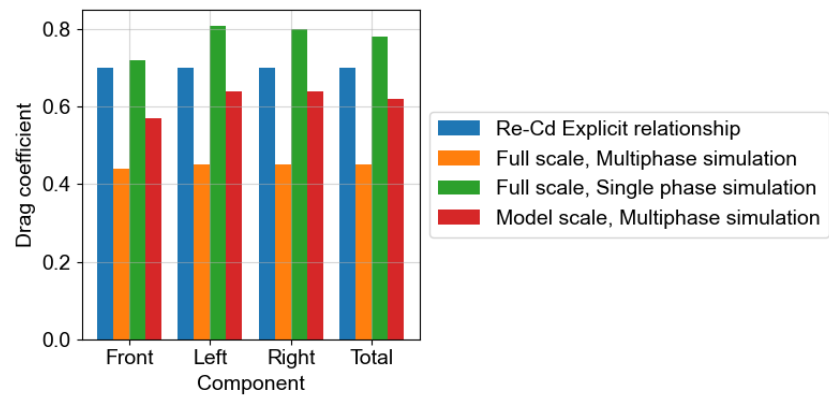
Figure 5.32: Drag coefficients obtained from various methods

To compare the difference in drag values, Figure 5.33 shows the predicted mean drag force from different models at a towing speed of 1.028 m/s, with 20 m draft.
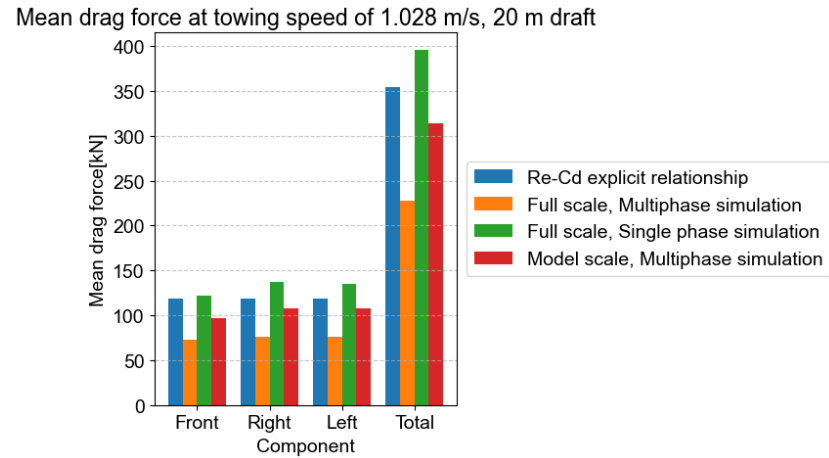
Figure 5.33: Mean drag force obtained from various models at towing speed of 1.028 m/s and 20 m draft

For comparing the computational cost and the efficiency of the three models. Table 5.6 shows the computational time for each model to simulate 350 s of time series.

	Full scale multiphase	Full scale single phase	Model scale multiphase
Mesh count	2.9 million	2.4 million	2.1 million
Computational time for 350 s simulatoin [core hours]	960	432	192
Error of drag prediction	-	75%	40%

Table 5.6: Comparison of computational cost and accuracy of drag prediction

- Full-scale multiphase model: This model is expected to be the most representative of the real-life case. The drag coefficient predicted from this model is 0.45, and is validated with literature. But it is also the most computationally heavy model, as it takes 960 core hours to simulate 350 s.

- Full-scale single-phase model: This model predicts a drag coefficient of 0.77, which is even less accurate than the explicit relation. This is because of the symmetry plane boundary condition that adds an extra constraint, which is not physically correct, to the flow. Even though the computational cost is less than half of the full-scale multiphase model, it is not suitable for the purpose of drag prediction.

- Model-scale multiphase simulation: This model predicts a drag coefficient of 0.63, which is 40 % higher than the full-scale multiphase model. However, the computational cost is only one-fifth of the full-scale multiphase model. For this reason, it is the most suitable model for drag prediction in terms of a balance between accuracy and efficiency. Furthermore, this model can be more accurately scaled with Hughes' method instead of Froude's method.

As a conclusion, if only focusing on the mean drag force, model-scale multiphase simulations can be used, and scaling with Froude's method can provide an upper bound of the prediction. Hughes' method can be used to improve accuracy.

5.4. Effect of free end: Infinite length cylinder versus Finite length cylinder

To investigate the influence of 3D effect on vortex shedding, two simple cases in single-phase are carried out. These two cases are described below:

1. Simulation with a single cylinder from the top to the bottom of the domain, simulating flow over an infinite length cylinder. This case should provide results closest to the theoretical values of drag coefficient and shedding frequency, since it is nearly equivalent to 2D simulations.

2. Simulation with a single cylinder in a deeper domain to allow flow from beneath, including the 3D effect, e.g., end effect.

The cylinders in both simulations are identical, with a diameter of 0.24 m and a length of 0.28 m, which is 12 m and 14 m in full-scale, respectively. This corresponds to the dimension of the upper offset column of the OC4 floater in its installed position. Figure 5.34 illustrates the side view of the two cases.

(a) Infinite cylinder

(b) Finite cylinder
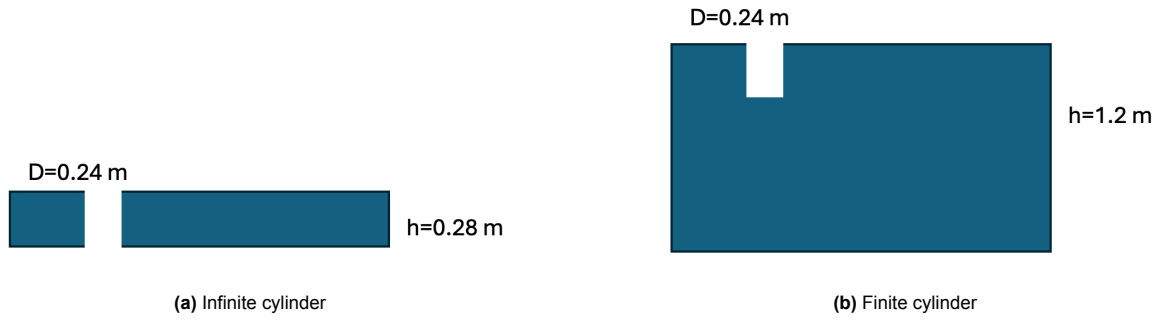
Figure 5.34: Illustrations of the two cases

Both cases have a velocity inlet of 0.085 m/s, and the Reynolds number can be calculated as follows:

$$\mathrm{Re} = \frac{UL}{\nu} = \frac{0.085 \cdot 0.24}{10^{-6}} = 20,400 \tag{5.2}$$

From Figure 1.6, the Strouhal number at this Reynolds number is found to be around 0.2. The shedding frequency can then be estimated from this Strouhal number as shown in Equation 5.3, which is 0.0708 Hz in frequency or 14.1 s in period.

$$f = \frac{\mathrm{St} \cdot U}{L} = \frac{0.2 \cdot 0.085}{0.24} = 0.0708 \text{ Hz} \tag{5.3}$$

The meshing procedure, boundary conditions, and solver settings all follow the single-phase simulation settings shown in chapter 3.

Figure 5.35 shows the time series of the drag coefficient of both the finite length cylinder and the infinite length cylinder. The mean drag coefficient of the infinite length cylinder is around 1.06, while the finite length cylinder is around 0.69, which is 35% lower. The drag coefficient of the infinite cylinder has an oscillation period of roughly 6.5 seconds, while the drag coefficient of the finite cylinder remains steady.
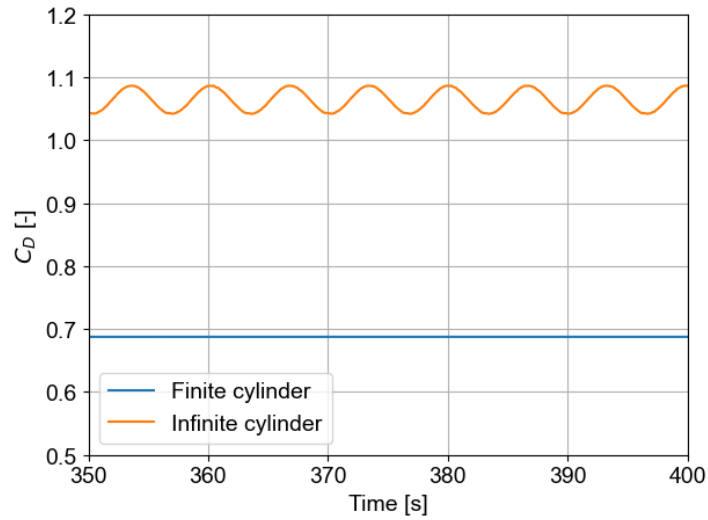
Figure 5.35: Time series of drag coefficient of infinite length cylinder and finite length cylinder

Figure 5.36 [28] demonstrates the relationship between the drag coefficient and the aspect ratio of the cylinder, where the red dot close to 0 in aspect ratio is the mean drag coefficient of the infinite case, and the dot at 0.86 is the finite case. This indicates that the results obtained are in agreement with the literature.
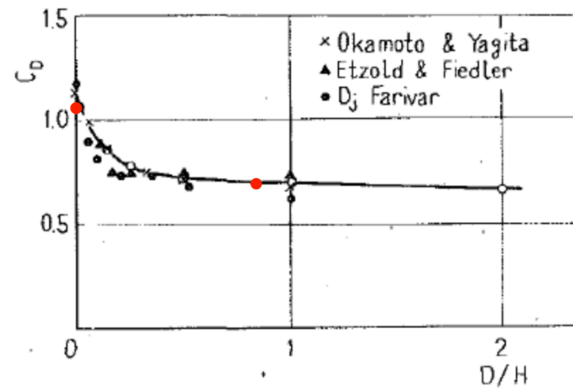
Figure 5.36: Relationship between drag coefficient and the aspect ratio of cylinder [28], where the two red dots represent the cases in the present study.

The drag difference between finite and infinite cylinder can be explained with the pressure distribution shown in Figure 5.37. The free end allows the flow to escape and accelerate from beneath. This causes the low pressure to appear also at the bottom of the cylinder. Therefore, the pressure difference between upstream and downstream is lower in the finite case, leading to a lower drag.

(a) Finite cylinder pressure distribution

(b) Infinite cylinder pressure distribution
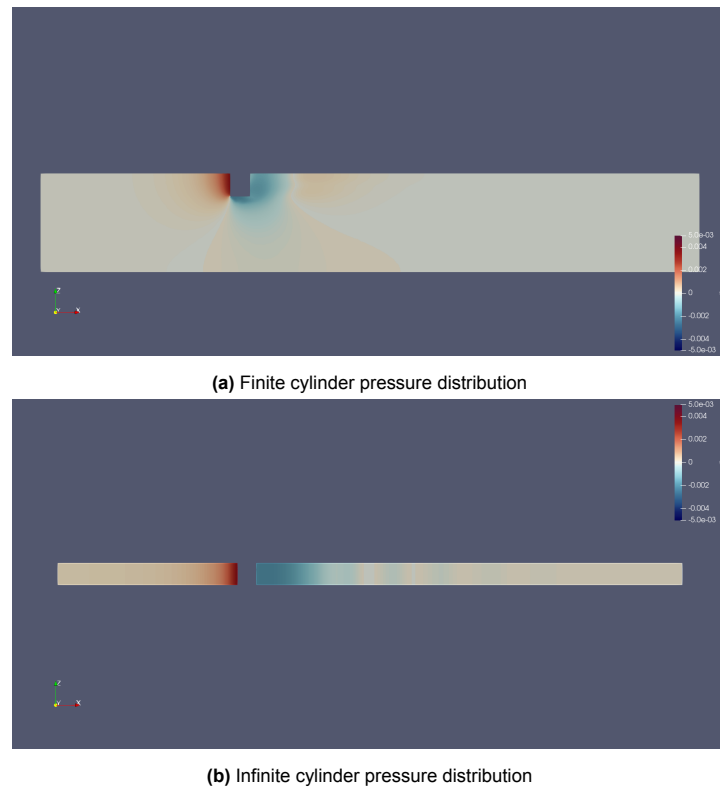
Figure 5.37: Pressure distribution indicates that the flow being able to escape from beneath reduces the pressure difference between upstream and downstream and thus the drag force.

Looking at the lift coefficients plotted in Figure 5.38, the finite length has no oscillation while infinite length has an oscillation with a mean lift coefficient around zero. By doing Fast-Fourier Transform, the frequency is found to be 0.0743 Hz, which is 13.46 seconds. This oscillation is due to vortex shedding, and it is not observed in the finite cylinder case. The Strouhal number can then be calculated from the shedding period as shown in Equation 5.4. This also matches the theoretical value of 0.2 found in Figure 1.6.
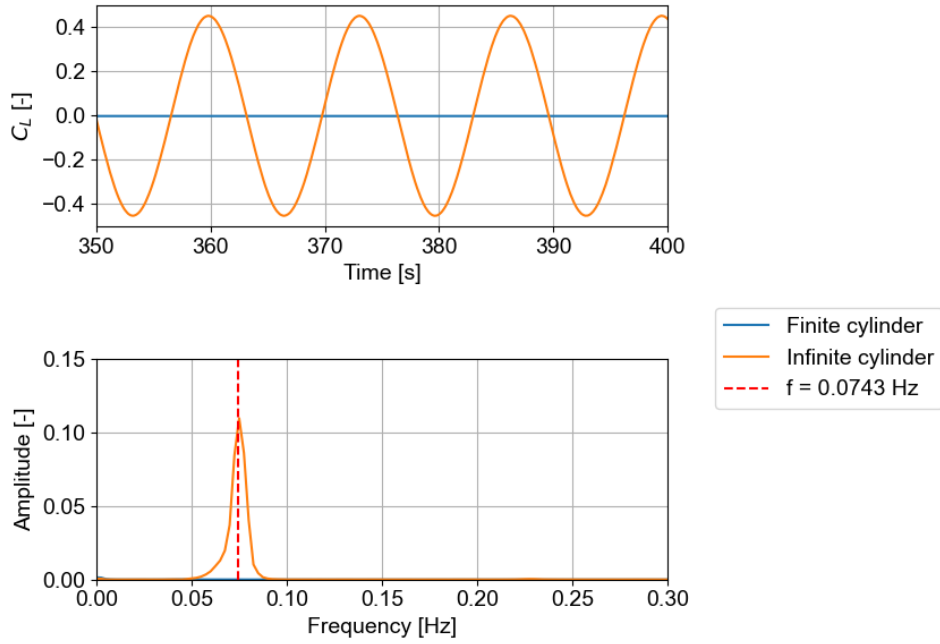
Figure 5.38: Time series and frequency spectrum of lift coefficient indicate that vortex shedding is observed in the infinite case but not tin he finite case.

$$St = \frac{fL}{U} = \frac{0.0743 * 0.24}{0.085} = 0.21 \tag{5.4}$$

To show the reason for the absence of vortex shedding in the finite length case, the z-component of the velocity field is shown in Figure 5.39. Positive z-direction flow velocity is seen at the downstream of the cylinder, flowing from the bottom of the cylinder to the free surface. This vertical flow breaks the vortex shedding downstream of the cylinder.
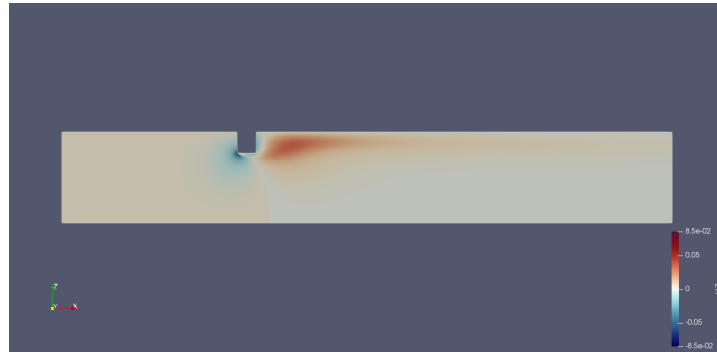
Figure 5.39: z component of the velocity field showing the vertical convective flow in the finite case suppressing vortex shedding.

It can be seen from Figure 5.40 that the flow over an infinite cylinder is mostly in the horizontal plane, while the flow over a finite cylinder has a vertical circulation behind it that breaks the vortices behind.

(a) Finite cylinder

(b) Infinite cylinder
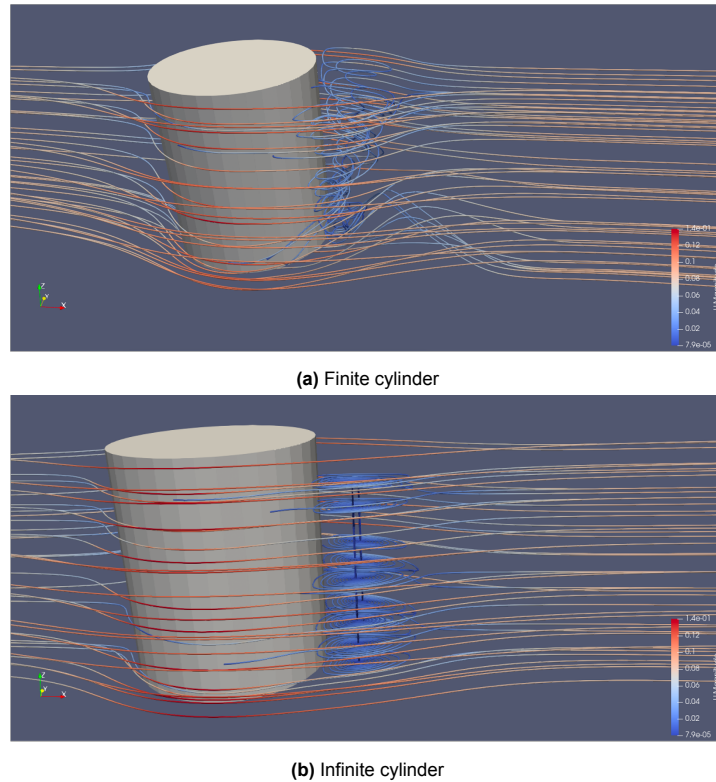
Figure 5.40: Streamlines in the infinite case are parallel and planar, resulting in high coherence and vortex shedding. While in the finite case, vertical convection flow disrupts and suppresses vortex shedding.

From this section, one can tell that the end effect plays a major role in vortex shedding. If the draft is shallow, the free end introduces 3D effects and can suppress the vortex shedding downstream. This is because vortex shedding requires a certain level of vertical coherence to sustain organized shedding along the span. The introduction of strong three-dimensionality near the free end disrupts this coherence, thereby weakening or entirely suppressing periodic vortex formation. This demonstrates the reason that vortex shedding phenomena is not found in the earlier cases.

5.5. Effect of draft: 10 m draft versus 20 m draft

Research from Ramachandran [31] shows that the OC4 floater has sufficient stability at 10 m draft, and this draft can be used for wet-towing. It is obvious that decreasing the draft can reduce the required force for towing the platform. To quantify the drag force that is reduced by decreasing the draft and to inspect if there are other effects introduced, a comparison is made in this section. Two simulations are conducted for the comparison, one with a draft of 10 m and the other with a draft of 20 m. Both simulations are conducted at full scale and in multiphase. The simulations are done at 0° heading as shown in Figure 5.41.
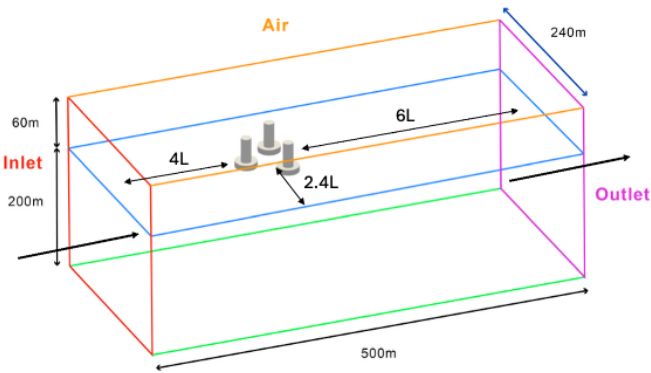
Figure 5.41: Illustration of the configuration for studying the effect of draft

The mesh is made following the procedure in section 3.3. The side views of both meshes are shown in Figure 5.42.

(a) Side view of floater at 10 m draft

(b) Side view of floater at 20 m draft
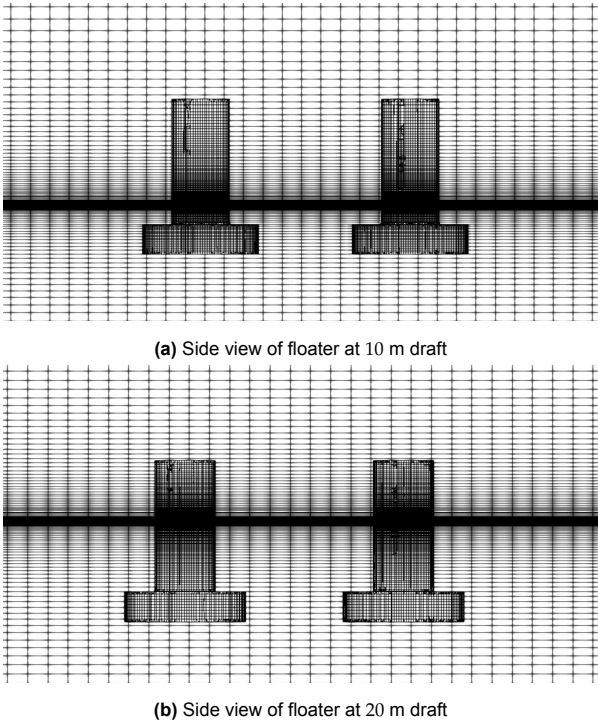
Figure 5.42: Side view of the meshes at 10 m and 20 m draft

The chosen towing speed is 2 knots, and the corresponding Froude number and Reynolds number are shown in Table 5.7 below.

Full scale speed [m/s]	Fr	Full scale Re
1.028	0.0947	1.23E+07

Table 5.7: Test cases for draft comparison

Figure 5.43 shows the mean drag forces on each column at 10 m draft and 20 m draft. The mean drag force of the whole floater is found to decrease by 40% lowering the draft to from 20 m to 10 m. For better comparison, the drag coefficients of each column and the full floater are shown in Table 5.8. The drag coefficients of 10 m draft model and 20 m draft model are very much the same.
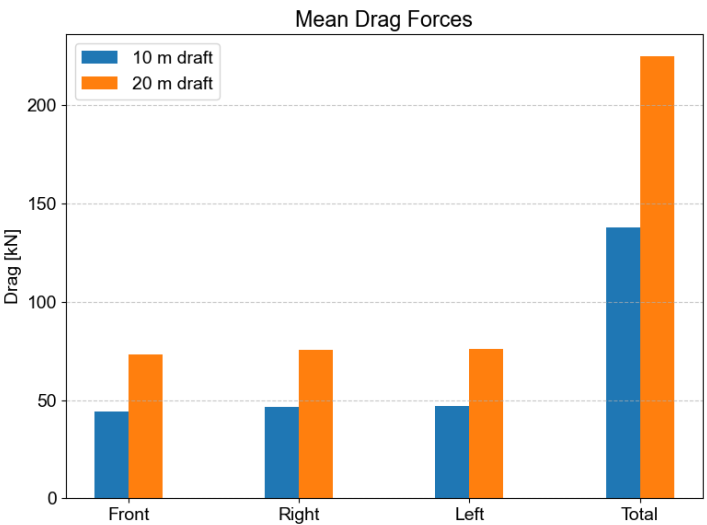
Figure 5.43: Comparison of drag force at 10 m and 20 m draft

	Mean drag [kN]		Drag coefficient	
	10 m draft	20 m draft	10 m draft	20 m draft
Front	44.4	73.6	0.43	0.44
Left	46.7	76.3	0.45	0.45
Right	47.0	76.2	0.45	0.45
Total	138.1	226.1	0.44	0.45

Table 5.8: Mean drag force and drag coefficient comparison of 10 m draft and 20 m draft
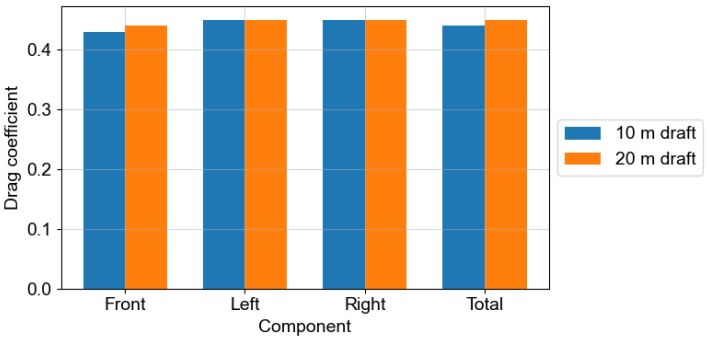
Figure 5.44: Drag coefficients of 10 m draft and 20 m draft are nearly identical.

Figure 5.45 shows the lift forces on each column at 10 m and 20 m draft. The difference in lift force behavior between the 10 m and 20 m draft configurations can be explained by analyzing the vorticity field and the 3D streamline structures. As shown in Figure 5.46, the vorticity cross-sections are taken

at a plane located 2 m above the base column. In the 10 m draft case, the vortex shedding is relatively simple and symmetric, with vortices propagating directly downstream. In contrast, the 20 m draft case exhibits a more complex pattern, with one or two vortices extending irregularly on the inside.

This observation is further supported by the streamline visualization in Figure 5.47, where the flow behind the right column at 20 m draft shows a more complicated circulation pattern compared to the relatively symmetric vortex pair observed in the 10 m case. The additional vertical extent of the submerged volume in the 20 m draft configuration contributes to the development of more complicated three-dimensional vortex structures. This may explain why the lift forces for the 20 m draft exhibit a steady offset, while the 10 m case is more symmetrically around zero. Furthermore, the aspect ratio of the 10 m draft and 20 m draft are 0.83 and 1.66, respectively. The streamlines show that both cases are highly affected by the free end, and these aspect ratios are not large enough for the vortices to have coherence.

(a) Lift force on each column at 10 m draft

(b) Lift force on each column at 20 m draft
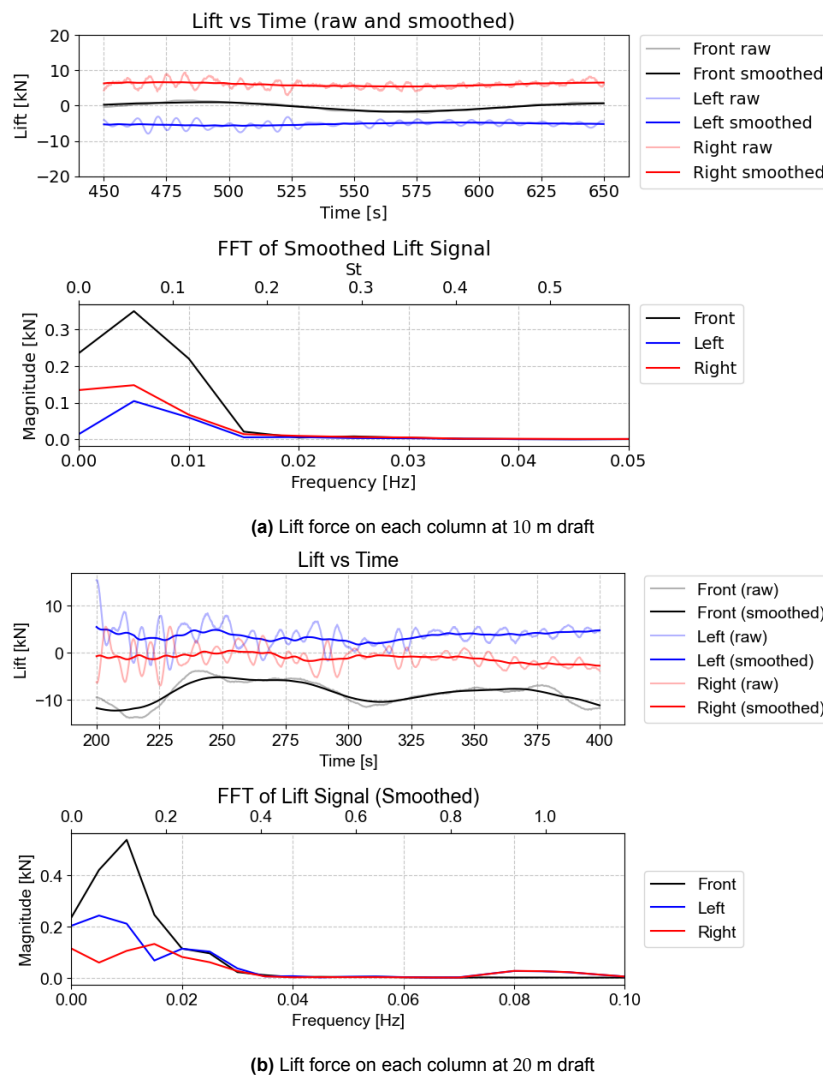
Figure 5.45: Lift forces of 10 m draft is steady, with the front column experiencing slight imbalance due to wake asymmetry. While in 20 m draft, the fluctuation is because of the more complex convective flow.
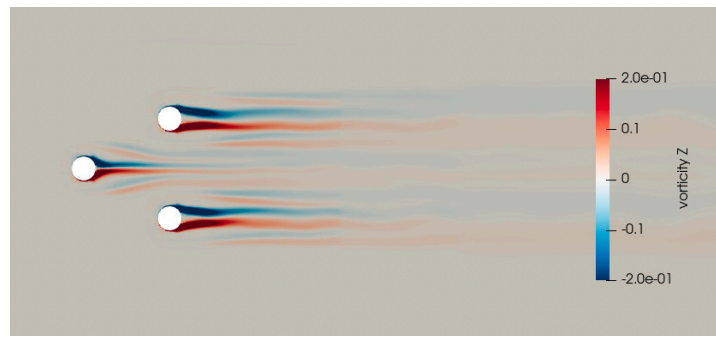
(a) Vorticity field of 10 m draft model at $z = -2$ m at $t = 600$ s
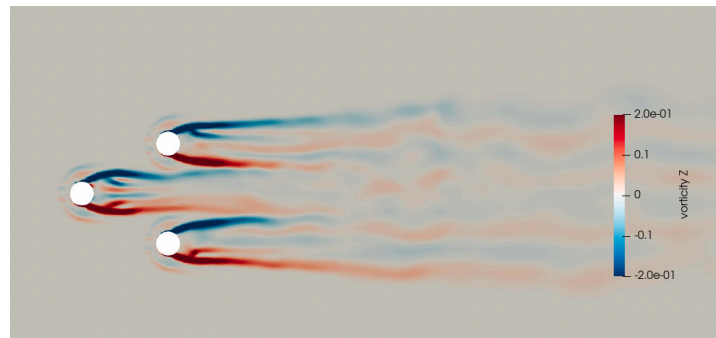
(b) Vorticity field of 20 m draft model at $z = -12$ m at $t = 400$ s

Figure 5.46: Vorticity field of 10 m draft is steady. While in 20 m draft, it is more irregular due to the vertical flow.

(a) View of the streamline behind the right column at 10 m draft

(b) View of the streamline behind the right column at 20 m draft
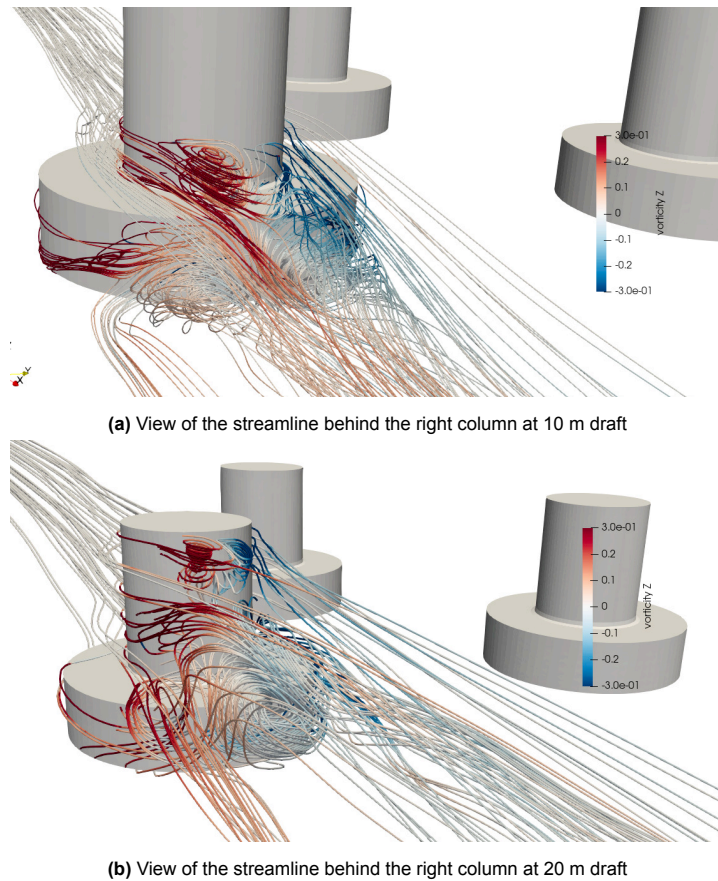
Figure 5.47: The streamlines in 20 m draft show more vertical convection due to the greater vertical extent. However, they indicate that both cases are highly affected by the free end and do not have a large enough aspect ratio for vortex shedding to develop.

Overall, the 20 m draft provides a greater vertical extent for the flow to develop, which enhances three-dimensional effects and results in a more complex wake structure. However, since both draft configurations exhibit strong 3D characteristics and lack of vertical coherence, classical vortex shedding is not observed. The essential point to convey from this comparison is that neither 10 m and 20 m draft have a large enough aspect ratio to overcome the effect of free end and form vortex shedding.

6

Conclusions

This study investigates the hydrodynamic behavior of a semi-submersible platform during wet-towing operations, with a focus on vortex shedding and drag prediction. The CFD tool *OpenFOAM* is used to simulate different towing conditions. The conclusions are made to answer the following research questions:

1. What is the more preferable towing heading between $0°$ and $180°$ and draft depth in terms of drag and wake dynamics?

2. What is the influence of the free surface on studying VIM of semi-submersible platforms?

3. What are the accuracy and efficiency of drag prediction and vortex behavior from full-scale multiphase model, full-scale single-phase model, and model-scale multiphase model?

Several models are simulated with CFD software *OpenFOAM* to compare the accuracy of estimated drag forces. These objectives aim to improve the physical understanding and prediction accuracy of hydrodynamic loads during wet-towing and to prevent unexpected phenomena during the operation. The DeepCWind OC4 floater is chosen for this study due to the amount of public data for validation and comparison. Its general geometry is expected to allow extending the findings in this study to semi-submersible platforms with similar geometry.

Validation

Three simulations with a towing speed of 0.3 m/s, 0.6 m/s, and 1.0 m/s with $0°$ heading at full-scale and multiphase are carried out. These simulations are done at a draft of 20 m, which is its designed installation draft. The resulting drag and lift forces are validated with the literature [5]. And the conclusions are shown below:

- The drag forces are in 10 % difference compared to the literature, except for the lowest speed, which is 30% higher.

- The dominant period around 8 s in the transverse force is also observed in this study. However,

this period in this study is found later to be **due to standing waves in the domain** caused by the initial transient, contradicting vortex shedding as mentioned in the literature.

- The frequency due to the wake asymmetry is found to be much lower, and it stabilizes with a longer simulation time.

What is the more preferable towing heading between 0° and 180° and draft depth in terms of drag and wake dynamics?

Simulations with 0° and 180° heading at full-scale and multiphase are done at a decreased draft of 10 m. Towing speeds of 1, 2, and 3 knots are simulated. Furthermore, a 20 m draft model in 0° heading is also carried out to study the effect of draft depth. The conclusions are as follows:

- The highly three-dimensional streamlines circulating from underneath the base columns reduce the coherence of the vortices and suppress vortex shedding. Therefore, no typical von Karman vortex street is observed in both 10 m and 20 m draft model.

- In 0°, the front column experiences slightly higher drag, and side columns experience non-zero mean lift due to flow acceleration between them.

- Simulations show slightly lower drag and near-zero mean lift in the 180° heading, **suggesting it is more preferable than the 0° heading**.

- **Draft of** 10 **m** can be used to reduce drag force. Additionally, the free end effect and the free surface effect are more pronounced in the shallower draft and vortex shedding is more unlikely to occur.

What is the influence of the free surface on studying VIM of semi-submersible platforms?

A single-phase simulation with a double-body assumption is carried out with a few motivations listed below.

1. To eliminate the reflection waves seen in the multiphase simulations.

2. The accuracy of drag prediction is of interest due to the lower computational cost.

3. Since vortex shedding is not seen in multiphase simulation, and Jiang [18] and Liu [25] studied VIM with single-phase simulations, the difference is of interest.

Both simulations have a towing speed of 2 knots, a 0° towing configuration, and a draft of 20 m. The conclusions are as follows:

- Multiphase simulations include free surface effects and are expected to better represent the reality, but no vortex shedding is observed.

- Single-phase (double-body assumption) simulations suppress vertical flow at the water surface and induce **vortex shedding with a period of** 50 **s** (Strouhal number 0.23).

- However, this shedding is likely an artifact of the symmetry boundary condition rather than a physically accurate behavior.

- The drag force is overestimated by 75 % in the single-phase case due to earlier separation and lack of free surface deformation.

What are the accuracy and efficiency of drag prediction and vortex behavior from full-scale multiphase model, full-scale single-phase model, and model-scale multiphase model?
The conclusions are broken down into two parts. One focusing on vortex shedding and the other focusing on drag prediction.

Vortex shedding

- Full-scale multiphase model is expected to be the most representative of real-life, and no vortex shedding is observed

- Full-scale single-phase model introduces constraints on the free surface, which is not physically correct, but it provides a potential vortex shedding period.

- Model-scale multiphase model has a very different flow field because of the Reynolds number mismatch, which is in the order of 10^4 in model scale and 10^7 in full scale. Therefore, it may not be suitable for studying vortex shedding.

Drag prediction

- The drag coefficient obtained from the relation to Reynolds number is 0.7. However, this relation does not account for the finite length and free end that allows the flow to escape from beneath.

- Full-scale multiphase model gives a drag coefficient of 0.45, and is validated with literature. The difference is less than 10 %, which is quite reliable.

- Full-scale single-phase model overpredicts by 75 % compared to the multiphase. It has a poor performance for drag prediction.

- Model-scale multiphase model provides a drag coefficient 40 % higher than the full-scale multiphase model. But it is more accurate than the drag coefficient predicted from the explicit relation, and the computational cost is one-fifth of the full-scale multiphase model.

- Model-scale multiphase model can be used for drag prediction for a balance of accuracy and efficiency. The drag force scaled with Froude's method can be used as an upper bound. It can be more accurate scaling with Hughes' method.

Practical implications

- For more complex geometry, where there are more fluid interactions and hand calculation find difficult, model-scale multiphase simulation can be used for drag prediction. Scaling with Froude's method can provide an upper bound for the towing load, and Hughes' method can be used to be more accurate.

- From the study, vortex shedding is not seen in both 10 m and 20 m drafts in the multiphase model. Therefore, it is unlikely to be a problem of wet-towing. Only the single-phase model shows a potential shedding period.

- Even if vortex shedding occurs, resonance in sway motion is unlikely to happen, due to the low restoring force of the towing system in the transverse direction.

- As a conclusion, the towing heading of $180°$ heading is more preferable, and a draft of 10 m can be used to reduce the required towing force.

- For reliable anticipated drag, the wind effect can be neglected, but the wave effect should be

included because it is significant.

Recommendations and future work

- One of the biggest challenges in this study is the reflection waves influencing the results. Several attempts are made, but they only alleviate the issue to a certain extent. Further research regarding non-reflective boundary conditions is required.

- To be certain that vortex shedding does not occur, an even higher fidelity tool, such as LES, might be required to resolve the smaller eddies. This is because the fluctuations could possibly be damped out due to the numerical damping introduced by URANS modeling and the solver.

- A dynamic meshing approach can be implemented to update the floater position and couple the dynamic motions with the hydrodynamics, as the feedback from the motion to the flow is quite important in vortex-induced motions. However, these combinations require a very high computational cost.

7

Limitations and recommendations

This chapter outlines the main limitations of the study and offers recommendations for future work. Key topics include coupling motion with hydrodynamics, challenges related to wave reflections and boundary conditions, and the influence of second-order wave drift and wind loads. These considerations provide a foundation for improving the accuracy and applicability of wet-towing simulations.

7.1. Dynamic meshing approach

The initial plan for this study was not only to compute the forces and frequencies, but also to obtain the vortex-induced motion (VIM) of the floater. A final phase of this study that is not conducted is fully coupling the dynamic motions and the hydrodynamics within *OpenFOAM*. Even though this is not done, the methodology is stated below, and further study can be done for more accurate and more informative research. Especially since vortex shedding is not observed in the multiphase fixed model in this study, it would be interesting if coupling the motion would make anything different.

An example illustration of the towing system is shown in Figure 7.1. The towing heading is 180° in this case. One end of the main towing line is connected to the tug boat, and the other end is connected to the floater with a bridle.
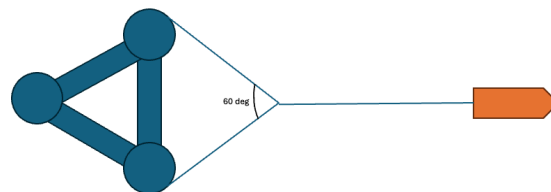
Figure 7.1: Illustration of the towing system

Since the VIM due to vortex shedding is of interest, the model can be simplified to a two degree of freedom in sway and yaw motion. An equivalent stiffness of the towing system in yaw and sway needs to be found and input into *OpenFOAM* to solve the equation of motion.

To obtain the stiffness of the towing system, the dynamic analysis software, *Orcaflex*, can be used. An equivalent spring stiffness can be obtained by inputting the drag coefficient obtained from CFD into *Orcaflex*, and setting up the towing configuration and the towing line properties. A free decay test can be done with the current speed set to the towing speed. The stiffness of the towing system depends on the towing speed as it is a component of the towing line tension as shown in Figure 7.2.
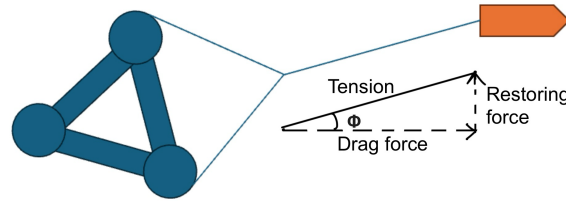
Figure 7.2: Force composition

By inputting this stiffness and the mass of the floater into the dynamic solver `dynamicMotionSolverFcMesh` in *OpenFOAM*, the motion due to the resulting hydrodynamic forces can be solved. Additionally, by adapting the dynamic meshing method, the position of the floater can be updated with a certain time step. This will provide a more accurate approach, as it fully couples the hydrodynamics and the motion. A hypothesis is that this may more easily trigger vortices to be coherent in the vertical direction and cause vortex shedding. However, the computational cost for dynamic meshing will be even higher than that of the present study.

Despite the method not being executed in this study, the framework laid out provides a path for future VIM analysis in semi-submersible wet-towing operations.

7.2. Standing waves and reflections

A major hurdle in this research is the reflection waves due to the transient at the beginning of the simulation. The inlet, outlet, and internal field are set to the target velocity as the initial condition. At the start of the simulation, the velocity difference at the surface of the floater is large, and this creates shock waves. The waves are then trapped inside the domain contaminating the results.

This issue can be fixed in two ways. One is to eliminate this transient at the start, and the other is to absorb the reflection waves. Many methods have been tried in this study, however, the problem is not solved in this study. The attempts and the effects are categorized below in these two ways so that further study can use them as a reference.

1. To prevent the transient from happening, a ramp-up is applied at the inlet patch with the `codedFixedValue` boundary condition, together with a `zeroGradient` outlet, and the internal field is initiated with zero velocity. However, this approach was not successful due to the length of the domain. The domain is 500 m long, and it was not possible to establish a uniform flow of 1

m/s throughout the entire domain within a reasonable simulation time. Subsequently, the outlet is also changed to a ramp-up function identical to the inlet. The result is that seiching, as shown in Figure 7.3, occurred, as well as the standing waves.
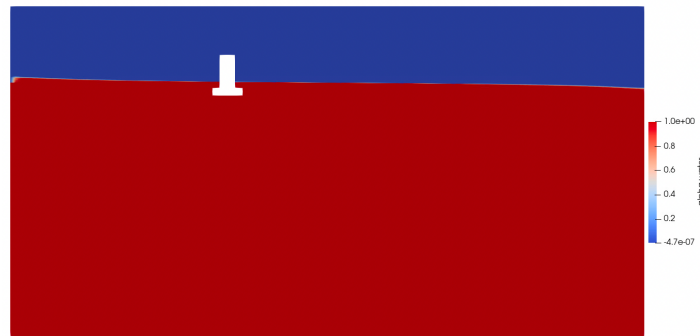

Figure 7.3: Seiching in the domain

There are also some other options, but they have not been tried due to technical limitations and time limitations. Instead of only ramping up the inlet and outlet patches, a time-dependent gravity in the flow direction can be applied. The acceleration can be set to a small value and turned off after the target velocity is reached. However, the gravity field in *OpenFOAM* is only read at the beginning of the simulation, and time-dependent gravity is not applicable unless changes are made to the source code. Therefore, it has not been tried.

2. Attempts to damp out the reflection waves are also made. Four damping zones are added to the sides with `explicitPorositySource` in `fvOptions`. The difference is observed as the elevation decreases faster, but the effect is limited, and it only works to a certain extent. This is mentioned in Figure 3.2.1. The `meanVelocityForce` is also attempted, but no noticeable improvement is observed. `meanVelocityForce` applies a force to the flow to maintain a specified velocity on the designated boundary.

   Another attempt is using outlet boundary condition instead of the symmetry plane for the sides as well. There are two types of non-reflective boundary conditions in *OpenFOAM*, one is the `waveTransmissive` and the other is `advective`. The `waveTransmissive` boundary condition requires a compressibility field since it is more dedicated to acoustics. Therefore, it is not applicable here. The `advective` boundary condition is used for `alpha` and `U`, and `fixedFluxPressure` for the pressure boundary condition. The attempt to use `advective` boundary condition is documented in more detail in section A.2, although it did not succeed.

   One other option is to increase the size of the domain. This is a simple way to alleviate the issue. However, as seen in the drag force, this does not solve the issue entirely but introduces higher modes. Additionally, this increases the number of cells, which is not desired in this study, as the computational cost is already quite high.

It is found that typical boundary conditions for multiphase simulations for calculating ship hull resistance may not be that well suitable for this study. This is because the much bluffer body diffracts more waves compared to the typical streamline shape of a ship hull. Recommendations are that non-reflective boundary conditions and wave-absorbing boundary conditions should be further investigated.

7.3. Effect of mean wave drift load (second-order) and wind

Even though this study only considers towing in calm water, the effect of mean wave drift load and wind load are still interested. The tug boat needs to pull the mean load of towing load in calm water, mean wave drift load, and mean wind load. Therefore, how the mean wave drift load and mean wind load compare to the towing load in calm water is of interest.

For the second-order wave load, the Maruo's Formula [9] as shown in Equation 7.1 is used, where ζ_a is the wave amplitude. This equation assumes that all waves are reflected and no transmitted waves so it is conservative. This provides the wave drift load of a 2D case.

$$\bar{F}_2 = 0.5\rho_{water}g\zeta_a{}^2 \tag{7.1}$$

The towing load in calm water in 2D as shown in Equation 7.2, where D is the draught and U is the towing speed.

$$F_{tow} = 0.5\rho_{water}C_{D,water}DU^2 \tag{7.2}$$

The ratio between these two forces is calculated as Equation 7.3. Assume that the towing speed (U) is 2 knots, the drag coefficient ($C_{D,water}$) is 0.45, obtained from the CFD simulations earlier, the draught (D) is 20 m and the wave height ($2\zeta_a$) is 2 m. The ratio is found to be 1.03. This shows that conservatively the wave drift load magnitude can be roughly the same as the towing load of 2 knots. Furthermore, this also shows that the ratio increases as the draught (D) decreases.

$$\frac{\bar{F}_2}{F_{tow}} = \frac{g\zeta_a^2}{C_{D,water}DU^2} \tag{7.3}$$

For the wind load, the wind load can be calculated with formulas similar to the towing load, and the ratio is shown in Equation 7.5.

$$F_{wind} = 0.5\rho_{air}C_{D,air}A_{air}U_{wind}{}^2 \tag{7.4}$$

$$\frac{F_{wind}}{F_{tow}} = \frac{\rho_{air}}{\rho_{water}}\frac{C_{D,air}}{C_{D,water}}\frac{A_{air}}{A_{water}}\frac{U_{wind}{}^2}{U^2} \tag{7.5}$$

Assume that the draught is still 20 m, the drag coefficient for the part in the air ($C_{D,air}$) is 1, the wind speed (U_{wind}) is 10 m/s, and the towing speed (U) is also 2 knots, the ratio of wind load to the towing load in calm water is 0.12.

Figure 7.4 compares the mean load of 2 m wave, 10 m/s wind, and the towing load in calm water with towing speeds from 1 to 3 knots.
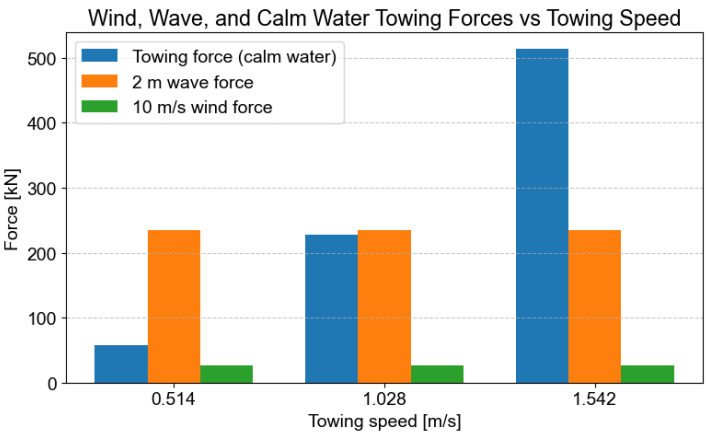
Figure 7.4: Mean force comparison of 2 m wave force, 10 m/s wind force, and towing load in calm water with towing speed of 1, 2, and 3 knots

This section shows that the contribution of wind is small and can be neglected. However, the wave drift load of 2 m wave is quite high and should be considered when predicting the required towing force.

References

[1] Delft High Performance Computing Centre (DHPC). *DelftBlue Supercomputer (Phase 2)*. `https://www.tudelft.nl/dhpc/ark:/44463/DelftBluePhase2`. 2024.

[2] Adnan Bajic. *Boskalis: Kincardine is a prelude to more floating wind projects*. en-US. Feb. 2021. URL: `https://www.projectcargojournal.com/offshore/2021/02/18/boskalis-kincardine-is-a-prelude-to-more-floating-wind-projects/` (visited on 04/15/2025).

[3] M A Benitz et al. "Comparison of Hydrodynamic Load Predictions Between Engineering Models and Computational Fluid Dynamics for the OC4-DeepCwind Semi-Submersible: Preprint". en. In: (2014).

[4] Maija Benitz. "Simulating the Hydrodynamics of Offshore Floating Wind Turbine Platforms in a Finite Volume Framework". en. In: (2016).

[5] Maija A. Benitz et al. "Validation of Hydrodynamic Load Models Using CFD for the OC4-DeepCwind Semisubmersible". en. In: *Volume 9: Ocean Renewable Energy*. St. John's, Newfoundland, Canada: American Society of Mechanical Engineers, May 2015, V009T09A037. ISBN: 978-0-7918-5657-4. DOI: `10.1115/OMAE2015-41045`. URL: `https://asmedigitalcollection.asme.org/OMAE/proceedings/OMAE2015/56574/St.%20John%E2%80%99s,%20Newfoundland,%20Canada/280004` (visited on 03/12/2025).

[6] Songtao Chen, Weiwen Zhao, and Decheng Wan. "CFD Study of Free Surface Effect on Flow around a Surface-Piercing Cylinder". en. In: (2020).

[7] Emma C. Edwards et al. "Trends in floating offshore wind platforms: A review of early-stage devices". en. In: *Renewable and Sustainable Energy Reviews* 193 (Apr. 2024), p. 114271. ISSN: 13640321. DOI: `10.1016/j.rser.2023.114271`. URL: `https://linkinghub.elsevier.com/retrieve/pii/S1364032123011292` (visited on 04/15/2025).

[8] F. Moukalled. *The Finite Volume Method in Computational Fluid Dynamics*. Vol. 113. Springer, 2015. ISBN: 978-3-319-16873-9.

[9] Odd M. Faltinsen. *Sea loads on ships and offshore structures*. en. 1. paperback ed., repr., transferred to digital printing. Cambridge ocean technology series. Cambridge: Cambridge University Press, 1999. ISBN: 978-0-521-45870-2.

[10] Joel H. Ferziger and Milovan Perić. *Computational Methods for Fluid Dynamics*. en. Berlin, Heidelberg: Springer Berlin Heidelberg, 2002. ISBN: 978-3-540-42074-3. DOI: `10.1007/978-3-642-56026-2`. URL: `http://link.springer.com/10.1007/978-3-642-56026-2` (visited on 03/12/2025).

[11] *FLOATING OFFSHORE WIND - A GLOBAL OPPORTUNITY*. Tech. rep. GWEC, 2022.

[12] *FLOATING OFFSHORE WIND:THE NEXT FIVE YEARS*. Tech. rep. DNV, 2022.

[13] Ch Hirsch. *Numerical computation of internal and external flows: fundamentals of computational fluid dynamics*. en. 2nd ed. Oxford Burlington, MA: Elsevier/Butterworth-Heinemann, 2007. ISBN: 978-0-7506-6594-0.

[14] Sunghun Hong et al. "Floating offshore wind farm installation, challenges and opportunities: A comprehensive survey". en. In: *Ocean Engineering* 304 (July 2024), p. 117793. ISSN: 00298018. DOI: 10.1016/j.oceaneng.2024.117793. URL: https://linkinghub.elsevier.com/retrieve/pii/S0029801824011314 (visited on 04/15/2025).

[15] I-Jen Hsu et al. "Optimization of Semi-Submersible Hull Design for Floating Offshore Wind Turbines". en. In: *Volume 8: Ocean Renewable Energy*. Hamburg, Germany: American Society of Mechanical Engineers, June 2022, V008T09A065. ISBN: 978-0-7918-8593-2. DOI: 10.1115/OMAE2022-86751. URL: https://asmedigitalcollection.asme.org/OMAE/proceedings/OMAE2022/85932/V008T09A065/1148004 (visited on 04/15/2025).

[16] Ian R. Young. *Wind Generated Ocean Waves*. Elsevier, 1999.

[17] "Introduction". en. In: *Mooring System Engineering for Offshore Structures*. Elsevier, 2019, pp. 1–18. ISBN: 978-0-12-818551-3. DOI: 10.1016/b978-0-12-818551-3.00001-6. URL: https://linkinghub.elsevier.com/retrieve/pii/B9780128185513000016 (visited on 07/15/2025).

[18] Fengjian Jiang et al. "Application of CFD on VIM of semi-submersible FOWT: A Case Study". en. In: *Journal of Physics: Conference Series* 2626.1 (Oct. 2023), p. 012041. ISSN: 1742-6588, 1742-6596. DOI: 10.1088/1742-6596/2626/1/012041. URL: https://iopscience.iop.org/article/10.1088/1742-6596/2626/1/012041 (visited on 05/09/2025).

[19] John H. Lienhard. *Synopsis of lift drag and vortex frequency data for rigid circular cylinders*. 1966.

[20] Jorgen Fredsoe. *Hydrodynamics Around Cylindrical Structures*. 2006.

[21] Hayato Kato, Kotaro Takamure, and Tomomi Uchiyama. "Characteristics of vortex shedding in the wake of a sphere with a uniaxial through-hole". en. In: *AIP Advances* 12.10 (Oct. 2022), p. 105112. ISSN: 2158-3226. DOI: 10.1063/5.0098762. URL: https://pubs.aip.org/adv/article/12/10/105112/2819838/Characteristics-of-vortex-shedding-in-the-wake-of (visited on 05/13/2025).

[22] *Kincardine Wind Farm*. en. Dec. 2021. URL: https://doriccolumns.wordpress.com/industry/electricity/aberdeen-offshore-wind-farm/kincardine-wind-farm/ (visited on 04/15/2025).

[23] Roger King. "A review of vortex shedding research and its application". en. In: *Ocean Engineering* 4.3 (July 1977), pp. 141–171. ISSN: 00298018. DOI: 10.1016/0029-8018(77)90002-6. URL: https://linkinghub.elsevier.com/retrieve/pii/0029801877900026 (visited on 06/18/2025).

[24] A. N. Kolmogorov. "The Local Structure of Turbulence in Incompressible Viscous Fluid for Very Large Reynolds Numbers". en. In: *Proceedings: Mathematical and Physical Sciences* 434.1890, (1991), pp. 9–13. URL: http://www.jstor.org/stable/51980.

[25] Yuanchuan Liu et al. "A CFD Study of Vortex-Induced Motions of a Semi-Submersible Floating Offshore Wind Turbine". en. In: *Energies* 16.2 (Jan. 2023), p. 698. ISSN: 1996-1073. DOI: 10.3390/en16020698. URL: https://www.mdpi.com/1996-1073/16/2/698 (visited on 03/22/2025).

[26] F. R. Menter. "Two-equation eddy-viscosity turbulence models for engineering applications". en. In: *AIAA Journal* 32.8 (Aug. 1994), pp. 1598–1605. ISSN: 0001-1452, 1533-385X. DOI: 10.2514/3.12149. URL: https://arc.aiaa.org/doi/10.2514/3.12149 (visited on 06/20/2025).

[27] Anthony F. Molland, Stephen R. Turnock, and Dominic A. Hudson, eds. *Ship Resistance and Propulsion: Practical Estimation of Propulsive Power*. en. Online-Ausg. Cambridge: Cambridge University Press, 2011. ISBN: 978-0-521-76052-2. DOI: 10.1017/CBO9780511974113.

[28] Shiki Okamoto and Yukisada Sunabashiri. "Vortex Shedding From a Circular Cylinder of Finite Length Placed on a Ground Plane". en. In: *Journal of Fluids Engineering* 114.4 (Dec. 1992), pp. 512–521. ISSN: 0098-2202, 1528-901X. DOI: `10.1115/1.2910062`. URL: `https://asme digitalcollection.asme.org/fluidsengineering/article/114/4/512/411001/Vortex-Shedding-From-a-Circular-Cylinder-of-Finite` (visited on 04/17/2025).

[29] OpenFOAM Foundation. *OpenFOAM User Guide*. 2024. URL: `https://www.openfoam.com/documentation/user-guide`.

[30] Ronald L Panton. "Incompressible Flow". en. In: (2013).

[31] Rahul Chitteth Ramachandran et al. "Towing Analysis and Validation of a Fully Assembled Floating Offshore Wind Turbine Based on an Experimental Study". en. In: *Journal of Marine Science and Engineering* 12.4 (Apr. 2024), p. 689. ISSN: 2077-1312. DOI: `10.3390/jmse12040689`. URL: `https://www.mdpi.com/2077-1312/12/4/689` (visited on 03/12/2025).

[32] *Resistance Uncertainty Analysis, Example for Resistance Test*. 2002.

[33] A. Robertson et al. *Definition of the Semisubmersible Floating System for Phase II of OC4*. en. Tech. rep. NREL/TP-5000-60601, 1155123. Sept. 2014, NREL/TP–5000–60601, 1155123. DOI: `10.2172/1155123`. URL: `http://www.osti.gov/servlets/purl/1155123/` (visited on 03/12/2025).

[34] Hermann Schlichting and Klaus Gersten. *Boundary-Layer Theory*. en. Berlin, Heidelberg: Springer Berlin Heidelberg, 2017. ISBN: 978-3-662-52917-1. DOI: `10.1007/978-3-662-52919-5`. URL: `http://link.springer.com/10.1007/978-3-662-52919-5` (visited on 04/02/2025).

[35] Tamotsu Igarashi. "Characteristics of the flow around two cylinders arranged in tandem". In: *JSME* (1981).

[36] Dongxu Wang and Sheng Dong. "A discussion of numerical wave absorption using sponge layer methods". en. In: *Ocean Engineering* 247 (Mar. 2022), p. 110732. ISSN: 00298018. DOI: `10.1016/j.oceaneng.2022.110732`. URL: `https://linkinghub.elsevier.com/retrieve/pii/S0029801822001834` (visited on 04/16/2025).

[37] David C. Wilcox. *Turbulence modeling for CFD*. en. 3. ed., 2. print. La Cañada, Calif.: DCW Industries, 2010. ISBN: 978-1-928729-08-2.

[38] M A Zahari and S S Dol. "Application of Vortex Induced Vibration Energy Generation Technologies to the Offshore Oil and Gas Platform: The Preliminary Study". en. In: 8.7 (2014).

[39] M M Zdravkovich. "THE EFFECTS OF INTERFERENCE BETWEEN CIRCULAR CYLINDERS IN CROSS FLOW". en. In: (1986).

A
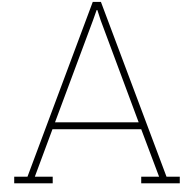
Appendix

A.1. Acknowledgement on the usage of AI

During the preparation of this thesis, artificial intelligence (AI) tools, such as OpenAI's ChatGPT, github Copilot, were employed to assist in several supporting tasks. This includes the following:

- Improving the clarity, coherence, and readability of written text.

- Supporting spelling and grammar correction.

- Providing suggestions to enhance logical flow and structure.

- Assisting in the preparation of technical plots and figures during post-processing.

- Offering preliminary feedback on phrasing, tone, and organization.

All outputs generated by AI tools were subject to critical evaluation and manual verification. The use of these tools was confined to editorial and auxiliary assistance, and did not extend to generating original research content, formulating core scientific arguments, or interpreting results. Full responsibility for the accuracy, originality, and academic integrity of the thesis rests solely with the author.
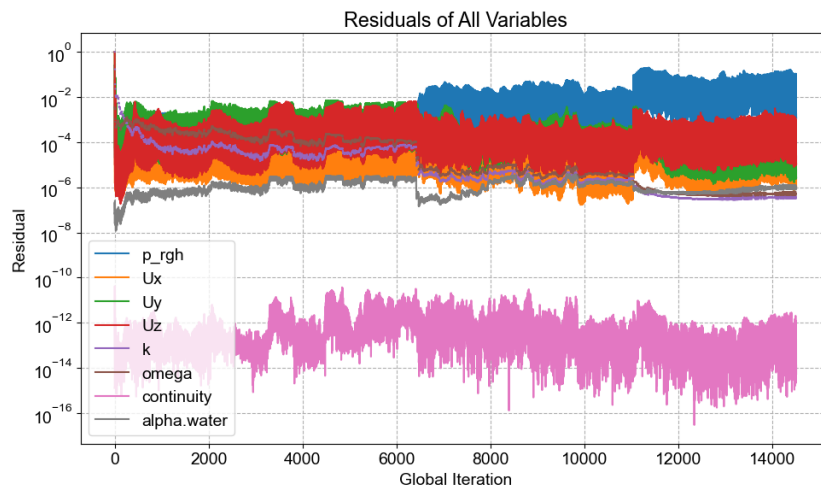
A.2. Non-reflective boundary condition

In the attempt with non-reflective boundary conditions, the boundary conditions are changed to Table A.1. The main differences are that `advective` boundary condition is used for **alpha.water** and **U** on the outlet and the sides, and the `fixedFluxPressure` boundary condition is used so that the pressure can change correspondingly.

| Patch	alpha.water	U	p_rgh
Inlet	fixedValue	fixedValue	fixedFluxPressure
Outlet	advective	advective	fixedFluxPressure
Left / Right	advective	advective	fixedFluxPressure
Top	inletOutlet	pressureInletOutletVelocity	totalPressure
Bottom	symmetryPlane	symmetryPlane	symmetryPlane
Wall (floater)	zeroGradient	fixedValue	fixedFluxPressure

Table A.1: Boundary conditions for `alpha.water`, `U`, and `p_rgh` with non-reflective boundary conditions

The mesh that is used is exactly the same as the one used in the earlier study. However, Figure A.1 shows that the simulation becomes very unstable due to the usage of the non-reflective boundary conditions. Additionally, the time step became unreasonably small starting from roughly 35 s.


Figure A.1: Residuals show that the simulation is very unstable with the non-reflective boundary conditions

From the water surface contour in Figure A.2 and the lift force time series in Figure A.3, the reflections are found to still be present, and the high-frequency oscillations as well.
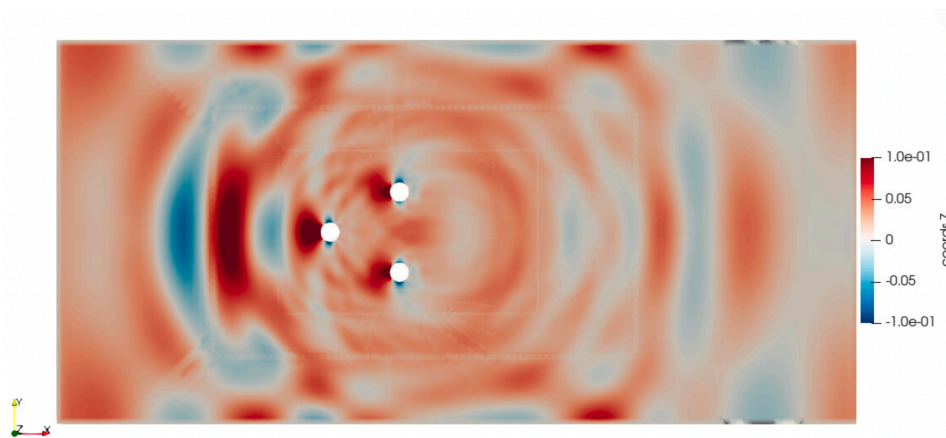
Figure A.2: z-coordinate of the free surface shows that reflections are still present at $t = 38$ s.
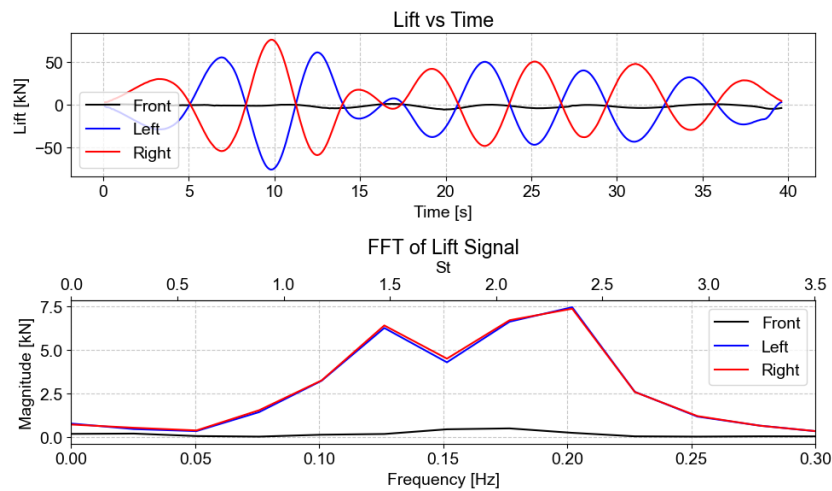
Figure A.3: Lift force time series shows that the high-frequency still exists.

While the simulation failed to complete, it is included to document the setup and difficulties encountered, which may inform future investigations and highlight potential challenges.

A.3. Attempt on 10 m draft model with double-body arrangement

An attempt to run the 10 m draft floater in a double-body arrangement is also made. However, an issue encountered is the conflict between the assumption of a double-body arrangement and the shallow draft. The double-body assumption uses a symmetry plane boundary condition at the top, which is the water surface, and the symmetry plane boundary condition assumes no normal flow across the boundary. The flow in front of the upper column has nowhere to escape due to the shallow draft, and therefore creates a very strong vortex as shown in Figure A.4. This also breaks the symmetry plane assumption at the top boundary as shown in Figure A.5 and crashes the simulation.
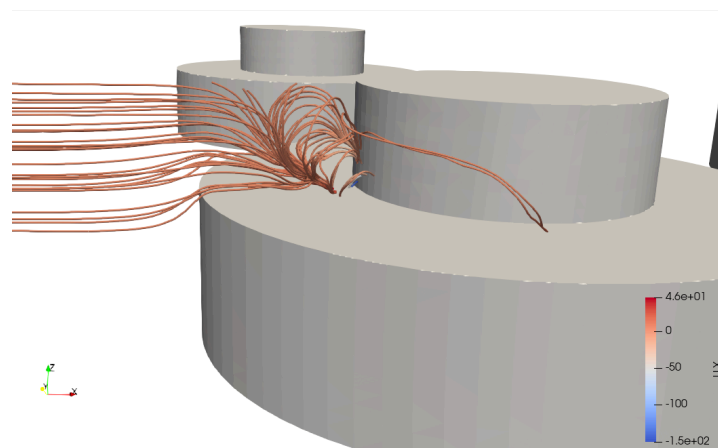
Figure A.4: Streamline of the attempt on 10 m draft model
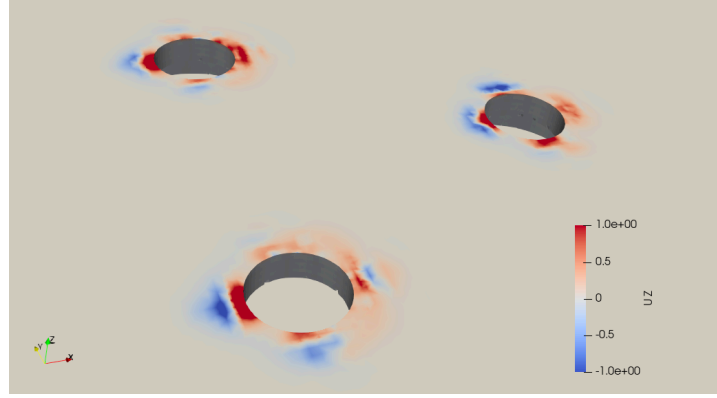
**Figure A.5:** Normal velocity on symmetry plane top boundary

A.4. Effect of first-order waves on towing resistance

The oscillatory wave loads caused by first-order wave excitation are primarily absorbed by the catenary configuration of the towing line. The range of this force can be estimated by basic calculation.

Using the linear wave theory [16], the horizontal water particle velocity (u) can be calculated with Equation A.1, where H is the wave height, k is the wave number, ω is the wave angular velocity, d is the water depth, and z is the vertical coordinate, where $z = 0$ is the free surface.

$$u = \frac{Hgk}{2\omega} \frac{\cosh |k(d+z)|}{\cosh (kd)} \sin (kx - \omega t) \tag{A.1}$$

Assuming a condition of wave height $H = 2$ m, wave period $T = 8$ s, water depth $d = 200$ m, together with the dispersion relation and Equation A.1, the amplitude of horizontal water particle velocity (u) is found to be 0.79 m/s at $z = 0$. Figure A.6 shows the horizontal water particle velocity profile over a depth of 0 to 20 m.
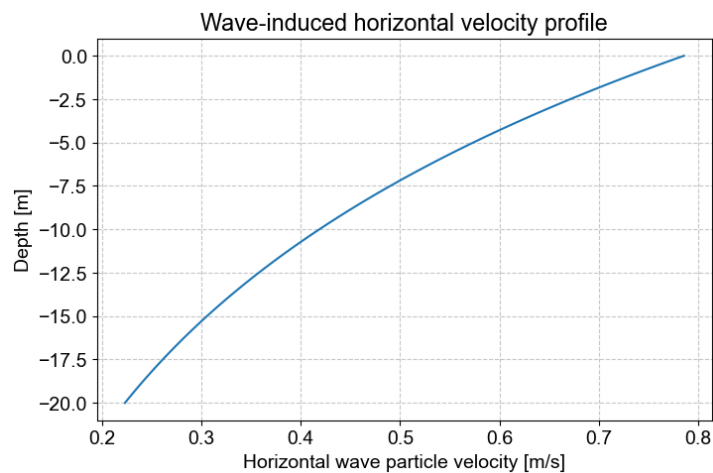

Figure A.6: The horizontal water particle velocity of 2 m wave over depth

The depths over the columns are discretized and account for the wave-induced particle velocity at different depths. Figure A.7 shows the drag force and the range due to the 2 m wave when towing at different speeds in the direction of wave propagation. The draft is chosen to be 20 m, and a drag coefficient of 0.45 is used. Note that this drag force only accounts for the side columns.
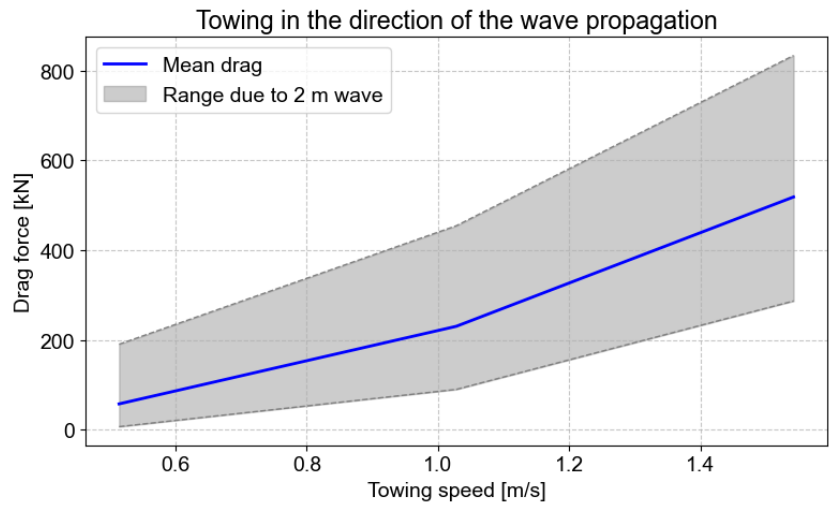
Figure A.7: Drag force and the effect of 2 m wave when towing in the direction of the wave propagation

The maximum and minimum of the range shown in Figure A.7 compared to the mean drag are then presented as percentages in Figure A.8. At a towing speed of 1 knot, the maximum can be more than two times the mean. As the towing speed increases, the relative change gets smaller, but it is still quite significant.
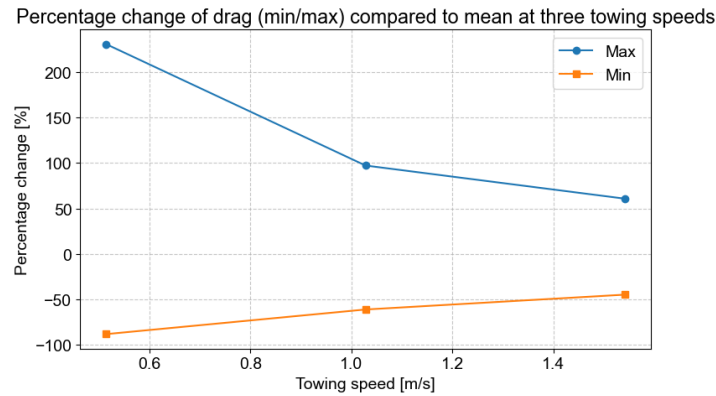
Figure A.8: Maximum and minimum drag compared to the mean drag at different towing speeds in percentage

The estimation in this section gives an idea of the range of the tension that the catenary shape towing line experiences.